

MECHANICAL CHARACTERIZATION, MODELING, AND EXAMINATION OF A
MUSCULAR INTRACRANIAL AND ELASTIC EXTRACRANIAL ARTERY WITH
AN EMPHASIS ON MICROSTRUCTURE, RESIDUAL STRESS,
AND SMOOTH MUSCLE CELL ACTIVATION

A Dissertation

by

HALLIE PAIGE WAGNER

Submitted to the Office of Graduate Studies of
Texas A&M University
in partial fulfillment of the requirements for the degree of

DOCTOR OF PHILOSOPHY

May 2011

Major Subject: Biomedical Engineering

Mechanical Characterization, Modeling, and Examination of a Muscular Intracranial and
Elastic Extracranial Artery with an Emphasis on Microstructure, Residual Stress, and
Smooth Muscle Cell Activation

Copyright 2011 Hallie Paige Wagner

MECHANICAL CHARACTERIZATION, MODELING, AND EXAMINATION OF A
MUSCULAR INTRACRANIAL AND ELASTIC EXTRACRANIAL ARTERY WITH
AN EMPHASIS ON MICROSTRUCTURE, RESIDUAL STRESS,
AND SMOOTH MUSCLE CELL ACTIVATION

A Dissertation

by

HALLIE PAIGE WAGNER

Submitted to the Office of Graduate Studies of
Texas A&M University
in partial fulfillment of the requirements for the degree of

DOCTOR OF PHILOSOPHY

Approved by:

Chair of Committee,	James E. Moore, Jr.
Committee Members,	Alvin T. Yeh
	Emily Wilson
	Duncan J. Maitland
Head of Department,	Gerard L. Cote

May 2011

Major Subject: Biomedical Engineering

ABSTRACT

Mechanical Characterization, Modeling, and Examination of a Muscular Intracranial and Elastic Extracranial Artery with an Emphasis on Microstructure, Residual Stress, and Smooth Muscle Cell Activation. (May 2011)

Hallie Paige Wagner, B.S., Washington University in St. Louis

Chair of Advisory Committee: Dr. James E. Moore, Jr.

Cerebrovascular disease continues to be responsible for significant morbidity and mortality. There is a pressing need to better understand the biomechanics of both intracranial arteries and the extracranial arteries that feed these vessels. Histology and immunohistochemistry were performed on basilar and carotid arteries and elucidated their structural differences. Nonlinear optical microscopy (NLOM) provided collagen fiber orientation and distribution, which offered motivation for a more microstructurally-based model. Biaxial testing was performed on acute basilar and carotid arteries and cultured basilar arteries. We used a validated 2D, four fiber family constitutive relation to model passive biaxial stress-stretch behaviors of basilar and common carotid arteries, and we developed a new relation to model their active biaxial responses. Residual stress information from opening angles and collagen fiber orientation were used to create a 3D fiber distribution constitutive relation. Passive biaxial stress-stretch behavior of basilar arteries was modeled with the 3D fiber distribution constitutive relation and was combined with our new active relation to model the active response of basilar arteries.

These data and 2D, four fiber family and active constitutive relation allow the first full comparison of circumferential and axial biomechanical behaviors between a muscular (basilar) and an elastic (carotid) artery from the same species. Our active model describes the responses by both types of vessels to four doses of the vasoconstrictor endothelin-1 (10^{-10} , 10^{-9} , 10^{-8} , 10^{-7} M) and predicts levels of smooth muscle activation associated with basal tone under specific in vitro testing conditions. Cultured arteries revealed smooth muscle tone is necessary for vascular remodeling. Our 3D model allowed for the calculation of stress through the wall in passive basilar arteries. These results advance our understanding of the biomechanics of intracranial and extracranial arteries, which is needed to understand better their differential responses to similar perturbations in hemodynamic loading.

ACKNOWLEDGEMENTS

I would like to thank my advisor, Dr. Humphrey, my committee chair, Dr. Moore, and my committee members, Dr. Yeh, Dr. Wilson, and Dr. Maitland. This research was supported, in part, by grants from the NIH (HL-64372, HL-80415).

Thanks also go to my friends, faculty, and fellow students. From Dr. Humphrey's lab I would like to thank Dr. Samantha Steelman for her expertise and companionship during experiments, Dr. John Eberth for his help during early stages of this work, Mrs. Melissa Collins, Dr. Heather Hayenga and undergraduates Matt Bersi and Brooke Hallmark. From Dr. Yeh's lab I would like to thank Dr. Qiaofeng Wu and Mr. Yuqiang Bai for their work capturing NLOM images. From Dr. Moore's lab I would like to thank Ellie Rahbar for being an amazing friend and a great sounding board. A thank you also goes to Prof. A.D. McCulloch (UCSD) for providing the code Continuity for our fiber angle assessments (see www.continuity.ucsd.edu, software developed via NIH grant NCRR P41 RR08605).

Finally, thanks to my family for encouragement and my husband Kyle Wagner, LSSP for his love, patience, and amazing editing skills.

TABLE OF CONTENTS

	Page
ABSTRACT	iii
ACKNOWLEDGEMENTS	v
TABLE OF CONTENTS	vi
LIST OF FIGURES	viii
LIST OF TABLES	xi
CHAPTER	
I INTRODUCTION.....	1
II NORMAL BASILAR ARTERY STRUCTURE AND BIAxIAL MECHANICAL BEHAVIOR.....	13
Introduction	13
Methods	14
Results	24
Discussion	35
III DIFFERENTIAL PASSIVE AND ACTIVE BIAxIAL MECHANICAL BEHAVIORS OF MUSCULAR AND ELASTIC ARTERIES: BASILAR AND COMMON CAROTID.....	47
Introduction	47
Methods	48
Results	57
Discussion	69
IV PROLONGED EX VIVO CULTURE OF THE RABBIT BASILAR ARTERY AND ITS EFFECTS ON BIAxIAL MECHANICAL BEHAVIOR	76
Introduction	76
Methods	77
Results	84

CHAPTER		Page
	Discussion	94
V	A 3D MICROSTRUCTURAL ARTERY MODEL WITH COLLAGEN FIBER ORIENTATION AND SMOOTH MUSCLE CELL ACTIVATION	97
	Introduction	97
	Methods	98
	Results	107
	Discussion	116
VI	CONCLUSION	123
	Summary	123
	Recommendations	125
	REFERENCES	128
	VITA	139

LIST OF FIGURES

FIGURE	Page
1.1 Schematic of Stress-free, Unloaded and Loaded Configurations	9
2.1 Video Image of a Cannulated Rabbit Basilar Artery	15
2.2 Schematic and NLOM Image of Rabbit Basilar Artery	19
2.3 Characteristic Data from Active/Passive Experiments	25
2.4 Representative Experimental Data and 4FF Model Fits at Axial Stretches of 1.15 and 1.2	27
2.5 NLOM SHG Optical Slices from a Representative Basilar Artery Imaged at 0, 40 and 80 mmHg	29
2.6 Three-Dimensional Histogram of Normalized and Averaged NLOM Data Sets	31
2.7 Distribution of Fiber Orientations within Characteristic Slices	32
2.8 Representative Experimental Data and 4FF Model Fit with a Fixed Mean Fiber Angle	34
2.9 Computations of Representative Energy Storage for the Two Primary Sets of Fiber Families as a Function of Fiber Stretch	41
3.1 Representative Histological Slices of Basilar and Carotid Arteries with H&E and VVG Staining	56
3.2 Representative Basilar Artery Data at Passive, Basal, and Four Levels of Active Tone	59
3.3 Representative Carotid Artery Data at Passive, Basal, and Four Levels of Active Tone	59
3.4 Representative Passive Basilar Artery Data and 4FF Model Fits	61
3.5 Representative Passive Carotid Artery Data and 4FF Model Fits	61

FIGURE	Page
3.6 NLOM Image Slices of an Illustrative Basilar and Carotid Artery.....	64
3.7 Representative Active Basilar Artery Data and Active Model Fits	66
3.8 Representative Active Carotid Artery Data and Active Model Fits.....	66
4.1 Representative Control Culture Data from Days 0, 1, 3, and 5.....	85
4.2 Representative Control Culture Day 5 ‘Passive’ Data and Fits	85
4.3 Representative Control Culture Days 0, 1, and 3 ‘Active/Basal Tone’ Data and Fits.....	87
4.4 Representative Growth Factor Culture Data from Days 0, 1, 3, and 5	90
4.5 Representative Growth Factor Culture Day 5 ‘Passive’ Data and Fits	90
4.6 Representative Growth Factor Culture Days 0, 1, and 3 ‘Active/Basal Tone’ Data and Fits	92
5.1 Schematic of Opening Angle Setup and Measurement Φ_0	99
5.2 Schematic of Collagen Fiber Angle Measurement α	101
5.3 Quantified Loaded Collagen Fiber Angles from NLOM Images and Von Mises Fits	109
5.4 Fits and Data of Modified von Mises Function Parameters c and k	110
5.5 Representative Passive Data and Distribution Fiber Model Fits.....	112
5.6 Radial, Axial, and Circumferential Stress Data from Representative Distribution Fiber Model Fits at a Loaded State of $P=80\text{mmHg}$	112
5.7 Representative Active Data and Active Model Fits	113
5.8 Bright and Dark Field Images of Sirius Red Stained Sections	114
5.9 Florescent Images of αSMA , Elastin, DAPI and a Composite Showing All Three	115

FIGURE	Page
5.10 Florescent Images of ET-B Receptors, Elastin and DAPI, and Composite Showing All Three	115
5.11 Quantified Loaded Carotid Collagen Fiber Angles from NLOM Images..	122

LIST OF TABLES

TABLE	Page
2.1 Weighting Factors used to Average Measured Collagen Fiber Angles	23
2.2 Best-fit Material Parameters from 4FF Model Fits	26
2.3 Best-fit Material Parameters from 4FF Model Fits with α_0 Fixed at 42.2°	33
3.1 Reference Inner and Outer Radii, in vivo Axial Stretch, Equivalent [ET-1] for Basal Tone Arteries and Calculated λ_M for Basilar and Carotid Arteries	58
3.2 Best-Fit Parameters for Passive Basilar Data 4FF Model Fits	62
3.3 Best-Fit Parameters for Passive Carotid Data 4FF Model Fits	63
3.4 Best-Fit Parameters for Active Basilar Data Active Model Fits	68
3.5 Best-Fit Parameters for Active Carotid Data Active Model Fits	68
4.1 Values of Constriction to 60 mM KCl on Days 0, 1, 3 and 5 and Calculated λ_M for Culture Controls	84
4.2 Best-Fit Parameters for Control Culture Day 5 Data ‘Passive’ Fits	86
4.3 Best-Fit Parameters for Control Culture Day 0, 1, and 3 Data ‘Active/Basal Tone’ Fits	88
4.4 Values of Constriction to 60 mM KCl on Days 0, 1, 3 and 5 and Calculated λ_M for Growth Factor Cultures	89
4.5 Best-Fit Parameters for Growth Factor Culture Day 5 Data ‘Passive’ Fits	91
4.6 Best-Fit Parameters for Growth Factor Culture Day 0, 1, and 3 Data ‘Active/Basal Tone’ Fits	93

TABLE	Page
5.1 Reference Inner and Outer Radii, Wall Thickness, in vivo Axial Stretch, Opening Angles, Collagen to Elastin Ratio and Area Fraction of Smooth Muscle	108
5.2 Mean Best-Fit Parameters for Fits of Modified von Mises Function Parameters c and k for Loaded and Unloaded Collagen Fiber Orientations	110
5.3 Mean Best-fit Parameter Values for Distribution Fiber Model Fits.....	111
5.4 Mean Best-fit Parameter Values for Active Model Fits.....	113
5.5 Reference Inner and Outer Radii, Wall Thickness, in vivo Axial Stretch, Opening Angles, Collagen to Elastin Ratio and Area Fraction of Smooth Muscle for the Carotid Artery	121

CHAPTER I

INTRODUCTION

Cerebrovascular disease is the third leading cause of death in the United States [1]. Two categories of cerebrovascular disease are ischemic events and cerebral hemorrhage, with further classification by etiology, location, and duration of symptoms. For example, subarachnoid hemorrhage is when bleeding occurs between the arachnoid membrane and the pia mater. While cerebrovascular disease is significant in its own right it is often a marker of underlying disease. Hypertension can cause intercranial hematomas, as well as being a major risk factor for stroke. Small intercranial artery stenosis is associated with hypertension and diabetes. Emboli from the heart are responsible for 10 to 20% of ischemic strokes. Atrial fibrillation and acute myocardial infarction are the most common cardiac conditions that predispose to embolization [2].

Hajdu et al. [3] showed remodeling of cerebral arteries in a hypertensive mouse model. Given the adaptive nature of cerebral vasculature, it is important for not only cerebrovascular disease, but vascular diseases in general that we obtain a better understanding of native cerebral arteries and how they differ from extracranial arteries.

Cerebral arteries are unique muscular arteries which supply the brain with a constant supply of blood. Like all arteries, cerebral arteries have an intima, media and

adventitia. The intima consists of a basement membrane and a single layer of endothelial cells which form part of the blood brain barrier (BBB). The media contains collagen predominately type I and III [4], elastin fragments [5], as well as smooth muscle cells (SMCs). The adventitial layer is primarily collagen type I, but also contains fibroblasts [4]. Walmsley et al. [6] reported the basilar artery wall by percent composition as $15 \pm 0.9\%$ intima, $49 \pm 5.6\%$ media, and $36 \pm 1.2\%$ adventitia. Cerebral arteries are set apart from systemic elastic arteries by the following: BBB, autoregulation, and elastic lamina [7].

The BBB is located at the intima and has three main functions: maintaining the ion balance, transporting nutrients, and preventing toxic substances from reaching the parenchyma. The BBB is composed of endothelial cells embedded in the basement membrane. This membrane, also known as a basal lamina, consists of type IV collagen, heparin sulfate proteoglycans, laminin, fibronectin, and other ECM proteins. Embedded endothelial cells form tight junctions which force transportation to occur via pinocytosis, or across the plasma membrane. The BBB is also a metabolic barrier capable of metabolizing drugs and nutrients. While the BBB plays a very important role, it does not contribute any load bearing constituents to cerebral arteries [8].

In autoregulation, a system uses an internal adaptive mechanism to regulate its own response to stimuli. Cerebral autoregulation refers to cerebral circulation maintaining blood flow despite changes in systemic blood pressure. Blood flow is maintained through vasoconstriction or vasodilation, which occur via changes in SMC tone. In the case of a high systemic pressure, cerebral arteries are circumferentially

stretched which in turn stretches the SMCs. This initiates a myogenic response causing the SMCs to constrict, increasing resistance and thereby decreasing the blood flow back to the optimal level. Low systemic pressures lead to an accumulation of metabolites, which leads to SMC relaxation. This vasodilation provides less resistance and increased cerebral blood flow. In humans the effective range of autoregulation is 50 to 160 mmHg. Such strong autoregulation is possible due to the abundance of SMCs which make up two thirds of cerebral arteries by volume [9]. However, autoregulation is often disrupted in cases of traumatic brain injury [10].

Elastic arteries are known for their numerous layers of elastin, which begin at the internal elastic lamina and continue until the external elastic lamina, a defining point between the media and adventitia. Muscular cerebral arteries differ in that they contain only internal elastic lamina and contain very few layers of elastin [11, 12]. Because cerebral arteries do not have an external elastic lamina, the end of the media is instead defined by a border of SMCs [9]. Cerebral vessels also have higher collagen to elastin ratios when compared to extracranial arteries, which is attributed to fewer layers of elastin, meaning lower levels of elastin in cerebral arteries [13-15].

Collagen elastin, and SMCs are the primary load bearing constituents in an artery, with SMCs accounting for variations in vascular tones [16]. Therefore, only medial and adventitial layers contribute structurally. Elastin is the major component of mature elastic fibers in arteries. These elastic fibers, and therefore elastin, are responsible in part for an artery being able to return to its original geometry after

deformation. Being highly cross-linked gives elastin its recoil properties [16]. Elastin is found in concentric lamina or layers with collagen and SMCs sandwiched in between.

Numerous types of collagen are expressed in arteries. Collagen types I and III, fibril forming collagens, are considered the main load bearing structural components of arteries [16]. The media of cerebral arteries contains collagen type I and III whereas the adventitia is predominately type I [4, 9]. Collagen type I is much stiffer than collagen type III, which implies the media is more compliant than the adventitia. Many groups have looked at collagen orientation through the arterial wall.

Canham et al. [12] concluded that collagen contributes significantly to the mechanical behavior of cerebral vessels, specifically those at and above physiologic pressures. In this study cerebral arteries were fixed at pressures ranging from 0 to 200 mmHg, then sectioned and stained. Using polarized light microscopy and the natural birefringence of collagen they obtained collagen fiber orientations. Adventitial collagen was found to have a circumferential component that increased with pressure. No conclusions could be made with respect to axially oriented fibers because they are tangential to the viewing plane. Rowe et al. [9] fixed a variety of cerebral arteries (middle cerebral, basilar, posterior cerebral, and posterior communicating arteries) and used the same technique as Canham et al. [12] to measure collagen fiber orientation at bifurcations. They found collagen in the adventitia “contribute[d] about one third of circumferential and almost all of longitudinal strength” [9]. Finlay et al. [7] used similar procedures to those mentioned above. However, they used a tangential sectioning procedure, which allowed for more complete collagen fiber orientation. In this study,

human cerebral arteries were pressure fixed at 30, 120, and 200 mmHg. Medial collagen was found to be circumferentially oriented and highly aligned. Adventitial collagen was found to have a wide distribution about an axial orientation. Canham [12], Rowe [9] and Finlay [7] all used fixed arteries. Fixation can alter the structure from what would be found in vivo and introduce errors in measuring orientations. However, even accounting for error, all three studies show collagen fiber orientation varies through the wall of cerebral arteries.

SMCs are a unique load bearing constituent due to their ability to contract as well as generate more load bearing constituents. Relaxed SMCs make very little structural contribution. However, when activated they contract becoming significant load bearing constituents. Much of their contribution is in the circumferential direction due to their predominately circumferential orientation [6, 7, 17].

SMCs can be made to relax or contract by two means: myogenic response and metabolic mechanism [10]. Myogenic response occurs when the vessel is inflated (circumferentially stretched), elongating the SMCs. In response the SMCs contract generating more force [18, 19]. Ohta et al. [20] showed myogenic tone developed in rat basilar arteries in vivo when the flow rate was above 10 ml/min.

Metabolic mechanism is the accumulation of vasoactive molecules, which then cause SMCs to relax or contract, respectively [10]. Constriction or relaxation to vasoactive molecules is dependent on concentration, location of exposure, transmural pressure and luminal flow. In a laboratory setting two commonly used vasoconstrictors are potassium chloride (KCl) and endothelin-1 (ET-1). Maximum SMC contraction can

be achieved through high concentrations of KCl [13, 21]. KCl is often used to determine the contractility of an artery, which is used as a measure of viability [21]. KCl is known to cause transient activation of cerebral arteries when exposed adventitially, but causes a phasic type contraction when applied intraluminally [20]. ET-1 leads to more prolonged constrictions, which do not decrease if ET-1 is rinsed from the vessel [22]. Vinall et al. (23) looked at how pressure affects the response of cerebral arteries to KCl and 5-HT. Potassium was found to cause greater constriction at lower pressures, but 5-HT constriction wasn't effected by changes in pressure. Similarly, Ohta et al. [20] made note that variations in flow rate alter basilar artery response to KCl.

SMCs can synthesis collagen, elastin, glycoprotiens, and proteoglycans [23] as well as proliferate. Synthesis is regulated by growth factors such as PDGF and TGF- β . PDGF induces cell proliferation and migration in SMCs [24]. TGF- β induces or inhibits cell proliferation depending on concentration as well as inducing collagen synthesis [25].

Mechanical testing of cerebral arteries has been done in a very limited capacity. Hayashi et al. [13, 14] mechanically tested human vessels at their in vivo length under active and passive conditions. These vessels came from human cadavers and included intracranial and extracranial vertebral, basilar, internal carotid, common carotid, and femoral arteries. Mechanical properties were then quantified by calculating circumferential stress as well as using incremental elastic modulus and stiffness parameter $\beta = \frac{\ln(P/P_s)}{R/R_s - 1}$, where P is pressure, R is radius, P_s is standard pressure which was 100 mmHg and R_s is the radius at standard pressure. Stiffness and elastic properties

were found to vary between intracranial and extracranial arteries as well as young and old arteries. Young intracranial arteries were found to have higher β values making them some of the stiffest vessels with the exception of middle-aged femoral arteries. Stiffness of intracranial arteries was found to increase with age. Young intracranial arteries experience higher circumferential stresses than older intracranial arteries. Increased wall thickness to radius ratio was determined to be the cause of decreased stress, increased stiffness and was found to compensate for decreased elasticity. Extracranial arteries, by comparison, start out with very low β values, which don't increase significantly until after 40 years of age. Comparing older arteries revealed intracranial arteries to be much stiffer than extracranial.

Monson et al. [26] mechanically tested human cerebral arteries and veins to failure at unperfused and unpressurized conditions. These tests are unique because they were designed to study axial mechanical properties, where as most arterial mechanical test focus on circumferential properties. Cerebral vessels underwent axial stretching in a static or dynamic manner until failure. Intracranial arteries were much stiffer than veins, undergoing twice as much stress at failure. Veins, however, were found to be much more axially compliant and were able to be stretched twice as far before failure. While these results aren't unexpected, in vivo geometry was not maintained, therefore the results may be unreliable in describing in vivo characteristics of a cerebral artery.

Monson et al. [27] biaxially tested human cerebral arteries at physiologic stretches and pressures, then axially stretched them to failure. In vivo and unloaded axial lengths were recorded to determine vessel specific in vivo axial stretch, prior to

which, vessels were preconditioned. Vessels underwent three inflation tests at three constant axial stretches, and three axial stretch tests at three constant pressures. Axial stress and stretch, as well as mean circumferential stress and stretch were calculated from their results. Small axial deformations resulted in much higher stresses than larger circumferential deformations; proving cerebral arteries are stiffer in the axial than circumferential direction. Data was fit with a four parameter Fung-type hyperelastic constitutive model, which supported observed anisotropy of the vessel. In order to better compare specimen to specimen, axial and circumferential stretch were calculated at in vivo conditions for each specimen. Axial and circumferential stretch was normalized by these values. This resulted in circumferential and axial stress stretch curves being tightly grouped despite differences in age and sex of the specimen. Opening angles were also recorded from sections adjacent to those biaxially tested. Opening angles varied considerable with a mean of 107 degrees, but a min of -17 and a max of 180 degrees. Large variations are common with opening angle measurements.

Experiments with animal models are very informative, though they can be even more instructive when paired with mathematical modeling, as seen in Monson et al. [27]. Modeling allows for the simulation of experiment, decreasing the number of animals needing to be sacrificed. Modeling also can help clarify which experiments have more potential or would be more helpful in understanding vascular biomechanics.

An accurate mathematical model must account for the differences in material properties of the structural components. As previously mentioned collagen, elastin, and smooth muscle are the primary load bearing constituents of arteries. Stresses are an

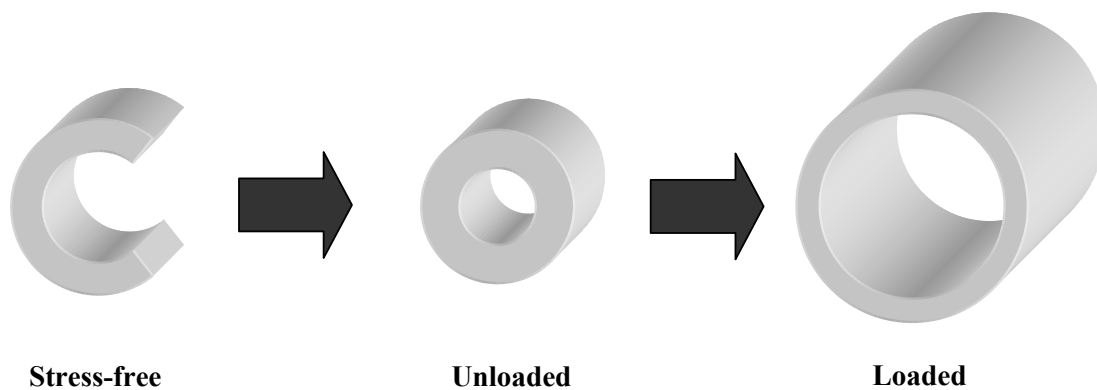


Fig. 1.1 Schematic of stress-free, unloaded and loaded configurations.

integral part of determining material properties. In a lab setting we prescribe a deformation and then measure the forces created by said deformation. Deformation is often referred to by three configurations: stress-free, unloaded, and loaded [28]. A stress-free configuration is when axial ends of the vessels are free, meaning there is no applied axial force, and a cut has been made through the vessel wall along the long axis to ensure no circumferential stress (Fig. 1.1). An unloaded configuration has no applied axial force, but the vessel wall is left intact. Last of all, in a loaded configuration the vessel is axially stretched and pressurized, leading to stresses in the axial, radial and circumferential directions. (Torsion or shear can also be applied in the loaded state, but is not considered in this dissertation.)

Residual, or prestresses, are the stresses in the wall of a vessel when that vessel is deformed from the stress-free to the unloaded state. Often residual stress isn't taken into account and stress is calculated as a vessel goes from the unloaded to the loaded state.

However, for the most accurate model, deformation from stress free to the loaded state should be considered. Forces and vessel geometry are measured during these deformations. Using these forces and the assumption that an artery has a cylindrical geometry we calculate the stresses in the arterial wall, which in conjunction with the prescribed deformation can be used to determine the mechanical properties of the artery.

Axial, radial, and circumferential, stresses can then be calculated from experimental measured values such as axial force, transmural pressure, and inner and outer radii in stress free, unloaded and loaded conditions. Deformation of a vessel is described using stretches. Axial, radial and circumferential stretches are calculated by stress free, unloaded and loaded radii and axial length. The relationship between these stretches and stresses were then modeled.

In order to model wall stress a theoretical framework is established. We assume our material (artery wall) is nonlinear, anisotropic, incompressible isothermal, and pseudoelastic [28]. A reference configuration maps to a current configuration through a deformation gradient \tilde{F} . In this framework Cauchy stress is

$$\sigma = -p\tilde{I} + 2\tilde{F}\frac{\partial W}{\partial \tilde{C}}\tilde{F}^T, \quad (1.1)$$

where \tilde{I} is the identity tensor, p is the Lagrange multiplier, W is the strain energy function and \tilde{C} is the left Cauchy-Green tensor ($\tilde{C} = \tilde{F}^T \tilde{F}$). A strain energy function takes into account all of the structurally significant components: elastin, collagen, and smooth muscle. Elastin and collagen are more simply modeled due to smooth muscle's ability to activate and contract. Modeling SMC activation must take into account

circumferential orientation [17], and increased contraction in response to circumferential stretch [18, 19], increased contraction to vasoconstrictors, and the effects of contraction in both circumferential [18] and axial directions [29].

Often it is best to start with a simplified model. Common simplifications include using a two-dimensional (2D) model projected onto three-dimensional (3D) surface and disregarding the stress free state. 2D models of this type have been shown to describe mechanical behavior quite well in both extracranial and cerebral arteries [30-33]. 2D models are computationally less expensive, which means getting results quicker. However, because 2D models are a simplification they are less informative. Stresses through the artery wall cannot be calculated. Also, 2D models often have material parameters which don't directly relate to measureable values, making the model more difficult to verify. Both of these issues can be addressed by using a 3D model based on vessel microstructure.

A microstructurally based 3D model is ideal for simulating the mechanical response of cerebral arteries. As mentioned earlier Finlay [34] and Canham [12] looked extensively at the collagen microstructure of cerebral arteries and found that it changed through the artery wall. Therefore a 3D model is essential in describing the collagen microstructure. A 3D model also allows for the calculation of stresses through the artery wall, which is essential for understanding cardiovascular disease. Cells have been shown to be 'picky' about their environment and will migrate, apoptosis, or secrete growth factors if not under ideal mechanical conditions [35]. These can trigger maladaptive growth and remodeling.

Complete characterization of normal cerebral vasculature is necessary in order to develop a better understanding of how cerebral arteries differ from extracranial arteries and how they are effected by cerebrovascular and other diseases. 2D modeling can provide accurate predictions of mechanical behavior, but lack vital information due to their simplification. A fully 3D model based on microstructurally information, which takes into account varying levels of smooth muscle cell activation as well as residual stresses would be ideal. Such a model could determine stresses through the wall, which often lead to maladaptive growth and remodeling in disease vessels. The ability to determine these stresses would lead to a better understanding of cerebrovascular diseases.

CHAPTER II

NORMAL BASILAR ARTERY STRUCTURE AND BIAXIAL MECHANICAL BEHAVIOR*

INTRODUCTION

The leading cause of death and disability in patients who survive subarachnoid hemorrhage (SAH) is stroke resulting from cerebral vasospasm, a delayed and prolonged narrowing of cerebral blood vessels that typically occurs three to five days post SAH [36]. Approximately 70% of patients presenting with SAH will experience some level of vasospasm [37]. Despite advances in treatment, nearly 50% of these patients will develop infarction and 15 to 20% will suffer a disabling stroke or die of progressive ischemia, a clinical situation that unfortunately has not changed much over the past three decades [38, 39].

A general consensus in the current literature on cerebral vasospasm implicates changes in the stiffness of the passive structural components of affected arteries as well as changes in the mechanical behavior of the smooth muscle. Although the etiology remains to be established, we submit that biochemomechanical mediated growth and remodeling processes play a key role in such structural changes [40]. To interpret cerebral vasospasm within such a theoretical framework, however, careful attention must

*Reprinted with permission from “Normal basilar artery structure and biaxial mechanical behaviour” by B.K. Wicker, H.P. Hutchens, Q. Wu, A.T. Yeh and J.D. Humphrey, 2008. *Computer Methods in Biomechanics and Biomedical Engineering*, **11**(5) pp. 539-551. Copyright 2008 by Taylor & Francis.

be given to the associated time course of changes in biomechanical properties, which requires a thorough understanding of the normal vessel. Yet, the biomechanics of the normal cerebral vasculature, and in particular that of common animal models, such as the rabbit basilar artery, has not been well characterized. In this paper we present new data on the passive and active biaxial mechanical behavior of normal rabbit basilar arteries, provide details on the associated transmural distribution of collagen, and employ a structurally-motivated constitutive relation to describe the passive behavior.

METHODS

The basilar artery was harvested from male New Zealand White Specific Pathogen Free Rabbits by removing the surrounding brain and spinal cord, then isolating the vessel from the brain stem under a dissection microscope. The artery was then divided into two equal segments (~5-6 mm length): the proximal portion for mechanical testing using a modified version of our computer-controlled biaxial testing and culture device [41] and the distal portion for imaging using a custom nonlinear optical microscopy (NLOM) system [42]. Both proximal and distal portions of the vessel were first prepared to enable “pressure stabilization” during testing. Specifically, following ligation of the larger branches with sterile 7-0 suture, the artery was secured using 6-0 ligatures onto custom glass cannulae (~300 μm tip) in either the mechanical testing device or a custom imaging chamber. To stabilize and control the intraluminal pressure, the remaining small branches were occluded via an injection of dextran microspheres (133 to 215 μm diameter; Cytodex 3, Sigma) into the lumen to prevent leakage (Fig. 2.1).

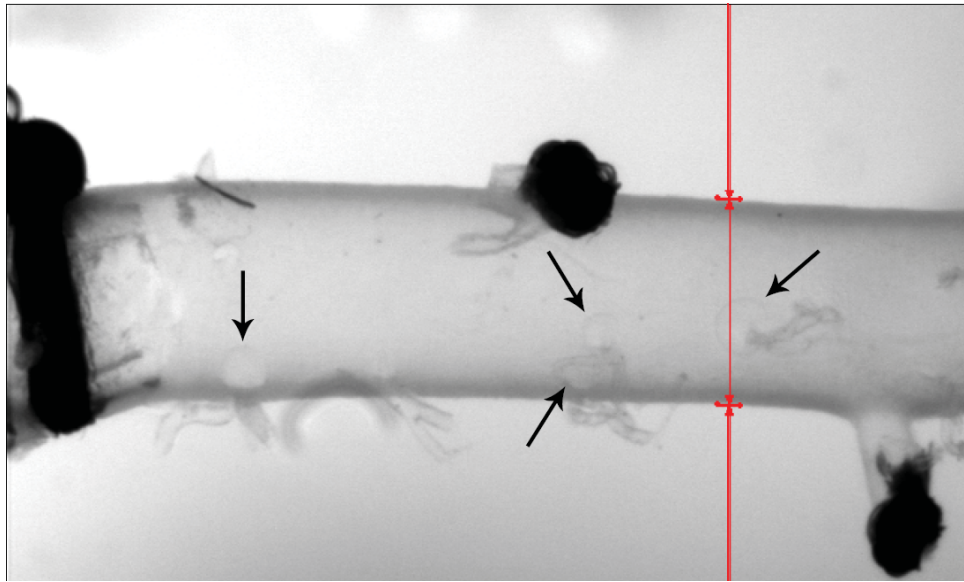


Fig. 2.1 Video image of a cannulated rabbit basilar artery. (Pressure = 7 mmHg, axial stretch = 1.15) Note the silk suture on the left holding the vessel on the glass cannula tip, ligation of larger branches with suture, the on-line computer-generated lines marking the outer diameter, and the microspheres (see black arrows) occluding unligated smaller branches.

Once pressure was stabilized and device setup completed, the unloaded length and diameter were measured and recorded at zero axial force and a transmural pressure of 7 mmHg (pilot studies revealed that the microspheres could dislodge at pressures less than 7 mmHg). The in vivo axial stretch was estimated to be 1.3 based on preliminary pressure-axial force data interpreted according to the method of van Loon et al. [43]. Conservative values of axial stretch from 1.1 to 1.2 were used for testing herein; the associated applied axial force was on the order of 5-7 mN, close to the value used by Ohta et al. [20]. A conservative estimate of in vivo transmural blood pressure in the rabbit basilar is 80 mmHg: the difference between a mean arterial pressure of ~85 mmHg and a cerebrospinal fluid pressure of ~5 mmHg. Following an acclimation period

of 1 hour at an axial stretch of 1.15 and a pressure of 7 mmHg, the artery was subjected to a gradual preconditioning process: cyclic pressurization from 7 to 60, 7 to 70, then 7 to 80 mmHg at an axial stretch of 1.1 followed by cycles from 7 to 70, 7 to 80, and again from 7 to 80 mmHg at a stretch of 1.2. This particular protocol was designed based on pilot studies to minimize hysteresis while protecting against possible mechanical damage to the smooth muscle or loss of the occluding microspheres. Indeed, the reported preconditioning cycles sufficiently eliminated any detectable hysteresis during cyclic mechanical testing (data not shown). Inner and outer radii were recorded in preconditioned vessels at fixed axial stretches of 1.1, 1.15, and 1.2 and associated fixed pressures of 7, 40, and 80 mmHg, thus yielding data at six statically loaded states to be used as described below to compute mean wall volume. Unloaded length and diameters were measured and recorded again following preconditioning, with only slight increases relative to the original measurements that followed the acclimation period. Mechanical testing then consisted of cyclic pressurization from 7 to 80 mmHg at fixed axial stretches of 1.1, 1.15, and 1.2 while recording pressure, diameter, and axial force. These stretches of 1.1, 1.15, and 1.2 were computed relative to the preconditioned unloaded lengths and were well below axial yield and failure values of 1.4 reported by Monson et al. [44, 45] for human cerebral arteries; data are not available on the failure axial stretches of rabbit basilar arteries. To ensure viability following periods of preconditioning and testing, vessels were then exposed to 60 mM KCl via the adventitial bath and associated decreases in diameter were measured over 15 minutes at a pressure of 7 mmHg and stretch of 1.15. A contraction of 30% was considered to reveal a fully viable artery [46].

KCl was chosen for viability testing since it elicits a reversible response and reveals both overall contractile capacity and endothelial-independent smooth muscle cell viability [21]; data were analyzed only for viable specimens. On a subset of arteries, another cyclic pressure protocol at a fixed in vivo stretch was performed during KCl exposure to record behavior under high levels of smooth muscle tone.

Each recorded inner, \hat{a} , and outer, \hat{b} , radius at length, ℓ , in the aforementioned six statically loaded states was used to calculate a wall volume, V , namely

$$V = \pi(\hat{b}^2 - \hat{a}^2)\ell. \quad (2.1)$$

These six volumes were averaged, yielding the value \bar{V} that combined with the assumption of incompressibility, was used to compute inner radius, a , at any cyclically pressurized testing condition given on-line measurements of outer diameter, $2b$. That is,

$$a = \sqrt{b^2 - \bar{V} / (\pi\ell)}. \quad (2.2)$$

These equations along with pressure-diameter and axial force data were used to calculate mean circumferential and axial Cauchy stresses and associated stretches,

$$\sigma_\theta = \frac{Pa}{h}, \quad \sigma_z = \frac{f}{\pi h(2a + h)}, \quad (2.3)$$

where P is the transmural pressure (outer pressure assumed to be approximately zero), $h = b - a$ is the wall thickness, and $f = f_T + \pi a^2 P$ is the total applied axial force, with f_T the force measured directly by the force transducer and the second term accounting for the luminal pressure acting over the projected area of the distended, cannulated vessel. The associated mean stretch ratios were computed as

$$\lambda_\theta = \frac{(a+b)/2}{(A+B)/2}, \quad \lambda_z = \frac{\ell}{L}, \quad (2.4)$$

where A and B denote unloaded inner radius and outer radius, respectively, and L denotes unloaded length. If one is interested in studying growth and remodeling *ex vivo*, the unloaded values should be measured both at the beginning of the study and as the vessel adapts over time. Herein, however, these values were constant.

For purposes of quantification of the passive biaxial data, a four-fiber family (4FF) Holzapfel-type strain-energy function was used [47]

$$W = \frac{c}{2}(I_1 - 3) + \sum_{k=1,2,3,4} \frac{c_1^k}{4c_2^k} \left\{ \exp \left[c_2^k \left((\lambda^k)^2 - 1 \right)^2 \right] - 1 \right\}, \quad (2.5)$$

where I_1 is the first invariant of the right Cauchy-Green tensor and c is an associated material parameter having dimensions of kPa; this term models the assumed isotropic contribution of the elastin-dominated amorphous extracellular matrix. Fiber family $k = 1$ and 2 denote axially (0°) and circumferential (90°) oriented collagen fiber, respectively, whereas families $k = 3$ and 4 denote diagonally oriented collagen fibers; the circumferentially oriented family can also include contributions due to passive smooth muscle cells (Fig. 2.2). With superscript k denoting the k^{th} fiber family, c_1^k (with dimension of kPa) and c_2^k (dimensionless) are thus the associated material parameters. For convenience, we let the material parameters for the diagonal fibers be equal, that is $c_1^3 = c_1^4$ and $c_2^3 = c_2^4$ (cf.[48]). Finally, note that λ^k is the stretch of the k^{th} fiber family, which is calculated as

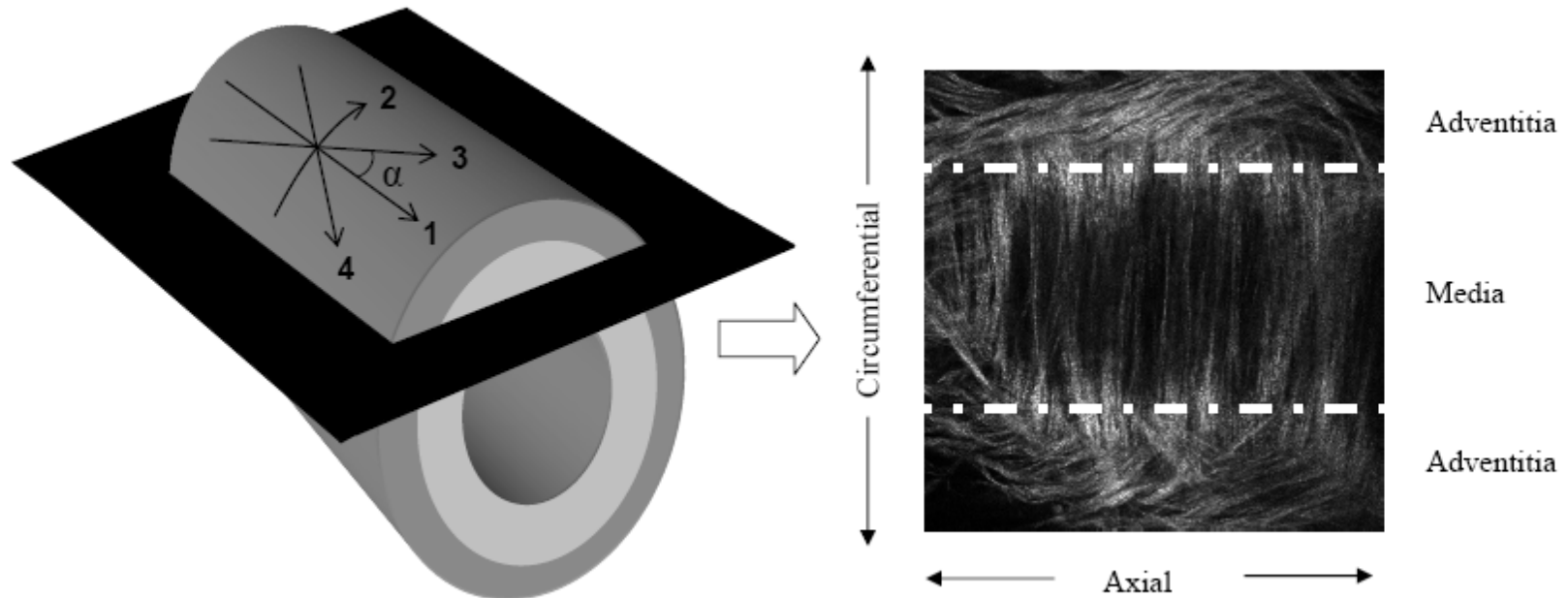


Fig. 2.2 Schematic and NLOM image of rabbit basilar artery. Optical slice was obtained from a pressurized artery via second harmonic generation (SHG) using NLOM. The adventitia is shown schematically in dark grey, the media in light grey and the optical slice in black. Note that the curvature of the vessel can capture collagen in the adventitia and media within a single optical slice, which motivates a cropping of the images prior to analysis to minimize effects of curvature (horizontal dashed lines in the image on the right). Finally, note that the observed collagen fiber orientations motivated the use of a four-fiber family constitutive model, the four families of which are denoted 1–4 in the schematic of the wall. Specifically, families 1 and 2 are axial (0°) and circumferential (90°), respectively, whereas families 3 and 4 are oriented diagonally.

$$\lambda^k = \sqrt{\lambda_z^2 \cos^2 \alpha_o^k + \lambda_\theta^2 \sin^2 \alpha_o^k} \quad (2.6)$$

where α_o^k represents the angle between a fiber family and the axial direction in the reference configuration. As they should, $\alpha_o^1 = 0^\circ$ and $\alpha_o^2 = 90^\circ$ recovers the axial and circumferential stretches for these families. Hence, below we focus on one angle, $(\alpha_0 \equiv \alpha_o^3 = -\alpha_o^4)$.

It is easy to show that the associated mean circumferential and axial Cauchy stresses are,

$$\sigma_\theta = \lambda_\theta \frac{\partial W}{\partial \lambda_\theta} = c \lambda_\theta^2 \left(1 - \frac{1}{\lambda_\theta^4 \lambda_z^2} \right) + \lambda_\theta^2 \sum_{k=1,2,3,4} \left\{ c_1^k ((\lambda^k)^2 - 1) \exp \left[c_2^k ((\lambda^k)^2 - 1)^2 \right] \sin^2 \alpha_o^k \right\}, \quad (2.7)$$

$$\sigma_z = \lambda_z \frac{\partial W}{\partial \lambda_z} = c \lambda_z^2 \left(1 - \frac{1}{\lambda_\theta^2 \lambda_z^4} \right) + \lambda_z^2 \sum_{k=1,2,3,4} \left\{ c_1^k ((\lambda^k)^2 - 1) \exp \left[c_2^k ((\lambda^k)^2 - 1)^2 \right] \cos^2 \alpha_o^k \right\}. \quad (2.8)$$

Note that $\sigma_i(\lambda_\theta = 1, \lambda_z = 1) = 0$ as they should at the reference configuration ($i = \theta, z$) and that the diagonal fibers can contribute to both the circumferential and the axial stress.

Values of the material and structural parameters were calculated via nonlinear regression (using the Matlab `fminsearchbnd` function) by minimizing the following objective function e , which accounts for differences between theoretically-predicted and experimentally-measured loads, namely

$$e = 0.5 * \sum_{i=1}^N \left[\left(\frac{P^{Theory} - P^{Exp}}{P^{Exp}} \right)_i^2 + \left(\frac{f^{Theory} - f^{Exp}}{f^{Exp}} \right)_i^2 \right], \quad (2.9)$$

where N is the number of data points. The superscript ‘Theory’ denotes the variable calculated using Eqs. 2.3 through 2.8 whereas the superscript ‘Exp’ denotes the experimental data. To restrict the parameter search space, all parameters had a lower allowed value of 0, but only α_o had an upper bound ($\pi/2$).

In parallel, the distal segment of the basilar artery was imaged using a custom NLOM system [42]. The artery was stretched axially to approximate the testing condition of 1.15 prior to imaging given expected effects of axial stretch on both undulation and orientation of the collagen fibers. Images were taken at three different pressures, 0, 40, and 80 mmHg, to determine effects of pressure on collagen undulation; the non-zero values were thus the same as those used in the statically loaded experiments to determine inner and outer radii and thus wall volume.

Sub-10-fs laser pulses (800 nm, FWHM 133 nm) from a Kerr-lens mode-locked Ti:Al₂O₃ oscillator (Femtosome compact, Femtolasers, Vienna, Austria) pumped by a frequency-doubled Nd:YVO₄ solid-state laser (Verdi, Coherent, Santa Clara, CA, U.S.A.) were coupled into the epifluorescence port of an upright microscope (Axioskop2 MAT, Carl Zeiss, Thornwood, NY, U.S.A.) via dual-axis galvanometer driven mirrors (Cambridge Technology, Lexington, MA, U.S.A.). Phase distortions introduced by the NLOM system were minimized by dispersion compensating mirrors and antireflection coated windows and wedge pair. Laser pulses were directed to the microscope objective (40X Achromplan, 0.8 NA; Carl Zeiss, Thornwood, NY, U.S.A.) using a short-pass dichroic mirror (635dcspxruv3p, Chroma, Rockingham, VT, U.S.A.). Second harmonic generation (SHG) in collagen was collected by the focusing objective and directed to a

photon counting photomultiplier tube (R7400P, Hamamatsu) using an appropriate long-pass dichroic mirror (505DCXRU, Chroma, Rockingham, VT, U.S.A.) and band-pass filter (HQ405/40M, Chroma, Rockingham, VT, U.S.A.). The result was that SHG NLOM images of fibrillar collagen types I and III in the adventitia and media were acquired at 1 Hz with 16-bit resolution in 1 micron steps through the thickness of the arterial wall (Fig. 2.2).

All NLOM images were processed using ImageJ, Continuity (courtesy Prof. A.D. McCulloch, UCSD), and Matlab. The curvature of the vessels and the flat optical imaging plane necessitated cropping to define appropriate regions of interest (i.e., tangent planes) and thereby reduce error in interpretation (Fig. 2.2). All images were cropped in ImageJ to at most a 200 micron region in the circumferential direction. Images were then imported into Continuity and processed to mark individual fibers and determine their orientations within the z - θ plane. To normalize the data and better compare fiber distributions between optical slices, fiber angles were divided by the total number of angles marked within a slice. The resulting values represented the percentage of marked fibers at that angle in a slice, not mass fractions for oriented collagen. Differences in wall thickness between specimens also required normalization of the number of optical slices per vessel. For each of the slices across the arterial wall, collagen fiber orientations were compiled in Matlab by segregating fiber families and subsequently were averaged for comparison with values predicted by the constitutive model and values reported in the literature. Four averages were compared: (1) the average of all angles from 0° to 90° and 0° to -90° in sixteen characteristic adventitial

slices, (2) the average from 5° to 85° and -5° to -85° for sixteen characteristic adventitial slices, (3) the average from 5° to 85° and -5° to -85° for 21 characteristic medial slices, (4) and a weighted average of values from averages (2) and (3) with weighting factors in Table 2.1 used to account for different thicknesses and collagen densities in the media proper, the outer part of the media having no smooth muscle cells, and the adventitia [9]. In all cases, absolute values were taken of the negative angles. Finally, note that orientations for the diagonal fibers at 80 mmHg, computed from the NLOM images, were denoted as α_{80} and converted to associated values α_o assuming that fibers deform according the overall stretches (i.e., $d\mathbf{x} = \mathbf{F}d\mathbf{X}$ where \mathbf{F} is the deformation gradient tensor in 2-D), whereby

$$\alpha_o = \tan^{-1} \left(\frac{\lambda_z}{\lambda_\theta} \tan \alpha_{80} \right). \quad (2.10)$$

Table 2.1 Weighting factors used to average measured collagen fiber angles. The average angle and wall thickness of each layer was obtained directly from NLOM data (Fig. 2.4) whereas the percentage of extracellular matrix was estimated from Rowe et al. (2003). The average area under the histogram was calculated from NLOM data based on a characteristic histogram slice excluding the range $\pm 5^\circ$ from axial and circumferential. This value was included to account for differences in abundance of diagonal fibers between the adventitia and the media.

	Average Angle (degrees)	Wall Thickness (normalized)	% Matrix Relative to Skin (Rowe et al. 2003)	Average Area Under Histogram (without axial and circumferential)
Adventitia	24.0	1/3	100	0.83
Outer Media	77.5	1/15	100	0.52
Media	77.5	9/15	35	0.52

RESULTS

Pressure-diameter and axial force-pressure data at the mean axial stretch of 1.15 exhibited characteristic nonlinear responses qualitatively similar to those of extracranial arteries (Fig. 2.3). As expected, apparent specimen-to-specimen variations in the pressure-diameter data were lessened by normalizing diameter using values from the preconditioned unloaded state (i.e., using the circumferential stretch ratio at the outer surface), which facilitated comparisons and averaging (not shown). Activation of the smooth muscle with 60 mM KCl caused the pressure-diameter curve to shift leftward, with the appearance of an inflection point around 15 mmHg, and reduced the axial force slightly (Fig. 2.3). At higher pressures, the active and passive curves had similar shapes and slopes. Although not shown, data from vessels having a “basal tone” were nearly identical to passive data recorded in a calcium-free solution. Finally, note that the basal circumferential stress-stretch relation was characteristically nonlinear with stress on the order of 100 kPa at physiologic conditions.

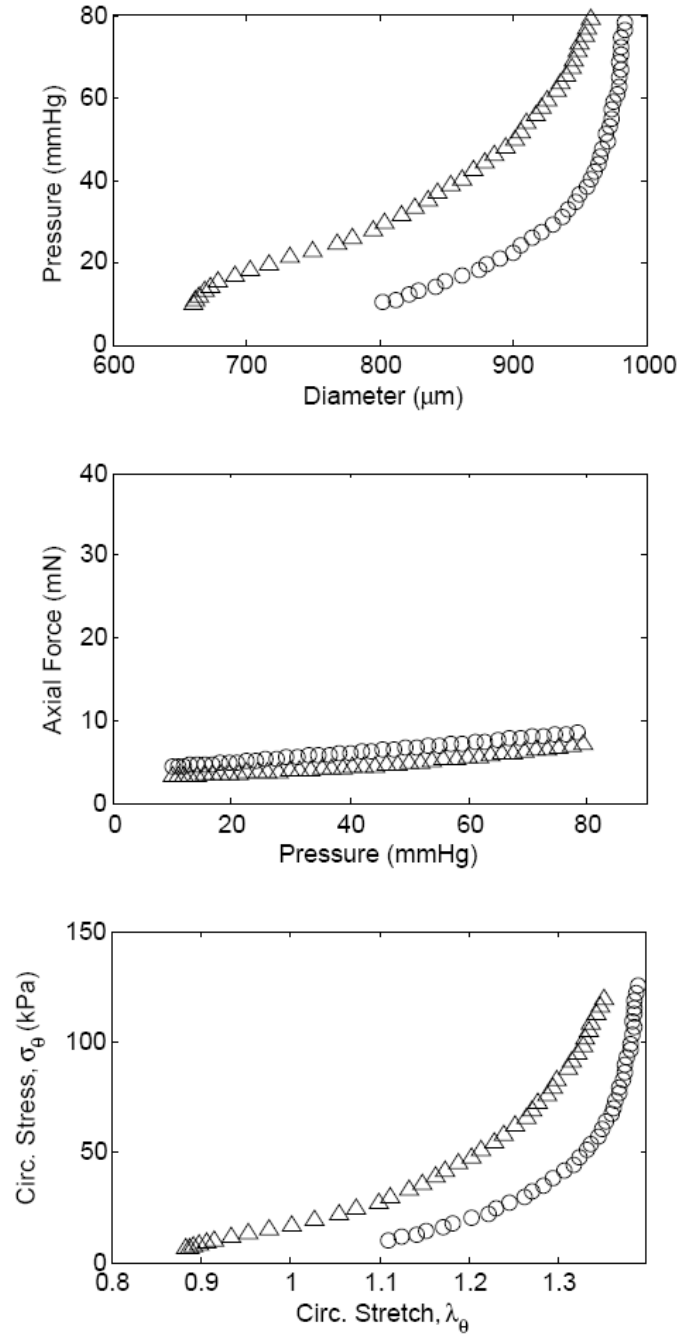


Fig. 2.3 Characteristic data from active/passive experiments. (axial stretch = 1.15) (top) Pressure-diameter data. At lower pressures the active curve (' Δ ') is shifted leftward of the passive curve (' \circ '). An inflection point can be seen around 15 mmHg. (middle) Axial force-pressure data. Force plotted is the total force. The axial force was less for the active vessel than the passive vessel at all increasing pressures. (bottom) Mean circumferential stress and stretch data. At lower pressures the active curve is shifted to left of the passive curve.

Extensive numerical studies revealed that using the four-fiber family model, experimental data were best fit with either six parameters ($c, c_1^{1,2}, c_2^{1,2}, c_1^{3,4}, c_2^{3,4}, \alpha_o$) or five parameters (same except α_o specified from NLOM as noted below). That is, fits were better when $c_1^1 = c_1^2$ and $c_2^1 = c_2^2$ (cf. [33]), not when families 1 and 2 had individual sets of best-fit values. Best-fit material and structural parameters for the eight specimens tested are given in Table 2.2 along with the mean values. Comparison of data to predicted responses are illustrated for a representative specimen (Fig. 2.4), which reveals a reasonable description of the data based on a best-fit value of $\alpha_o = 36.9$ (i.e., $\alpha_{80} = 40.3^\circ$).

Table 2.2 Best-fit material parameters from 4FF model fits. Mean and standard deviation of each parameter are listed below.

Specimen	e	c (kPa)	$c_1^{1,2}$ (kPa)	$c_2^{1,2}$	$c_1^{3,4}$ (kPa)	$c_2^{3,4}$	α_o
1	0.15	5.76E-10	0.01	6.15	23.35	0.83	38.7
2	0.13	2.51E-08	0.06	18.84	26.10	3.53	48.6
3	0.18	1.46E-07	0.30	9.93	13.86	5.14	51.9
4	0.16	1.45E-07	3.26	3.17	22.43	4.45	31.9
5	0.15	1.25E-10	0.06	7.99	35.46	0.71	42.7
6	0.17	2.35E-10	2.20	3.04	28.43	1.44	36.6
7	0.14	4.22E-07	2.82	4.39	39.26	0.54	39.3
8	0.15	2.31E-07	6.48	2.41	11.86	8.46	26.3
Mean	0.15	1.21E-07	1.90	6.99	25.09	3.14	39.5
Std	0.01	1.50E-07	2.29	5.46	9.50	2.80	8.4

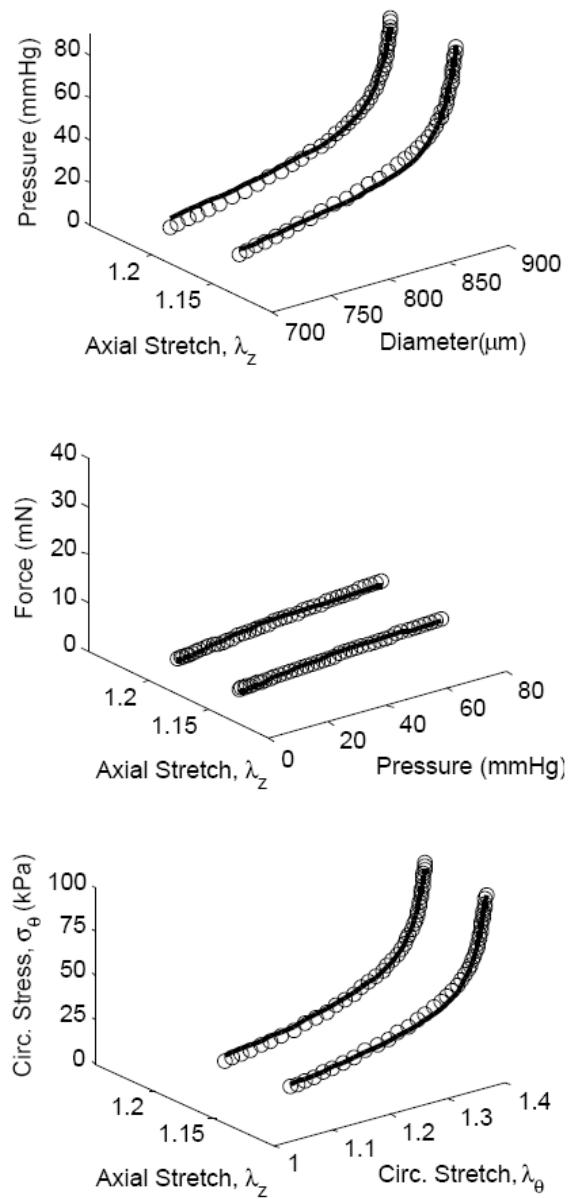


Fig. 2.4 Representative experimental data (open circles, with two thirds of the data removed for clarity when plotting) and 4FF model fits (solid lines) at axial stretches of 1.15 and 1.2. (top) Pressure-diameter. (middle) Axial force-pressure, with force plotted as the total force. (bottom) Circumferential stress-stretch.

Illustrative optical slices from one vessel maintained separately at three pressures and an axial stretch of 1.15 displayed the expected decrease in collagen undulation as pressure increased (Fig. 2.5), recalling again that images are oriented so that horizontal and vertical directions correspond to axial and circumferential orientations, respectively. Images (a) through (e) at each of the three pressures reveal further the transmural splay in collagen from adventitia to media. In particular, note that image (d) suggests a dramatic transition from more axially oriented fibers to circumferentially oriented fibers at all three pressures. The voids between the circumferentially oriented fibers in images (d) and (e) likely reflect the positions of the medial smooth muscle cells, which are not imaged by SHG but occupy about 70% of the media [5]. Note, too, the almost undetectable undulation of collagen fibers at a transmural pressure of 80 mmHg, even in the adventitia, which suggests that these fibers are load bearing at this pressure. Moreover, the diameters of the collagen fibers appear to be greater in the adventitia than in the media, although this was not quantified. Finally, images (d) and (e) also support the image cropping used during processing and analysis. As a result of vessel curvature in the circumferential direction, the center of the images progress to the medial layer faster than the top and bottom of the images (recall Fig. 2.2). Visual inspection of the images confirmed that for the pressurized rabbit basilar artery, 200 microns (roughly 1/5 of the pressurized diameter) provided a sufficient region of interest for analysis while removing significant effects of vessel curvature.

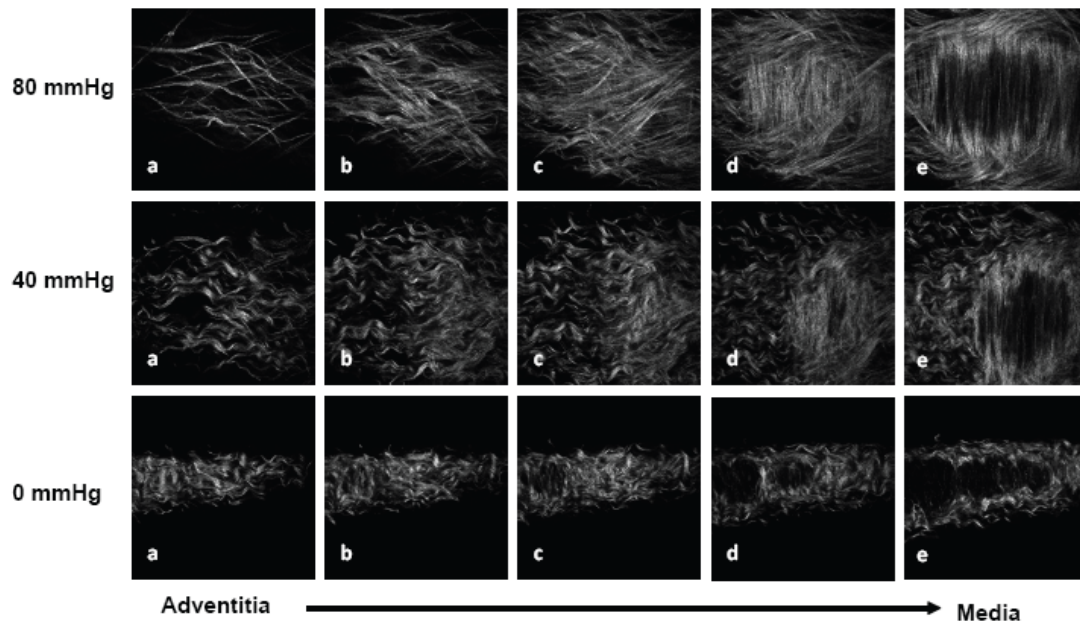


Fig. 2.5 NLOM SHG optical slices (uncropped) from a representative basilar artery imaged at 0, 40 and 80 mmHg. (axial stretch = 1.15) Images (a) through (e) for each pressure represent a sampling of slices from the adventitia to the media. The images are oriented so that the horizontal direction is the axial direction of the artery and the vertical direction is the circumferential direction. In particular, note the increased undulation with decreased pressure, the black voids in the media, which likely indicate where the smooth muscle cells reside, and the dramatic shift in orientation from axial to circumferential fibers. Again note the need for image cropping to get more consistent measurements of fibers within the same layer.

Orientations of the collagen fibers within corresponding slices from six vessels maintained at a pressure of 80 mmHg and an axial stretch of 1.15 were averaged and plotted in a three dimensional histogram (Fig. 2.6). The normalized position through the wall indicates positions from the outermost adventitia (0) to the inner media (1). Constituents within the inner wall, such as the basement membrane, internal elastic lamina and smooth muscle, were not imaged by second harmonic generation and thus are not represented. Collagen fibers in the adventitial region were distributed primarily around the axial direction (0°), whereas fibers in the media were oriented nearly circumferentially ($\pm 90^\circ$). These marked differences in collagen orientation are revealed further by characteristic slices from adventitial and medial regions (Fig. 2.7). The medial slices were bimodal ($\pm 90^\circ$), thus, negative angles were converted to positive with the addition of 180° to compare widths of the fiber distributions. Specifically, for comparison with ‘helical angles’ in the literature (e.g., [34]), sixteen characteristic optical slices were chosen from the adventitial region and all angles between 0° and 90° and all absolute values of angles from -90° to 0° were averaged together, resulting in a mean $\alpha_{80} = 20.2^\circ$. An average value was also calculated from the adventitial data when excluding angles corresponding to the axial and circumferential fiber families (-5° to 5° , -85° to -90° , and 85° to 90° removed), resulting in a value of 24.0° . A similar average calculated from 21 characteristic medial optical slices (-5° to 5° , -85° to -90° , and 85° to 90° removed) resulted in a value of 77.5° . For a meaningful comparison with model-calculated values of α_{80} (Eq. 2.10 and Fig. 2.2), the adventitial mean of 24.0° and the medial mean of 77.5° were weighted (Table 2.1) and averaged, resulting in an overall

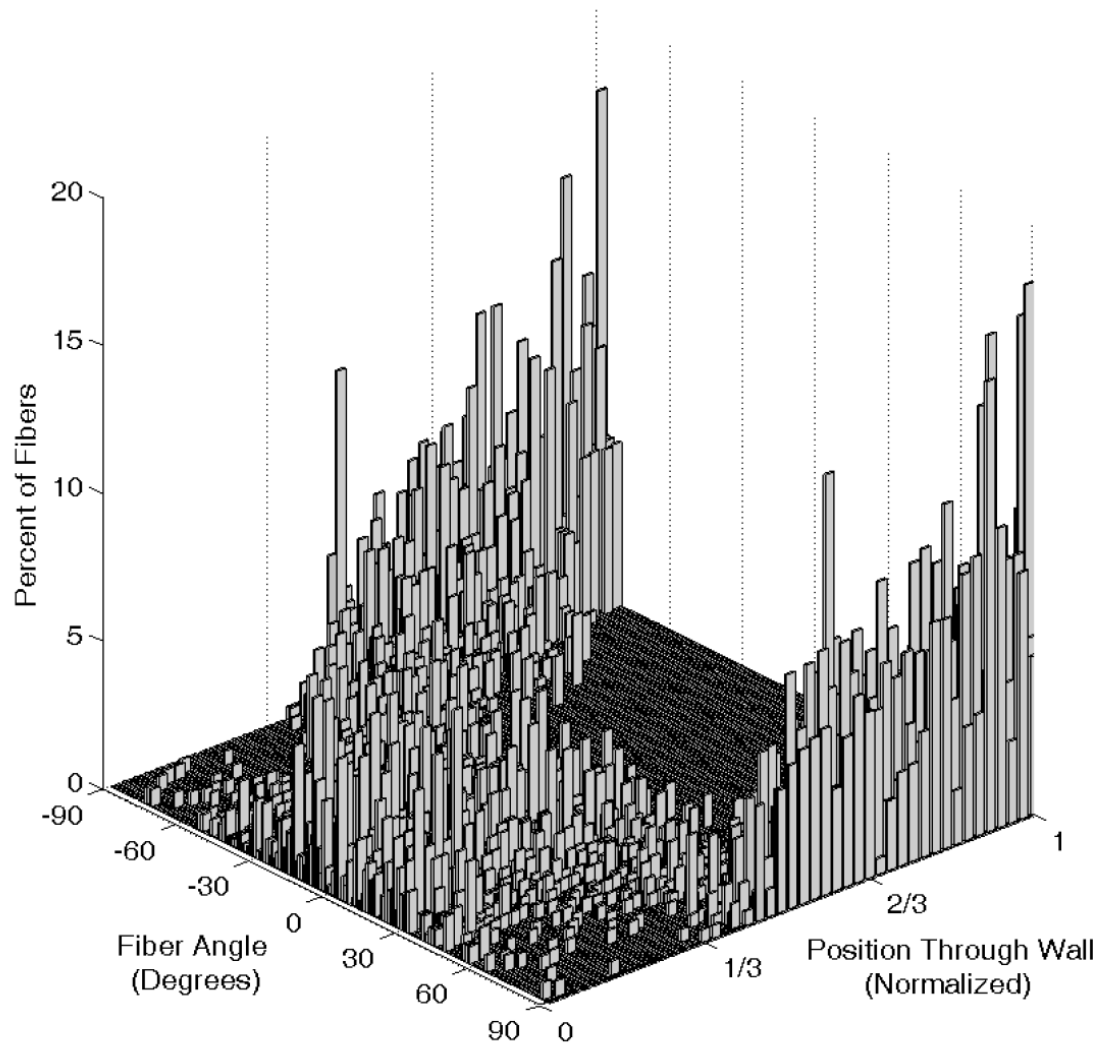


Fig. 2.6 Three-dimensional histogram of normalized and averaged NLOM data sets. (n of 6, axial stretch = 1.15, and pressure = 80 mmHg) The 'Position Through Wall' begins with 0, marking the outer adventitia, and ends with 1, marking the inner media; constituents within the intima were not captured with second harmonic generation and are not represented. The 'Fiber Angle' axis is oriented so that 0° is axial and $\pm 90^\circ$ is circumferential. Note the relative heights of the columns in respective layers do not represent fractional composition of collagen at that slice. For example, the higher columns in the medial layer slices seem to suggest the presence of higher levels of collagen in this layer, yet the opposite is true. See text for analyses that normalize data to account for the number of fibers marked in each slice.

mean fiber angle of 42.2° (at 80 mmHg and an axial stretch of 1.15, computed relative to the axial direction). The mechanical response of the four-fiber family model with a fixed $\alpha_o = 38.7^\circ$, corresponding to an $\alpha_{80} = 42.2^\circ$ (recall Eq. 2.10), and associated best-fit material parameters revealed a similarly good fit to data (cf. Fig. 2.4) when plotted against measured biaxial data (Fig. 2.8), as well as similar parameter values (Table 2.3).

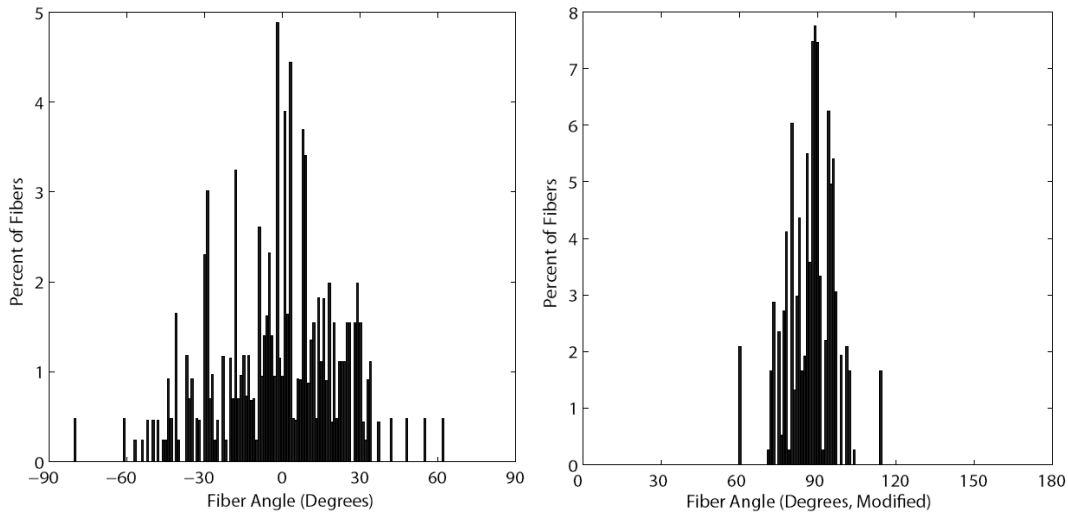


Fig. 2.7 Distribution of fiber orientations within characteristic slices. (left) Representative adventitial layer. The ‘Angles’ axis is oriented so that 0° corresponds to the axial direction and $\pm 90^\circ$ is the circumferential direction. (right). Representative medial layer. Note that angle is given as an absolute value.

Table 2.3 Best-fit material parameters from 4FF model fits with α_{80} fixed at 42.2°. Mean and standard deviation of each parameter listed below.

Specimen	e	c (kPa)	$c_1^{1,2}$ (kPa)	$c_2^{1,2}$	$c_1^{3,4}$ (kPa)	$c_2^{3,4}$
1	0.15	1.38E-08	4.98E-03	6.20	23.33	0.84
2	0.28	1.86E-07	1.41	11.36	19.70	3.33
3	0.45	1.29E-08	0.35	12.28	12.35	5.05
4	0.22	1.24E-06	0.03	8.38	24.00	3.93
5	0.17	4.13E-08	0.82	4.97	33.06	0.71
6	0.17	4.29E-08	0.97	3.81	30.71	1.29
7	0.14	2.48E-07	1.56	5.36	43.11	0.29
8	0.35	1.02E-08	2.75E-06	19.77	21.50	4.70
Mean	0.24	2.24E-07	0.64	9.02	25.97	2.52
Std	0.11	4.20E-07	0.64	5.31	9.43	1.94

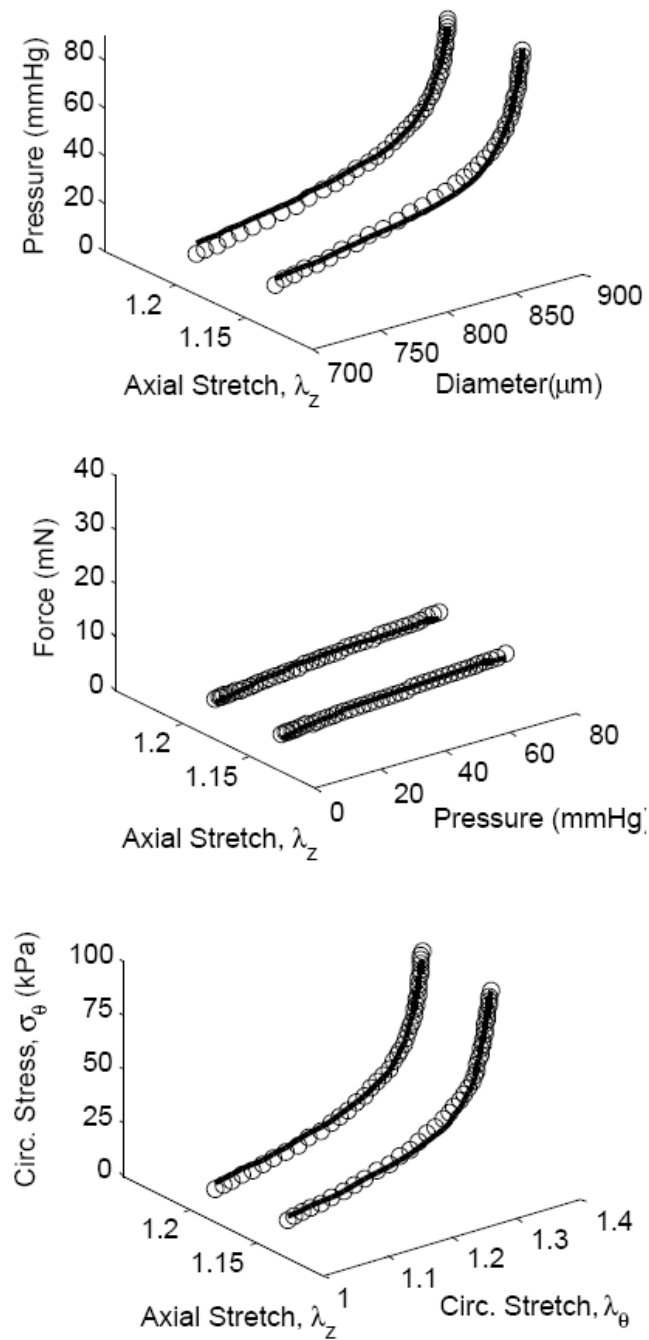


Fig. 2.8 Representative experimental data (open circles, with two thirds of the data removed for clarity when plotting) and 4FF model fit (solid lines) with a fixed mean fiber angle. $\alpha_0 = 38.7^\circ$, determined from NLOM (corresponding to a measured $\alpha_{80} = 42.2^\circ$ at an axial stretch of 1.15). Compare to the similar fit-to-data in Fig. 2.4, which was based on an estimation of the mean fiber angle via the nonlinear regression. Force plotted is the total force.

DISCUSSION

Data from Hayashi et al. [13, 14] and Monson et al. [44, 45] reveal marked differences between intracranial and extracranial human arteries: intracranial vessels exhibit a higher circumferential stiffness, less axial extensibility, and paradoxical decreases in stiffness with aging. Although these findings provide important information, they are limited by the use of simple measures of stiffness or uniaxial testing. To gain a more complete perspective of the biomechanics of the cerebral vasculature, from which one can interpret normal function or quantify consequences of pathologies such as vasospasm, it is necessary to catalogue biaxial responses under physiologic conditions and to formulate associated nonlinear constitutive relations for the stress response. Values of circumferential and axial stress at 80 mmHg and 1.15 stretch were on the order of 100 kPa and 40 kPa, respectively, for the rabbit basilar artery, a vessel of importance in animal models of cerebral vasospasm but not well studied biomechanically. For comparison, Hayashi et al. [13] reported circumferential stresses of 196 kPa and 98 kPa for basilar arteries from young and old humans tested at 100 mmHg. Although they did not report the prescribed axial stretch, they noted that the higher stresses in younger humans were due to a thinner wall. There are few other data on basilar arteries to which to compare the present findings.

It is important, of course, to preserve the *in vivo* geometry and to mimic normal applied loads during *in vitro* testing. Measurements of axial force on an intact cylindrical specimen can, for example, confirm *in vivo* axial stretch conditions and enhance our understanding of the overall biaxial mechanical behavior. Numerous biomechanical

studies have been reported on rings excised from basilar arteries (e.g., [21]), but these do not provide biaxial information on the biomechanics despite providing information on the pharmacology and characteristic behaviors [28]. At in vivo axial stretches, axial force remains nearly constant in extracranial arteries despite changes in pressure [43, 49], which was found for the basilar artery at a stretch of 1.3 (data not shown). One obstacle to mimicking the in vivo pressure loading on the basilar artery was the extensive side branches. We found that combining ligation of large branches using surgical silk and microsphere occlusion of small branches via bolus injections (Fig. 2.1) successfully stabilized transmural pressure and isolated the intraluminal and extraluminal environments. This method for pressure stabilization is much faster than ligation alone and less detrimental to living tissue than cauterization [20]. Less manipulation of the tissue and time under a microscope also reduces chances of tissue degradation or smooth muscle cell death. Finally, the microspheres appeared to have negligible effects on the mechanical response of the artery, that is, responses were largely uniform along the length of the vessel regardless of the location of the microspheres.

Extraluminal application of 60 mM KCl at the an axial stretch of 1.15, a pressure of 7 mmHg, and no flow proved effective in producing a constriction of ~30% in most specimens and served as a quick and reversible way to judge overall viability. The 30% contraction in response to high KCl at low transmural pressure correlated well with trends reported by Ohta et al. [20]. Mechanical testing under maximal contraction also provided data for quantifying the contractile capacity of the wall (Fig. 2.3), though this

was beyond the present scope. Quantification of contractility and alterations therein will prove necessary for data interpretation for tests on vasospastic vessels.

As constitutive relations continue to advance in complexity, there is increasing need to include better microstructural information on individual constituents within the wall. Not only does the microstructure dictate normal biomechanical behavior, it plays a key role in arterial adaptations to altered loading in vivo as well as disease progression via growth and remodeling processes [28]. As the primary load-bearing constituent within the arterial wall, quantification of the orientations and distributions of collagen fibers plays a particularly important role in the formulation of constitutive relations. Despite a historical dismissal of the mechanical contribution of adventitial collagen in cerebral arteries under physiologic conditions, Canham et al. [50] and Rowe et al. [9] suggested that the adventitia contributes significantly at and above physiologic pressures. Indeed, Rowe et al. [9] proposed that the normal adventitia contributes as much as one-third of the circumferential strength and all of the axial strength. Our NLOM images collected under physiologic loads (Figs. 2.2 and 2.5) confirm the presence of straightened (i.e., significantly load bearing) adventitial collagen fibers, thus implicating their significant mechanical contribution under normal conditions and motivating a more thorough consideration of the adventitia in cerebrovascular mechanics.

NLOM can provide unique information on arterial collagen within intact, living vessels maintained in their in vivo geometry and subjected to multiple clinically relevant loading conditions. The ability to image sequential layers throughout the vascular wall at

multiple pressures and axial stretches enables quantification of collagen fiber orientation as a function of both radius and deformation. Subsequent extraction of fiber angles with available software such as Continuity is simple in comparison to methods needed for polarized light microscopy [33, 34, 50]. NLOM also removes many of the limitations that make measuring angles of axially oriented fibers in standard histological cross-sections difficult, including the inevitable shrinkage of fixed specimens [9]. Fiber orientation depends strongly upon pressure and stretch (Eq. 2.10), variables that cannot be varied in polarized light microscopy due to pressure fixation, embedding, and sectioning. Utilization of NLOM in organ culture will likewise be ideal as the vessel remains intact and requires no staining. Until now, detailed information regarding the specific orientation of collagen fibers in the media and adventitia have not been catalogued fully for the basilar artery.

Data suggested a demarcation in fiber orientations between the media and the adventitia (Fig. 2.6). Moreover, image slices just past a 1/3 depth into the wall showed both axial and circumferential fibers, which seem to suggest a transition region between the adventitia and media. Although this interpretation could reflect an artifact due to the cylindrical geometry of the vessel, it could also represent the smooth muscle cell-free outer media described by Rowe et al. [9], which they suggested may play a role similar to the external elastic lamina that exists in extracranial arteries. We note, nonetheless, that cropping the images to 200 microns maximum in the circumferential direction significantly reduced effects of vessel curvature, but did not eliminate these effects (Fig. 2.2). Indeed, visual inspection of all images suggested a demarcation between the two

layers with little, if any, transition zone, and the dramatic differences in mean angles further supports the structural distinction between the adventitia and media. Clearly, there is a need for further study of this potentially important microscopic feature.

Finlay et al. [34] qualitatively described medial collagen as highly aligned about a circumferential direction and adventitial collagen as widely distributed about a mean axial direction, an assessment supported by the present NLOM data (Fig. 2.5). The mean fiber angle throughout the medial layer, near 90° in every slice herein (Figs. 2.6 and 2.7), correlates well with the mean orientation in the media of 88° reported by Finlay et al. [34]. They also report a mean helical orientation for the adventitial layer of 37° at 120 mmHg, which differs from our value of 20.2° at 80 mmHg and an axial stretch of 1.15. This discrepancy could be due in part to previously discussed potential differences introduced via pressure fixation and sectioning, different axial stretches, or differences between species (human vs. rabbit).

The mean experimentally determined collagen fiber angle α_o , determined via Eq. 2.10 and NLOM, was fixed within the structurally-based four-fiber family constitutive relation (Eqs. 2.5 to 2.8) and best-fit values of the material parameters $(c, c_1^{1,2}, c_2^{1,2}, c_1^{3,4}, c_2^{3,4})$ were determined via nonlinear regression using basal stress-stretch data. Results were very similar to those obtained via nonlinear regression of the same data when the mean fiber angle was one of the estimated parameters, thus providing a consistency check between the structural and mechanical modeling. Other α_o values determined via Eq. 2.10 and NLOM resulted in comparable fits (data not shown), which was to be expected because they fell within the standard deviation for

values found via the nonlinear regression (Table 2.2). Clearly, prescribing measured values of the structural parameters is preferred when possible, thus highlighting another strength of combining NLOM and biomechanical testing. Albeit only structurally-motivated, not microstructurally derived, the four-fiber family model was chosen over purely phenomenological models due to its attention to microstructural components and potential use in models of arterial growth and remodeling wherein one must model turnover of individual constituents [40]. Because this four-fiber family model estimated well the mean fiber angle (for the diagonal families) directly from biomechanical data and correctly estimated that the relative contribution of elastin was small (see value of c in Table 2.2, noting that cerebral arteries contain little medial elastin; [5]), it appears that the model faithfully represented salient microstructural features (note: unpublished results using the same constitutive relation, regression methods, and types of biaxial data for carotid arteries resulted in much larger values of c consistent with the greater percentage of elastin in carotids). This finding is also very encouraging for microstructural information will not be available in many clinical situations wherein constitutive relations will need to be estimated [51]. Finally, we note that the original two-fiber family model of Holzapfel et al. [48], with only diagonal collagen families, did not describe the biaxial data well (results not shown). In hindsight, this was to be expected given the strong circumferential and axial orientations of collagen in addition to diagonal families (Fig. 2.4). Indeed, Gasser et al. [52] showed numerically that the two-fiber family does not provide realistic descriptions of wall mechanics under particular loading conditions. They, in turn, suggested that the collagen be modeled

using von Mises' distributions about the two diagonal fiber directions, but this does not appear to be supported for the basilar artery based on the predominant circumferential and axial fibers revealed by NLOM, hence the use of a four-fiber family model [47] herein.

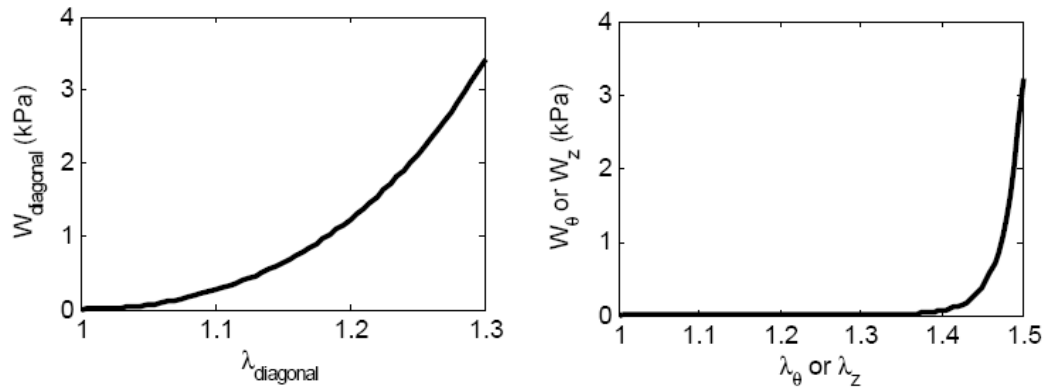


Fig. 2.9 Computations of representative energy storage for the two primary sets of fiber families as a function of fiber stretch. (top) Diagonal fibers. (bottom) Axial-circumferential fibers. The stored energy was calculated using constitutive forms in Eq. 2.5 and parameter values from Table 2.2 Values of $\lambda_{\text{diagonal}}$ are plotted from 1 to 1.3 as these are the values reached during cyclic pressurization.

An unexpected result from the regressions was that the best-fit to data was obtained when fiber families 1 and 2, that is the axially and circumferentially oriented fibers, had the same values of material parameters. Although it is not clear from the NLOM images why this was the case, this finding is consistent with results of Hu et al. [33] for porcine basilar arteries even though specific values of the parameters differ between the two species. In particular, it was found herein that best-fit values for the pair $(c_1^{3,4}, c_2^{3,4})$ for the diagonal fibers differed considerably from the pair $(c_1^{1,2}, c_2^{1,2})$ for the

axial and circumferential fibers. One way to visualize these differences is to plot the energy stored in each family of fibers as a function of its stretch. As it can be seen (Fig. 2.9), the primary difference is that the diagonal fibers have a gradually stiffening nonlinear response whereas the axial and circumferential fibers exhibit much more dramatic stiffening – initially very compliant, then very stiff. Fig. 2.9 would suggest, therefore, that all fibers are load bearing under physiologic conditions but that the diagonal fibers would bear most of the load at low (non-physiologic) pressures. Of course, the diagonal fibers contribute to both the overall axial and circumferential stiffnesses, hence the tissue-level response results from a complex mixture of all families, particularly under physiologic conditions. Nevertheless, the classical interpretation of 1-D (i.e., individual fiber) behaviors such as seen in Fig. 2.9 is that significant compliance followed by rapid stiffening results from similarly, highly undulated fibers that become very stiff only when straight. Such an interpretation would seem to be contrary to the NLOM images where adventitial (primarily axial and diagonal) collagen is seen to be undulated at lower pressures while medial (primarily circumferential) collagen is straight (Fig. 2.5). It is generally thought that medial collagen is a type I/III mixture whereas adventitial collagen is primarily type I (e.g., [4, 9]). Type I collagen is significantly stiffer and therefore can bear greater load than the more compliant type III collagen. Our results suggest that type I collagen is partially load bearing even when undulated and that unloaded medial collagen may not undulate in the same manner as adventitial collagen, perhaps due to its close association with the smooth muscle. Such a situation offers a potential explanation for the disparate

parameter values for the diagonal versus axial-circumferential fibers and could motivate a possible grouping of parameters such as $(c_1^1 = c_1^3 = c_1^4, c_1^2, c_2^1 = c_2^3 = c_2^4, c_2^2)$, that is, letting only the circumferential fibers be distinct. Yet, nonlinear regressions using this grouping of fiber families produced comparable fits to the biaxial data using the four-fiber family model but much greater variability in values from specimen-to specimen (data not shown). Clearly, more study is needed to elucidate structure-function relations for arterial collagen, including the different types.

Until now it has not been possible to compare distributions of fiber orientations predicted by mathematical models to orientations measured throughout the wall of intact, living arteries. A parameter of particular interest is α_o , the mean pitch angle of diagonal fiber families in a reference configuration. A tacit assumption of the four-fiber family model is that a single mean fiber angle can model well the net effects of transmural variations in fiber angles throughout the wall. Indeed, one reason for adopting this assumption is that it has not been possible to collect information on transmural variations in the same vessel under multiple loading conditions. Clearly, NLOM enables such measurements and there is now a need to explore fully 3-D models based on transmural variations in fiber directions (which was done many years ago for muscle fibers in the heart, see Humphrey [28]). Nevertheless, simplified models often provide useful information, thus we compared results for the present four-fiber family model when the mean fiber angle for the diagonal fibers was computed based on a simple average versus based on a weighted average that accounts for the different thicknesses of the adventitia and media and the different collagen fiber densities in the

adventitia and outer media (which are roughly 3 times more densely packed with collagen than the media; [9]). Yet, this weighting did not dramatically affect the resulting mean value. For example, when all angles in the adventitia and media (excluding the near axial and circumferential fibers) were averaged, the resulting value of α_{80} was 43.0° , which was very similar to the value of 42.2° that was obtained via the weighting procedure and that provided a very good fit to the biaxial data (Fig. 2.5). This finding provides further confidence in the robustness of the current 2-D model. Of course, biomechanical models can serve two very different functions: increasing our understanding for purposes of improving clinical care at tissue-organ levels and contributing to our continued desire to understand underlying mechanobiological mechanisms at cell-matrix levels.

For many clinical applications, including surgical planning, requisite information about lumen caliber and altered arterial distensibility can be determined from computations of fluid-solid interactions that are based on 2-D models of the arterial wall [53]. That is, accurate hemodynamics can be computed from patient-specific geometric models based on reliable 2-D models of the structural stiffness of the wall, which faithfully capture salient features of arterial behavior such as presented herein. Indeed, in cases of normal arteries in which residual stresses tend to yield uniform distributions of stress across the arterial wall, 2-D models provide accurate estimates of wall stress. There is, nonetheless, a need to continue to refine our models to reflect accurately the complex, 3-D microstructure of the arterial wall to understand better the mechanobiology that results from cells sensing and responding to their local mechanical

environment, which can change spatially and temporally during growth and remodeling. Toward this end, the NLOM data presented herein reveal a need to formulate models of the complex transmural distributions of collagen fibers, perhaps within the context of multiple layers. Indeed, it may well be that the smooth muscle cells of the media experience a different mechanical environment than do the fibroblasts of the adventitia, and consequently that their mechanobiological responses may differ. Layer specific modeling has been explored previously despite the difficulty of mechanically separating and testing the media and adventitia. For example, von Maltzahn et al. [54] proposed a two-layer cylindrical model for the elastic behavior of carotid arteries, with the media assumed to be isotropic and the adventitia assumed to be anisotropic. Demiray et al. [55] similarly proposed a two-layered cylindrical shell model of the aorta, but with an orthotropic elastic medial layer and an isotropic elastic adventitial layer. Clearly, detailed structural information available via NLOM will help in future attempts to formulate potentially multi-layered, fully 3-D structurally-based models notwithstanding the continued potential clinical utility of 2-D models given the lack of patient-specific information on transmural microstructure and the important role of residual stress homogenizing transmural stress distributions.

In addition to vasospasm, many other disease conditions involve structural and functional adaptations of the cerebral vasculature, including intracranial aneurysms, atherosclerosis, hypertension, and sequelae to traumatic head injury. The computer-aided experimental methods and computational findings presented herein promise to lead to a better understanding of such conditions through a more detailed characterization of

normal arterial wall structure and mechanical behavior. These new stress-stretch data provide baseline mechanical characteristics for rabbit basilar arteries, a common model for cerebral vasospasm. Data from contracted arteries provide a framework for interpreting active wall mechanics and alterations therein due to vasospasm. Perhaps most importantly, quantified collagen fiber orientations contribute to our understanding of arterial behavior and will guide the development of detailed structurally-motivated or structurally-based constitutive models and eventually detailed models of arterial growth and remodeling that depend on significant turnover of fibrillar collagen.

CHAPTER III

DIFFERENTIAL PASSIVE AND ACTIVE BIAXIAL MECHANICAL BEHAVIORS OF MUSCULAR AND ELASTIC ARTERIES: BASILAR AND COMMON CAROTID

INTRODUCTION

The arterial tree reflects well the fundamental principle of biology that form follows function. Variations along the arterial tree in both geometry (i.e., caliber and wall thickness) and wall structure (e.g., relative distributions of elastin, collagen, and contractile smooth muscle) correspond well to spatial differences in local blood flow and pressure [56] and thereby reinforce the critical role of mechanobiological processes in arterial homeostasis and pathobiology [57]. Although these variations represent a nearly continuous spectrum, it is convenient to classify arteries as either elastic (characterized by concentric elastic lamellae within the media, which occupies most of the wall) or muscular (characterized by a smooth muscle rich media that is devoid of concentric elastic lamellae and by a collagenous adventitia that occupies nearly half of the wall). Given the longstanding appreciation of the different structure and function of elastic and muscular arteries, it is surprising that there has been little effort to compare directly the biaxial mechanical properties of these two classes of arteries, particularly from the same species or donor.

Notwithstanding remarkable clinical advances, cerebrovascular disease continues to be responsible for significant morbidity and mortality. Many such diseases cause, or are caused by, changes in the biomechanical properties of the associated arteries. There

is, therefore, a pressing need to understand better the biomechanics and mechanobiology of both intracranial arteries and the extracranial arteries that feed these vessels. In this paper, we present the first direct comparison of biaxial biomechanical behaviors of the basilar (a muscular artery) and common carotid (an elastic artery) arteries from the same species (rabbit), including both passive and active. To facilitate future utility of these findings, the data are reduced in terms of a validated four fiber family constitutive model of the passive behavior [30] and a new constitutive relation for the active response.

METHODS

All animal protocols were approved by the Institutional Animal Care and Use Committee at Texas A&M University. Following euthanasia with sodium pentobarbital, basilar and common carotid arteries were excised from male New Zealand white rabbits and were gently cleaned, cannulated, and mounted in our biomechanical testing device [41] following methods described in [58]. Tests were performed in MegaCell DMEM (Sigma), supplemented with 580 mg/L L-glutamine, 5% rabbit plasma, 200 U/L penicillin, 100 mg/L streptomycin, 50 mg/L glycine, 3 μ g/L CuSO₄, and 50mg/L ascorbic acid, unless otherwise stated. Once mounted, we recorded the nearly unloaded (axial stretch \sim 1, pressure \sim 7 mmHg) length and diameter. Note that the average in vivo axial stretch at mean arterial pressure was found previously to be 1.15 for the basilar arteries [58] whereas it was determined using methods described in [59] to be 1.68 for the carotid arteries. Vessels were then acclimated for one hour at the appropriate in vivo axial stretch, low pressure (7 mmHg for basilar, 40 mmHg for carotids), and low flow (6 ml/min for basilar, 20 ml/min for carotids). They were next preconditioned via

pressurization at multiple axial stretches: basilar arteries were cycled from 7 to 40, 60, and then 80 mmHg at axial stretches of 1.1, 1.15, and 1.2 whereas carotid arteries were cycled from 7 to 60, 100, and then 120 mmHg at the in vivo axial length and $\pm 10\%$ of this length. Unloaded length was measured again following preconditioning; if changed, its new value was used. For the thinner walled basilar arteries, both the inner and outer radii were recorded on-line at axial stretches of 1.1, 1.15, 1.2 and pressures of 7, 40 and 80 mmHg. Because the inner radius of the thicker walled carotid arteries could not be visualized while mounted in the test system, an adjacent unused section of vessel was cut into rings and unloaded wall thicknesses were recorded using a calibrated microscope. These values allowed inner radii to be inferred during testing, via incompressibility, from the other on-line measurements. Baseline conditions were in vivo axial stretch and a pressure of 80 mmHg for basilar and 120 mmHg for carotids.

Axial length, outer diameter, axial force, and luminal pressure were measured on-line throughout testing using information from the axial stepper-motors, a video caliper, and force and pressure transducers, respectively, and were recorded continuously via a custom LabView program [41]. One set of basilar arteries underwent 4 pressure-diameter cycles from 7 to 80 mmHg during which the axial stretch was held constant at 1.1, 1.15, and then 1.2; another set underwent the same pressure-diameter cycles at the in vivo stretch (1.15) alone. All carotid arteries underwent 4 pressure-diameter cycles from 7 to 120 mmHg during which the axial stretch was held constant at the in vivo value and then $\pm 10\%$ of that value. These initial mechanical tests were conducted at basal conditions meaning the level of smooth muscle tone was close to in vivo levels and not

intentionally altered. Following these mechanical tests, both types of vessels were exposed adventitially to 10^{-10} M endothelin-1 (ET-1) and allowed to acclimate for 15 minutes. They then underwent repeated mechanical testing at the in vivo axial stretch alone. This procedure was then repeated at three higher doses of ET-1 (10^{-9} , 10^{-8} , 10^{-7} M). After the final dosing of ET-1 and mechanical testing, the adventitial bath was drained, rinsed, and replaced with normal saline containing 10 μ L of 100 mM sodium nitroprusside (SNP) for a final concentration of 10^{-4} M. After a 30 minute acclimation period, the unloaded diameter was compared to prior values to verify that the vessel had relaxed actively. If the vessel still appeared to be active, an additional 10 μ L of SNP was added and 15 more minutes of acclimation were allowed until the vessel was passive. The vessel then underwent mechanical testing at the in vivo stretch for the final time.

Assuming incompressibility, the current inner radius can be computed from the current outer radius, r_o , current axial length, l , and mean wall volume, \bar{V} , using the equation

$$r_i = \sqrt{r_o^2 - \frac{\bar{V}}{\pi l}}. \quad (3.1)$$

As noted above, mean wall volume was calculated differently for the basilar and carotid arteries. Inner, \hat{r}_i , and outer, \hat{r}_o , radii were recorded within the device at six states for the basilar arteries and wall volume was calculated at each state via

$$V = \pi(\hat{r}_o^2 - \hat{r}_i^2)l. \quad (3.2)$$

Wall volume for carotid arteries was calculated using measurements of the cross section from 2 to 4 unloaded rings and the following equation,

$$V = \pi \left(R_o^2 - (R_o - \hat{h})^2 \right) L, \quad (3.3)$$

where R_o is the reference outer radius, \hat{h} is the measured wall thickness, and L is current axial length. For both basilar and carotid arteries, all resulting volume measurements were then averaged to calculate mean wall volume. From the calculated inner radii and data recorded during mechanical testing, mean circumferential and axial Cauchy stress and stretch were calculated via the equations,

$$\sigma_\theta = \frac{Pr_i}{h}, \quad \sigma_z = \frac{f}{\pi(r_o^2 - r_i^2)}, \quad (3.4, 3.5)$$

and

$$\lambda_\theta = \frac{(r_i + r_o)/2}{(R_i + R_o)/2}, \quad \lambda_z = \frac{l}{L}, \quad (3.6, 3.7)$$

where P is transmural pressure, h is current wall thickness, f is total axial force, and L is reference axial length.

As in [58], a four-fiber family strain energy function of the following form was used to model the passive data [30],

$$W = \frac{c}{2}(I_1 - 3) + \sum_{k=1,2,3,4} \frac{c_1^k}{4c_2^k} \left\{ \exp \left[c_2^k \left((\lambda^k)^2 - 1 \right)^2 \right] - 1 \right\}, \quad (3.8)$$

where I_1 is the first invariant of the right Cauchy-Green tensor, c is a material parameter that models the contribution of the elastin-dominated amorphous matrix (assumed to be isotropic) and c_1^k (kPa) and c_2^k are material parameters associated with the k^{th} fiber family. In particular, fiber family $k = 1$ represents axially oriented (0°)

collagen fibers, $k = 2$ represents circumferentially oriented (90°) collagen fibers plus passive smooth muscle, and $k = 3$ and $k = 4$ represent symmetrically oriented diagonal families of collagen fibers. Material parameters for the diagonal fibers are equal, meaning $c_1^3 = c_1^4$ and $c_2^3 = c_2^4$ [48]. Stretches experienced by the k^{th} fiber family are

$$\lambda^k = \sqrt{\lambda_\theta^2 \sin^2 \alpha_o^k + \lambda_z^2 \cos^2 \alpha_o^k}, \quad (3.9)$$

where α_o^k is the angle of the k^{th} fiber relative to the axial direction in a reference configuration. Mean circumferential and axial Cauchy stresses are thus

$$\sigma_\theta^{\text{Passive}} = c \lambda_\theta^2 \left(1 - \frac{1}{\lambda_\theta^4 \lambda_z^2} \right) + \lambda_\theta^2 \sum_{k=1,2,3,4} \left\{ c_1^k \left((\lambda^k)^2 - 1 \right) \exp \left[c_2^k \left((\lambda^k)^2 - 1 \right)^2 \right] \sin^2 \alpha_o^k \right\}, \quad (3.10)$$

and

$$\sigma_z^{\text{Passive}} = c \lambda_z^2 \left(1 - \frac{1}{\lambda_z^4 \lambda_\theta^2} \right) + \lambda_z^2 \sum_{k=1,2,3,4} \left\{ c_1^k \left((\lambda^k)^2 - 1 \right) \exp \left[c_2^k \left((\lambda^k)^2 - 1 \right)^2 \right] \cos^2 \alpha_o^k \right\}. \quad (3.11)$$

To account for active stress generated by the smooth muscle, we assumed additivity of active and passive contributions, that is, $\sigma_\theta^{\text{total}} = \sigma_\theta^{\text{active}} + \sigma_\theta^{\text{passive}}$ and $\sigma_z^{\text{total}} = \sigma_z^{\text{active}} + \sigma_z^{\text{passive}}$, and furthermore that the active stress response was separable in terms of length-tension and agonist dose-response parts, as, for example,

$$\sigma_\theta^{\text{active}} = T_M \sigma_\theta^{A1}(\lambda_\theta) \sigma_\theta^{A2}([\text{ET-1}]), \quad (3.12)$$

where [ET-1] is the concentration of the agonist, endothelin-1 in this case. Following a trial-and-error search of many candidate functions, we let

$$\sigma_\theta^{A1}(\lambda_\theta) = e^{-b \left(\frac{\lambda_M - \lambda_\theta}{\lambda_M} \right)^2} \quad (3.13)$$

$$\sigma_{\theta}^{A2}([ET-1]) = \frac{1}{1 + e^{-d(\log([ET-1]) + c)}} \quad (3.14)$$

where T_M (kPa) is the maximum stress generated by the smooth muscle, λ_M is the circumferential stretch at which active stress is maximal, and b , c and d are dimensionless parameters. Functions $\sigma_{\theta}^{A1}(\lambda_{\theta})$ and $\sigma_{\theta}^{A2}(\lambda_{\theta})$ were inspired by the works of Rachev and Hayashi [60] and Carlson and Secomb [61]. In particular, the latter work modeled the active length-tension relation using a Gaussian curve,

$$T_{act}^{\max}(L) = C_{act} \exp\left\{-\left(\frac{L/L_0 - C'_{act}}{C''_{act}}\right)^2\right\}, \text{ where } C_{act}, C'_{act}, \text{ and } C''_{act} \text{ are free parameters. Our}$$

model is similar, with these free parameters equivalent to T_M , λ_m , and λ_m / \sqrt{b} , respectively. We also used a sigmoid function to represent changing smooth muscle tone, but our relation depends on vasoconstrictor concentration [ET-1] rather than total vessel wall tension.

Active axial stress can similarly be assumed to be separable, namely

$$\sigma_z^{active} = \sigma_z^{A1}(\lambda_{\theta}) \sigma_z^{A2}([ET-1]). \quad (3.15)$$

An extensive trial and error search suggested a simple linear function for the length-tension relation,

$$\sigma_z^{A1}(\lambda_{\theta}) = -q\lambda_{\theta} + p, \quad (3.16)$$

where p (kPa) and q (kPa) are material parameters. The agonist dependent part again depended on vasoconstrictor concentration [ET-1],

$$\sigma_z^{A2}([ET-1]) = \frac{1}{1 + e^{-r(\log([ET-1]) + s)}}, \quad (3.17)$$

where r and s are dimensionless material parameters.

Best-fit values of material parameters were determined via nonlinear regression (Matlab functions `lsqnonlin` and `fminsearch`) to minimize the following objective function

$$e = \sum_{i=1}^N \left[\left(\frac{P_i^{th} - P_i^{exp}}{P_{average}^{exp}} \right)^2 + \left(\frac{f_i^{th} - f_i^{exp}}{f_{average}^{exp}} \right)^2 \right], \quad (3.18)$$

where N is the number of data points, ‘th’ denotes theoretically calculated, ‘exp’ denotes experimentally measured, and ‘average’ denotes an average over all specified data. All parameters were constrained to respect a lower bound of 0, but only α_o had an upper-bound ($\pi/2$). The parameters associated with the passive behavior were determined first from passive data alone, then the parameters associated with active behavior were determined simultaneously from the total data at all four concentrations of ET-1. To determine the ‘goodness’ of model predictions in both passive and active cases, the root mean sum of the square (RMS) and Akaike information criterion (AIC) were calculated based on differences in the experimentally inferred and computed Cauchy stresses, namely

$$RMS = \sqrt{\frac{1}{N} \sum_{i=1}^N (\sigma_{\theta}^{exp} - \sigma_{\theta}^{th})^2} + \sqrt{\frac{1}{N} \sum_{i=1}^N (\sigma_z^{exp} - \sigma_z^{th})^2}, \quad (3.19)$$

and

$$AIC = 2M + N \log(RSS), \quad (3.20)$$

where M is the number of parameters and

$$RSS = \sum_{i=1}^N \left(\sigma_{\theta}^{\text{exp}} - \sigma_{\theta}^{\text{th}} \right)_i^2 + \sum_{i=1}^N \left(\sigma_z^{\text{exp}} - \sigma_z^{\text{th}} \right)_i^2. \quad (3.21)$$

Outlier detection was performed on parameter values for both the passive and active fits. If a parameter, such as α_o , was distributed normally, its mean and standard deviation were calculated. Any value falling outside the range of the mean plus or minus two standard deviations was considered to be an outlier and the associated data set was removed. For non-normally distributed parameters, such as c , the log of the values was used to determine means and standard deviations. Data sets were similarly removed if a vessel was damaged during testing (e.g., exposure to excessive pressure or axial stretch) or if it did not constrict to ET-1.

Values of λ_M were calculated first by finding the maximum value of $\sigma_{\theta}^{\text{active}}$, where $\sigma_{\theta}^{\text{active}} = \sigma_{\theta}^{\text{total}} - \sigma_{\theta}^{\text{passive}}$ and $\sigma_{\theta}^{\text{passive}}$ was calculated using the passive fit and $\sigma_{\theta}^{\text{total}}$ was measured experimentally during “active tests.” Values were then averaged from all four concentrations of ET-1. These values were compared to those found via regression of data using the active model; this check served as a means to verify the physical reasonableness of the model.

Following Wicker et al. [58], images were taken of fresh segments of basilar and carotid artery using custom nonlinear optical microscopy [42]. Prior to imaging, the vessels were cannulated and loaded to in vivo values as defined previously. Images of collagen fiber orientation were taken at 1 micron steps through the thickness of the wall. Standard histology was also performed using fresh sections of basilar and carotid arteries that were fixed in 10% formalin for 1 hour. The vessels were then embedded in a frozen

embedding medium (Cryostat) and sectioned by the Veterinary Integrative Biosciences Histology Laboratory at Texas A&M. Hematoxylin and Eosin (H&E) and Verhoeff-Van Gieson (VVG) were used to assess general morphology and elastin, respectively. Differences in elastin content (or collagen to elastin ratio) frequently distinguish muscular from elastic arteries, particularly for intracranial versus extracranial arteries.

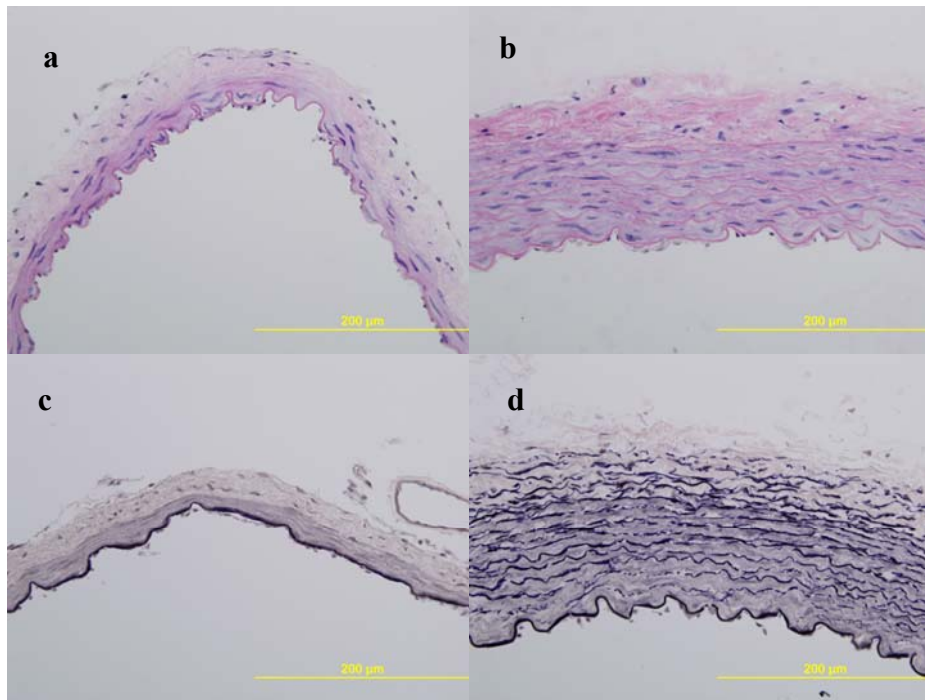


Fig. 3.1 Representative histological slices of basilar and carotid arteries with H&E (a, b) and VVG (c, d) staining.

RESULTS

Despite significant differences in unloaded radius and wall thickness, in vivo axial stretch, and both wall organization and composition (Table 3.1, Fig. 3.1), standard pressure-diameter tests revealed qualitatively similar nonlinear behaviors under a comparable “basal” tone for the basilar and carotid arteries (open triangles in Fig. 3.2 and 3.3). The carotids exhibited a slightly more ‘S-Shaped’ behavior, however; they also experienced slightly larger circumferential stretches at comparable transmural pressures (e.g., a λ_θ of 1.52 versus 1.47 at a common pressure of 80 mmHg) and they required larger axial forces to maintain their in vivo axial stretch, which was also significantly greater (1.68 versus 1.15). Yet, the average mean circumferential Cauchy stress was 20 kPa higher for basilar (124.71 kPa) than carotid (104.16 kPa) arteries at a common pressure of 80 mmHg. This difference appeared to result in part from the carotid having an unloaded thickness that was four times greater, but an inner radius that was only twice as large (Eq. 3.4; Table 3.1). The overall character of the Cauchy stress - stretch behaviors were nevertheless similar as seen in the figures.

As expected, the curves on the far right in both pressure-diameter and circumferential stress-stretch plots (Figs. 3.2 and 3.3) represent passive responses. Note, too, the progressively smaller diameters near zero pressure for increasing [ET-1]. That is, as expected, this progressive vasoconstriction tended to reveal itself via a leftward shift and appearance of an inflection point in the pressure-diameter data; circumferential stress-stretch plots showed more modest leftward shifts and monotonic responses. The axial forces required to maintain each vessel at a constant length during testing tended to

be qualitatively similar, but to decrease with increasing contraction, hence revealing biaxial effects in the active behavior. As expected, basal data fell between the passive and the exogenously activated $[ET-1] = 10^{-10}$ M concentration data in each case.

Table 3.1 Reference inner and outer radii, in vivo axial stretch, equivalent [ET-1] for basal tone arteries and calculated λ_M from basilar and carotid arteries. Mean values followed by standard deviations.

	Basilar	Carotid
R_i (μm)	282.25 ± 28.97	575.63 ± 61.07
R_o (μm)	346.4 ± 26.37	847.42 ± 79.00
H (μm)	64.16 ± 10.61	271.78 ± 34.30
$\lambda_z^{\text{in vivo}}$	1.15 ± 0.00	1.68 ± 0.12
$[ET-1]$ (M)	$3.59\text{E-}11 \pm 3.97\text{E-}11$	$3.56\text{E-}07 \pm 7.50\text{E-}07$
λ_M	1.35 ± 0.12	1.49 ± 0.07

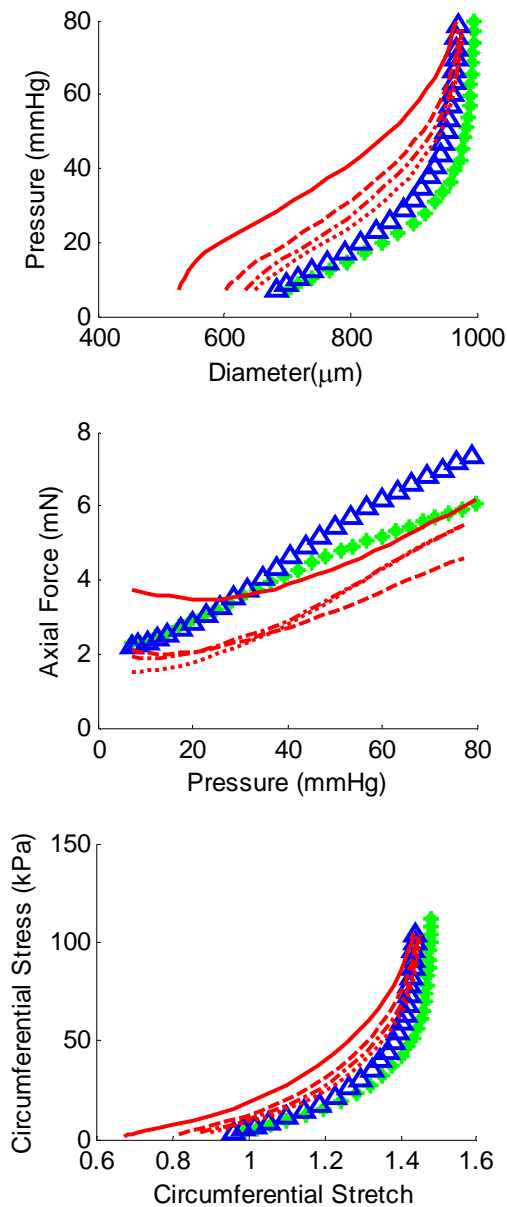


Fig. 3.2 Representative basilar artery data at passive ('+'), basal ('Δ'), and four levels of active tone. These were achieved by concentrations of ET-1: 10^{-10} ('...'), 10^{-9} ('-.-'), 10^{-8} ('- - -'), 10^{-7} ('—').

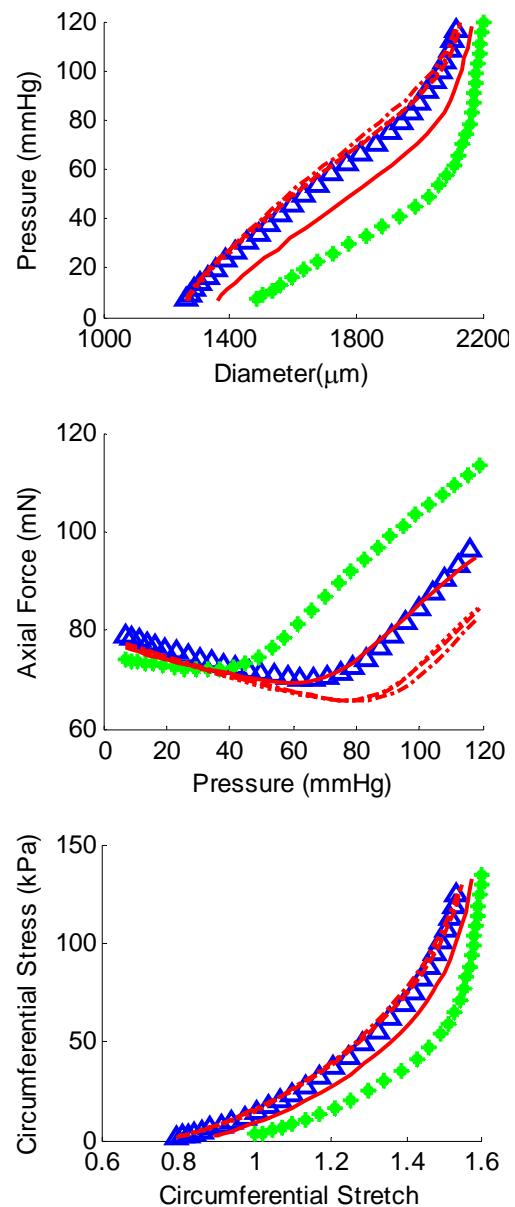


Fig. 3.3 Representative carotid artery data at passive ('+'), basal ('Δ'), and four levels of active tone. These were achieved by concentrations of ET-1: 10^{-10} ('...'), 10^{-9} ('-.-'), 10^{-8} ('- - -'), 10^{-7} ('—').

The ability of the four fiber family constitutive relation (Eqs. 3.8 to 3.11) to describe passive data (open circles) is shown in Figs. 3.4 and 3.5 for basilar and carotid arteries, respectively, with solid curves showing both the fits to pressure-diameter and axial force-pressure data and the predictions of circumferential stress-stretch behaviors. When comparing AIC values (not shown), it was found that the 8-parameter model (c , c_1^1 , c_2^1 , c_1^2 , c_2^2 , $c_1^{3,4}$, $c_2^{3,4}$, α_o) provided much better fits and predictions for both the basilar and carotids than did a prior 6-parameter version of this model [58]. Associated best-fit values of the parameters are listed in Tables 3.2 and 3.3 for basilar and carotid arteries, respectively. Note, in particular, the much lower value of the parameter c (which is meant to model the elastin-dominated portion of the extracellular matrix) for the basilar compared with the carotid artery, which is consistent with its lower elastin content (Fig. 3.1).

Recalling that this constitutive model (Eqs. 3.10 and 3.11) is essentially two-dimensional, consistent with a transmural homogenization, it is interesting that best-fit values of the diagonal fiber angle (Tables 3.2 and 3.3) were similar for the basilar and carotids despite different transmural distributions of collagen fiber angles measured using NLOM (Fig. 3.6).

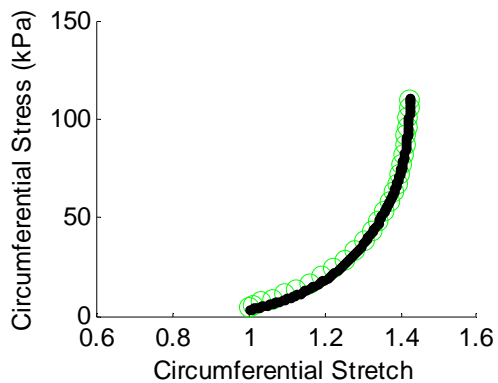
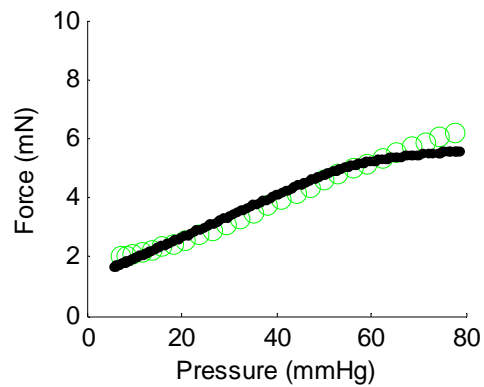
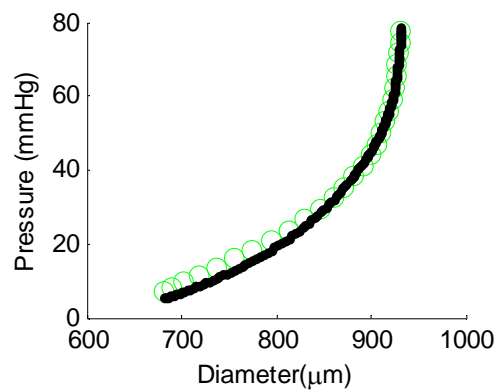


Fig. 3.4 Representative passive basilar artery data (—) and 4FF model fits (‘o’).

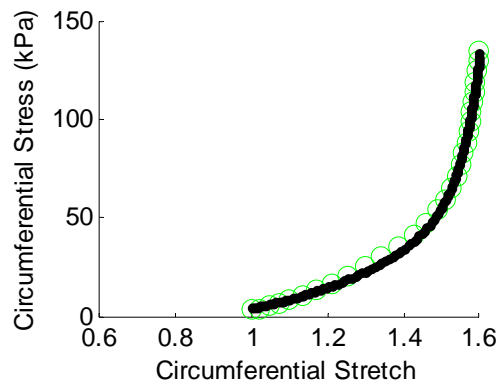
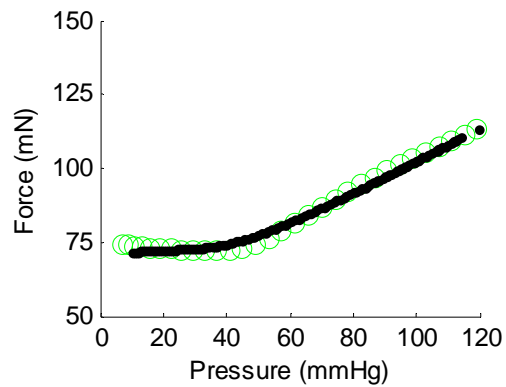
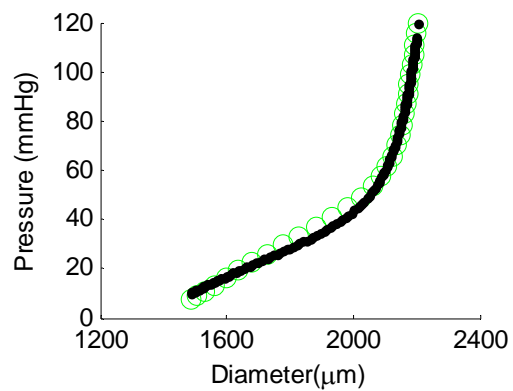


Fig. 3.5 Representative passive carotid artery data (—) and 4FF model fits (‘o’).

Table 3.2 Best-fit parameters for passive basilar data 4FF model fits. Mean and standard deviation of each parameter are listed below.

Specimen	c	c_1^1 (kPa)	c_2^1	c_1^2 (kPa)	c_2^2	$c_1^{3,4}$ (kPa)	$c_2^{3,4}$	α_0	RMS
1	3.07E-05	6.10	14.30	6.33E-06	7.44	18.11	0.66	50.64	3.47
2	5.49E-06	7.51	12.45	3.09E-07	16.66	23.15	1.34	50.42	4.06
3	1.37E-05	18.70	0.14	1.28E-07	10.55	18.30	0.78	50.93	4.06
4	1.30E-06	21.49	0.71	1.57E-03	4.86	12.34	0.37	59.38	1.80
5	6.63E-05	12.71	3.47	4.35E-09	15.16	11.11	1.19	55.95	5.21
6	2.99E-05	5.40	2.06	2.50E-05	8.79	25.58	0.83	46.97	5.03
7	3.34E-05	0.10	11.45	4.57E-03	3.85	23.40	0.01	45.97	4.63
8	1.21E-04	13.89	2.83	7.61E-04	5.15	15.11	0.22	55.56	1.69
9	3.09E-07	1.11	28.00	1.79E-03	8.16	18.10	0.42	61.57	1.81
10	2.16E-06	4.86	14.18	2.47E-03	6.32	24.12	0.45	46.24	5.11
11	5.30E-05	1.42	0.00	2.24E-09	15.64	13.94	1.98	44.96	6.31
12	7.79E-06	15.94	3.43	4.46E-06	3.37	23.88	0.33	53.83	3.29
Mean	3.24E-05	8.48	8.15	1.02E-03	9.32	18.48	0.75	51.69	3.93
Std Dev	3.65E-05	7.24	8.78	1.48E-03	4.59	5.02	0.57	5.68	1.57

Table 3.3 Best-fit parameters for passive carotid data 4FF model fits. Mean and standard deviation of each parameter are listed below.

Specimen	c	c_1^1 (kPa)	c_2^1	c_1^2 (kPa)	c_2^2	$c_1^{3,4}$ (kPa)	$c_2^{3,4}$	α_0	RMS
1	18.58	1.12	0.92	12.65	2.35E-02	0.01	3.15	51.67	6.87
2	16.31	1.38	1.30	18.33	1.10E-01	0.16	2.71	49.39	2.52
3	6.94	0.92	1.35	10.51	3.97E-03	0.01	3.00	50.33	4.48
4	15.90	0.44	0.83	7.79	1.87E-01	0.21	1.10	45.54	9.54
5	17.19	0.21	0.68	7.10	6.15E-02	0.07	1.74	53.07	3.86
6	17.92	1.19	0.48	6.42	3.04E-01	0.01	3.21	57.97	9.37
Mean	15.47	0.88	0.93	10.47	1.15E-01	0.08	2.49	51.33	6.11
Std dev	4.30	0.46	0.34	4.51	1.13E-01	0.09	0.87	4.14	2.95

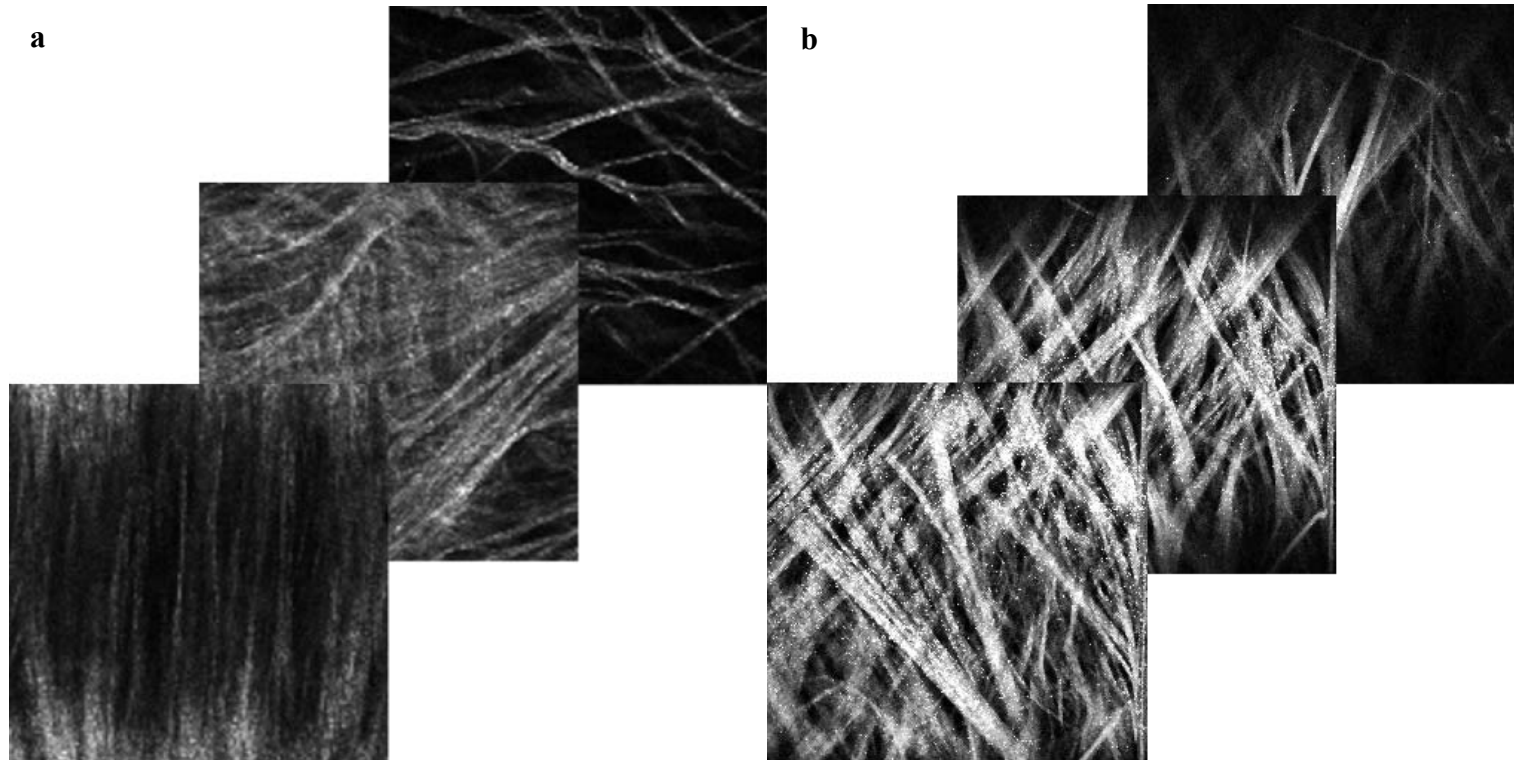


Fig. 3.6 NLOM image slices (150 x 150 μm) of an illustrative basilar (a) and carotid (b) artery. Basilar images (a) show collagen fiber alignment in the media, a transition area between media and adventitia, and the adventitia. Carotid images (b) show collagen fiber alignment in the inner and outer adventitia.

This figure shows three representative images for each vessel. For the basilar, the first (closest) slice corresponds to the media, the second to a transition from media to adventitia, and the third to the adventitia. It is seen that the media of the basilar artery consists primarily of thin, predominately circumferentially oriented collagen fibers. When comparing results for basilar and carotids, this finding appears to correspond well with the estimated values of the parameters associated with the circumferential collagen fibers for the basilar artery ($c_1^2 < c_2^2$), as seen in Table 3.2. Indeed, this estimation further reflects the significant axial and diagonal orientations in the adventitia (Table 3.2). In contrast, NLOM slices from the carotid artery show thicker and more diagonally oriented collagen from the outer media to the adventitia (because of the greater wall thickness plus loss of signal, images could not be collected throughout the entire wall). This broad distribution of fiber angles also appears to be reflected by the estimated parameter values (Table 3.3) wherein all fiber families have similar values. The slightly higher values associated with the circumferential direction may have been due to circumferentially oriented collagen in the media or passive smooth muscle, neither of which were captured by the NLOM imaging.

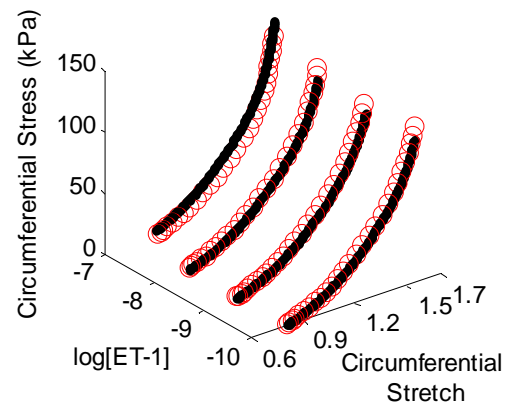
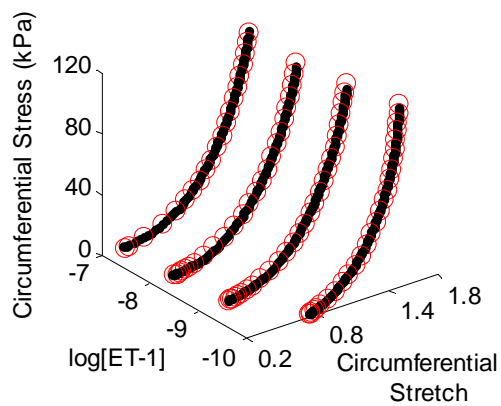
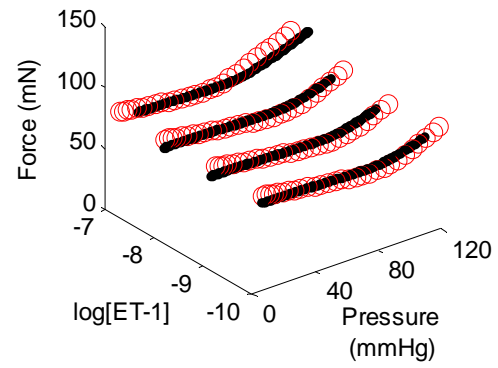
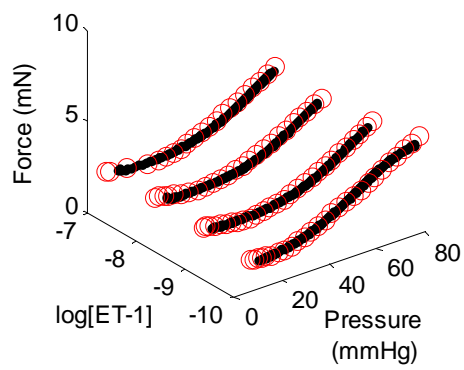
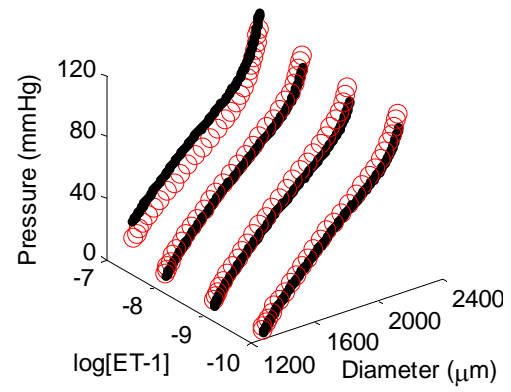
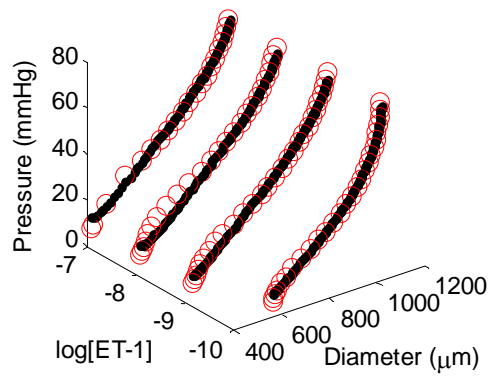


Fig. 3.7 Representative active basilar artery data (—) and active model fits (‘o’).

Fig. 3.8 Representative active carotid artery data (—) and active model fits (‘o’).

After first fixing the known values of the parameters for the passive portion of the overall behavior (Tables 3.2 and 3.3), simultaneous nonlinear regression of biaxial data for the four concentrations of ET-1 revealed that the proposed active constitutive relations (Eqs. 3.12 to 3.17) fit the active data well (Figs. 3.7 and 3.8). Associated best-fit values of the 9 material parameters (T_M , λ_M , b , d , c , p , q , r , s) are listed in Tables 3.4 and 3.5. Albeit not shown, based on AIC values, this model was found to be the best of many different models considered for both the basilar and carotid arteries despite values of λ_M (Tables 3.3 and 3.5) being higher than values inferred directly from data (Figs. 3.2 and 3.3; Table 3.1).

Finally, the combined passive – active constitutive relations were found to fit biaxial data under basal conditions well for both the basilar and carotid arteries (not shown). In particular, specimen-specific parameters for both passive and active behaviors were fixed based on the aforementioned fits to data (Tables 3.2, 3.3, 3.4, and 3.5) and an ‘equivalent [ET-1] concentration’ was allowed to be a free parameter. Mean best-fit values were 3.59E-11 M and 3.56E-07 M for the basilar and carotid arteries, respectively (Table 3.1). Hence, the equivalent [ET-1] concentrations for the basilar artery were slightly smaller than the lowest value tested (10^{-10} M) and were grouped closely. These values are consistent with the pressure-diameter tests wherein the data for basal tone fell between those for passive and [ET-1] = 10^{-10} M behaviors (Fig. 3.2). Conversely, mean values for the equivalent [ET-1] concentration for the carotids was much higher and had a larger standard deviation. This finding suggests that basal tone varied considerably from specimen-to-specimen for the carotid arteries, ranging from

Table 3.4 Best-fit parameters for active basilar data active model fits. Mean and standard deviation of each parameter are listed below.

Specimen	T_M	λ_M	b	d	c	q	p	r	s	RMS
1	52.23	1.34	7.96	9.39	10.25	30.43	12.52	20.32	10.34	18.30
2	79.95	1.47	6.90	17.42	9.04	17.04	9.68	33.43	9.99	6.19
3	47.08	1.41	6.71	9.59	10.08	16.37	10.57	70.00	10.80	6.54
4	54.87	1.66	5.69	2.94	10.05	23.81	31.65	58.71	10.04	3.57
5	127.33	2.31	6.09	1.59	10.21	12.85	7.55	77.61	10.01	3.47
6	220.43	2.27	7.94	0.43	8.37	21.11	29.06	143.97	9.81	9.12
7	79.27	1.63	5.53	1.21	10.42	21.73	27.95	65.04	9.99	4.03
Mean	94.45	1.73	6.69	6.08	9.77	20.48	18.43	67.01	10.14	7.32
Std dev	61.89	0.40	1.00	6.29	0.76	5.76	10.57	39.63	0.33	5.25

Table 3.5 Best-fit parameters for active carotid data active model fits. Mean and standard deviation of each parameter are listed below.

Specimen	T_M	λ_M	b	d	c	q	p	r	s	RMS
1	51.89	1.50	9.86	19.88	10.68	10.69	9.74	21.70	10.10	9.55
2	49.52	1.72	9.10	16.40	10.51	10.08	9.70	121.06	10.07	9.63
3	53.92	1.72	9.46	13.87	11.21	20.22	24.18	484.91	10.04	8.25
4	50.80	1.70	5.66	17.69	10.35	4.80	10.65	43.29	10.12	10.61
5	50.64	1.56	7.87	14.40	10.52	9.76	10.18	48.80	10.14	11.34
Mean	51.35	1.64	8.39	16.45	10.66	11.11	12.89	143.95	10.09	9.88
Std dev	1.66	0.11	1.70	2.46	0.33	5.61	6.32	194.23	0.04	1.17

greater than $[ET-1] = 10^{-7}$ M to less than $[ET-1] = 10^{-10}$ M. Despite these variations, the equivalent $[ET-1]$ concentrations accurately reflected the level of smooth muscle cell activation in each specimen under basal conditions (not shown).

DISCUSSION

Amongst other risk factors, hypertension and aging are increasingly recognized as potent initiators and indicators of cardiovascular risk [62-64]. Moreover, effects of both hypertension and aging on wall stiffness have emerged as potentially critical clinical information [65-67]. Despite reports many years ago that elastic and muscular arteries respond very differently to both hypertension and aging [68, 69], there have been few attempts to quantify and compare such changes in arteries from the same animals using methods of continuum biomechanics. Fundamental to understanding arterial mechanics, of course, is knowledge of the basic geometry, microstructure, and biaxial biomechanical behavior of the normal, healthy arterial wall.

Basic morphological and microstructural differences between the basilar and carotid arteries revealed herein by standard histology (Fig. 3.1) were consistent with many prior reports on cerebral arteries and common carotid arteries. Hematoxylin and Eosin (H&E) stains cell nuclei blue to purple and other tissues, including collagen, pink. Verhoeff Van Gieson (VVG) stains elastin dark blue to black. The VVG staining revealed that the basilar artery had a prominent internal elastic lamina, but little medial elastin and no external elastic lamina. Conversely, the common carotid artery had a prominent internal elastic lamina plus many concentric elastic laminae within the media. The media of the basilar artery consisted primarily of smooth muscle. Also as expected,

the media occupied about half of the wall in the basilar artery but over two-thirds of the wall in the carotid. Smooth muscle cells appeared to be oriented primarily circumferentially in both types of vessel. Of course, the internal radius and wall thickness were both much smaller for the basilar than the carotid artery.

The dramatically lower amount of elastin in basilar compared to carotid arteries was reflected well by the best-fit values of the parameter c in the four fiber family model (Tables 3.2 and 3.3). A comparable finding of decreasing values of c was reported recently for aging of human arteries [70]. Similarly, best-fit parameters for the different families of collagen appeared to track general observations from the NLOM. Together, these findings give added confidence that the four family constitutive relation is a reasonable descriptor of the passive behavior of both types of arteries, which will facilitate further vessel to vessel comparisons. Indeed, this model is also consistent with recent models of arterial growth and remodeling [71], which further increases the general utility of this model.

Hu et al. [33] previously used the same four fiber model (albeit based on a different objective function and by setting axial and circumferential parameters equal) to fit biaxial data from porcine basilar arteries tested under nearly passive conditions. The pig and rabbit basilar arteries have similar histological features and they are surprisingly similar in unloaded caliber ($R_o = 256 \mu\text{m}$ for the pig) and in vivo axial stretch (1.17 for the pig). Comparing our results for parameter c (Table 3.2) to those of Hu and colleagues, we found c to be similarly very small in both. Values of the dimensioned parameters for the axially and circumferentially oriented collagen (c_1^1 and c_1^2) were an

order of magnitude or more lower for the rabbit than for the pig, and the non-dimensional parameters (c_2^1 and c_2^2) were also lower. The parameters associated with the diagonal fibers were opposite in character ($c_1^{3,4} > c_2^{3,4}$ for the rabbit) compared to those for the pig, and the best-fit angle α_o was nearly 30 degrees higher for rabbit than for the pig. Without more detailed information, it is difficult to say whether these differences are due to different restrictions placed on the constitutive relation, using a different objective function, using different testing solutions, or simply real differences between species. In this regard, it is interesting that overall best-fit values of the parameters for the rabbit basilar arteries tested under basal conditions (5.52×10^{-5} kPa, 30.88 kPa, 2.87, 20.12 kPa, 2.22, 5.17 kPa, 10.72, and 37.74° for c , c_1^1 , c_2^1 , c_1^2 , c_2^2 , $c_1^{3,4}$, $c_2^{3,4}$, α_o , respectively) were closer to those for the pig. Wicker et al. [58] used the same approach to modeling as Hu and colleagues, but for rabbit basilar arteries. The present best-fit values of the material parameters (Table 3.2) were all much more similar to those reported by Wicker and colleagues, but the best-fit diagonal fiber family angle was 10 degrees higher than that reported previously. The otherwise modest differences in parameters are likely due to the prior setting of axial and circumferential parameters equal as well as the use different testing solutions and objective function. Taken together, therefore, it appears that there may be important mechanical differences between rabbit and pig basilar arteries. Finally, Monson et al. [27] reported biaxial data for human cerebral arteries and associated fits using a classical Fung-exponential model. We did not evaluate the potential utility of the Fung model because Hu et al. [33]

previously showed that the Fung model was inferior for fitting biaxial data for basilar arteries. Moreover, the purely phenomenological Fung model cannot provide any guidance in current growth and remodeling simulations, which are based on microstructurally motivated models.

Common carotid arteries are among the most commonly tested blood vessels for they are long, straight, and cylindrical without branches. Nevertheless, few have reported complete biaxial data and none have considered biaxial active behavior. Eberth et al. [59] biaxially tested mouse common carotid arteries and subsequently fit the basal data using the four fiber family model. They found an average in vivo axial stretch for wild type mice to be 1.71, which is close to the 1.68 found herein for the rabbit; although Jackson et al. [72] did not perform biaxial mechanical tests, they similarly reported a value of 1.62 for the rabbit. Comparing best-fit values of parameters found by Eberth and colleagues for wild type mice to results herein for the carotids under passive conditions revealed that most of the parameters were similar. The main differences again was the higher value of the diagonal fiber angle for the rabbit. These slight differences most likely reflect differences between the rabbit and mouse, but the objective function also differed.

In addition to passive behaviors, vasoactivity is critical in arterial homeostasis and in adaptations to altered mechanical loading or physiologic conditions [71, 73]. Dose response behaviors of cerebral arteries to ET-1 have been reported previously, but only for ring tests [22, 74] or standard pressure-diameter tests [75, 76]. Both of these types of studies ignore effects of smooth muscle contraction on axial behavior.

Moreover, ring tests simultaneously expose both the adventitia and the intima to ET-1, thus triggering constrictor and dilator responses via ET_A and ET_B receptors. Despite these limitations these studies reveal a similar sigmoidal relationship for vessel contraction as a function of ET-1 concentration. Whereas these studies quantified contraction as a percent of control diameter [22] or a percent of KCl induced contraction [74], none attempted to model the relationship. In contrast, we report some of the first active biaxial data and the first constitutive relation for quantifying this behavior. As revealed by the measures of goodness of fit and the direct comparisons of data and fits (Fig. 3.7), this relation appears to be a good first phenomenological model. There are no comparable data or constitutive relations to which to compare.

There exists much more data beyond that collected via simple ring tests [77] for the active response of common carotid arteries [78-80]. For example, Dobrin et al. [79] reported some of the first active common carotid artery data using the vasoconstrictor norepinephrine and canine vessels. They also noted a sigmoidal relationship between smooth muscle activation and agonist concentration as well as a parabolic active stress – strain relation. No modeling was attempted, but maximum incremental elastic moduli and associated strains were used to compare active response from vessel to vessel. The average associated strain can be converted to stretch and the resulting value, 1.46, can be compared to λ_M determined herein (1.49 and 1.64 in Tables 3.2 and 3.5, respectively). These values suggest that smooth muscle responds similarly in different species. Indeed, Cox [78] published a seminal paper comparing active mechanics of carotid arteries in rats, rabbits, and dogs. His plot of circumferential stress versus normalized diameter

further supports the comparable responses of smooth muscle across species; maximum circumferential stress for dogs and rabbits occurred at normalized diameters of 1.7 and 1.9, respectively. Although the vessels may have been damaged in his study due to the supra-physiologic pressures (~ 250 mmHg), the general trends agree with our findings. Although not studied in detail, Cox et al. [81] noted that activation does affect axial responses.

Masson et al. [80] used a fully 3D four fiber family model that accounted for residual stresses and circumferential active stresses to study human in vivo carotid data; the active model was similar to that proposed by Achakri et al. [60] model. Comparing results for the passive parameters c and α_o revealed values similar to those for the rabbit, yet all other passive parameters differed markedly. In contrast, best-fit values of T_M and λ_M in [80] are comparable to those reported herein. Both λ_M and T_M values are very similar to those found for our model (Table 3.5), which is interesting given differences in the models and species.

As noted above, many prior investigators have studied the biomechanical properties of common carotid and cerebral arteries, yet few attempted to quantify differences between them. Many years ago, however, Hayashi and his colleagues [13, 82] compared passive and active behaviors of human intracranial (basilar) and extracranial (common carotid) arteries as a function of aging. A single stiffness parameter (or, elastic modulus) was used to facilitate comparisons. They concluded that intracranial arteries were stiffer than extracranial arteries though they had a higher elastic modulus. Our results agree qualitatively with this conclusion. Toda et al. [83] cut

helical strips from dog intra- and extra-cranial arteries and exposed them to vasoactive agents. Due to differences in experiment set up it is difficult to compare our results to theirs. They did note a relationship between length (i.e., smooth muscle length) and active tension similar to what we found and modeled with Eq. 3.13. Direct comparison of active responses as a function of the type of vessel was not possible due to the use of different vasoactive agents.

In summary, our collective understanding of the biomechanical behaviors of diverse arteries continues to grow. Nevertheless, most prior reports have focused on a single type of artery from a single species and have often ignored biaxial behaviors, particularly active. Moreover, because of differences in testing procedures and methods of data analysis, it is difficult to infer from multiple studies possible differences in biomechanical behaviors amongst different classes of vessels. We showed that a four fiber family constitutive relation for passive behaviors reflects differences in microstructure between two vessels in the same species. Our active model similarly describes responses in two different types of vessels and predicts different levels of smooth muscle activation via an ET-1 equivalent parameter. There is, nevertheless, a need to extend the current model to account for the transmural distributions of constituents.

CHAPTER IV

PROLONGED EX VIVO CULTURE OF THE RABBIT BASILAR ARTERY AND ITS EFFECTS ON BIAXIAL MECHANICAL BEHAVIOR

INTRODUCTION

Many cardiovascular diseases result from maladaptive growth and remodeling, but such effects are often ignored in the cerebrovasculature. In order to understand better the etiology of these diseases it is necessary to follow their natural history. Whereas it is convenient to follow disease progression using in vivo animal models [31, 84-87], it can be difficult to tease out the underlying mechanisms because of the complex physiology and pathophysiology. That is, it is difficult to control or measure all potential effects in vivo. In vivo studies can also require a large number of animals when tissue must be excised upon euthanasia at the many time points of interest. There is, therefore, a need to explore ex vivo organ culture wherein the mechanical and chemical environment can be controlled precisely and the mechanical testing can be performed throughout the culture period on the same specimen, thus allowing clearer interpretations of results and using fewer animals.

In this chapter, we describe the first attempt at ex vivo culture of large cerebral arteries under biaxial loading conditions for extended periods (up to 5 days). Control cultures were performed first, wherein it was demonstrated that native passive properties of the vessel could be maintained over the period of interest. Next, vessel remodeling was attempted (motivated by the desire to understand cerebral vasospasm) by exposing

the cultured arteries to clotted whole blood as well as individually to various vasoactive molecules and growth factors that are thought to be released by a blood clot in vasospasm: endothelin-1 (ET-1), platelet-derived growth factor-AB (PDGF-AB), transforming growth factor- β 1 (TGF- β 1). Biaxial biomechanical behaviors were quantified using constitutive models developed by Wagner and Humphrey [88]. These models account for both passive and active responses, the latter at different levels of smooth muscle cell activation.

METHODS

All animal protocols were approved by the IACUC of Texas A&M University. Following euthanasia with sodium pentobarbital, basilar arteries were excised from specific pathogen free male New Zealand white rabbits, gently cleaned, and cannulated using custom pipettes. The vessels were then mounted in our custom organ culture device [41] as described in Wicker et al. [58]. Vessels were tested and cultured in MegaCell DMEM (Sigma), supplemented with 580 mg/L L-glutamine, 200 U/L penicillin, 100 mg/L streptomycin, 50 mg/L glycine, 3 μ g/L CuSO_4 , and 50mg/L ascorbic acid. Control culture media also contained 1% fetal bovine serum whereas media used to test effects of vasoactive molecules and growth factors contained 5% autologous rabbit plasma. The plasma was found to increase overall culture success (data not shown). The following concentrations and combinations of vasoactive molecules and growth factors: 10^{-8} M ET-1, 20 ng/ml PDGF-AB, 10^{-8} M ET-1 and 20 ng/ml PDGF-AB, and 30 ng/ml TGF- β 1. During mechanical testing, a LabView Program continuously recorded measurements of axial length, outer diameter, axial force, and

pressure using micrometers, video calipers, and pressure and force transducers, respectively. After cannulation, the nearly unloaded length of the vessel was determined at ~ 7 mmHg transmural pressure. As described in Wagner and Humphrey [88], the vessel then underwent a one hour of acclimation followed by preconditioning before the unloaded length was re-verified. Inner and outer radii were recorded at axial stretches of 1.1, 1.15, 1.2 and pressures of 7, 40 and 80 mmHg to facilitate inference, by invoking incompressibility, of wall thickness throughout testing based on the on-line measurement of other diameter and axial stretch. The in situ loaded conditions were assumed to be an axial stretch of 1.15 [58] and a transmural pressure of 80 mmHg.

On days 0, 1, 3, and 5 of culture, the vessel underwent mechanical testing that included 4 pressure-diameter cycles from 7 mmHg to 80 mmHg while axial stretch was held constant at each of three values: 1.1, 1.15, and 1.2. Day 0 denotes the day of harvest. After mechanical testing, the vessels were returned to the in vivo length at a pressure of 7 mmHg and outer diameter was recorded. Contractility was then tested via an adventitial exposure to 60 mM potassium chloride (KCl), with outer diameter measured during the contraction. KCl was used due to its transient effect [20], and ease of washing out. In particular, the adventitial bath was then rinsed three times with normal saline (9 g NaCl/L) and replaced with fresh culture media.

During culture, the sealed testing chamber was disconnected from the bench top testing device and placed in an incubator. Luminal pressure, flow, and pulsatility were control by a pressure controller and two peristaltic pumps. Culture conditions were as follows: pressure of $80 \text{ mmHg} \pm 10 \text{ mmHg}$, flow rate of 6 ml/min, which gave an

approximate in vivo shear stress of 2 Pa, and pulse rate of 200 beats/min, all similar to in vivo conditions for a rabbit at rest [89]. Adventitial media was changed on days 1 and 3 for culture controls. Due to possible consumption/degradation rates of the adventitially applied vasoactive molecules and growth factors, the adventitial media (base media plus the applied molecule) was changed daily. For all cultures, luminal media was changed on day 3 alone. After the final day of culture, the vessel was removed from the system and incubated in culture media with 0.45 mg/ml Thiazoyl Blue Tetrazolium (MTT) for 1 hour to determine overall cell viability. Vessels that did not stain with MTT were not used in the analysis.

As in Wagner and Humphrey [88], inner, r_i and outer, r_o , radii were recorded at six states, which were then used to calculate wall volume via

$$V = \pi(r_o^2 - r_i^2)l, \quad (4.1)$$

where l is the current axial length. The resulting values were averaged to compute a mean volume, \bar{V} . Inner radius, which could not be recorded on-line during mechanical testing, was then calculated using incompressibility to yield

$$r_i = \sqrt{r_o^2 - \frac{\bar{V}}{\pi l}}. \quad (4.2)$$

Using calculated inner radii and recorded data, mean circumferential and axial Cauchy stress and stretch were calculated using equations,

$$t_{\theta\theta} = \frac{Pr_i}{h}, \quad t_{zz} = \frac{f}{\pi(r_o^2 - r_i^2)}, \quad \lambda_\theta = \frac{(r_i + r_o)/2}{(R_i + R_o)/2}, \quad \text{and} \quad \lambda_z = \frac{l}{L}, \quad (4.3, 4.4, 4.5, 4.6)$$

where P is the transmural pressure, h is the current wall thickness, f is the total axial force, R_i and R_o are the inner and outer reference radii respectively, and L is the reference axial length.

A four-fiber family strain energy function of the following form was used to model the passive data [30, 58],

$$W = \frac{c}{2}(I_1 - 3) + \sum_{k=1,2,3,4} \frac{c_1^k}{4c_2^k} \left\{ \exp \left[c_2^k \left((\lambda^k)^2 - 1 \right)^2 \right] - 1 \right\}, \quad (4.7)$$

where I_1 is the first invariant of the right Cauchy-Green tensor, c is a material parameter which models the elastin-dominated contribution of the matrix (assumed to be isotropic) and c_1^k (kPa) and c_2^k are material parameters associated with the k^{th} fiber family. Fiber family $k = 1$ denotes axially oriented (0°) collagen fibers; $k = 2$ denotes circumferentially oriented (90°) collagen fibers and passive smooth muscle cells, and $k = 3$ and $k = 4$ denotes diagonally oriented collagen fibers. Material parameters for the diagonal fibers are equal, meaning $c_1^3 = c_1^4$ and $c_2^3 = c_2^4$ [48]. Stretches of the k^{th} fiber family are

$$\lambda^k = \sqrt{\lambda_\theta^2 \sin^2 \alpha_0^k + \lambda_z^2 \cos^2 \alpha_0^k}, \quad (4.8)$$

where α_0^k is the angle of the k^{th} fiber relative to the axial direction in a reference configuration. Mean circumferential and axial Cauchy stresses are then given constitutively by

$$\sigma_\theta^{\text{Passive}} = c \lambda_\theta^2 \left(1 - \frac{1}{\lambda_\theta^4 \lambda_z^2} \right) + \lambda_\theta^2 \sum_{k=1,2,3,4} \left\{ c_1^k \left((\lambda^k)^2 - 1 \right) \exp \left[c_2^k \left((\lambda^k)^2 - 1 \right)^2 \right] \sin^2 \alpha_0^k \right\}, \quad (4.9)$$

and

$$\sigma_z^{Passive} = c\lambda_z^2 \left(1 - \frac{1}{\lambda_z^4 \lambda_\theta^2}\right) + \lambda_z^2 \sum_{k=1,2,3,4} \left\{ c_1^k \left((\lambda^k)^2 - 1 \right) \exp \left[c_2^k \left((\lambda^k)^2 - 1 \right)^2 \right] \cos^2 \alpha_0^k \right\}. \quad (4.10)$$

Throughout culture, vessels were found to have different levels of basal tone or smooth muscle cell activation. To account for this finding, we used an active model developed by Wagner and Humphrey [88], which includes terms in both the circumferential $\sigma_\theta^{total} = \sigma_\theta^{active} + \sigma_\theta^{passive}$ and axial $\sigma_z^{total} = \sigma_z^{active} + \sigma_z^{passive}$ directions. Active circumferential stress is modeled by the following equation,

$$\sigma_\theta^{active} = T_M e^{-b \left(\frac{\lambda_M - \lambda_\theta}{\lambda_M} \right)} \frac{1}{1 + e^{-d(\log([ET-1]) + c)}}, \quad (4.11)$$

where T_M (kPa) is the maximum stress generated by the SMCs, λ_M is the circumferential stretch at which SMCs achieve maximum stress, and b , c and d are dimensionless parameters. This function takes into account mechanical as well as chemical effects on the SMCs. Active axial stress is similarly model as,

$$\sigma_z^{active} = (-q\lambda_\theta + p) \frac{1}{1 + e^{-r(\log([ET-1]) + s)}}, \quad (4.12)$$

where r and s are dimensionless material parameters associated with the axial dose response to vasoconstrictors, modeled in terms of equivalent concentrations of ET-1.

Each day of culture had its own equivalent [ET-1] concentration to account for varying degrees of SMC tone due to different levels of vasoconstrictors and smooth muscle function. Although the active model could thus include 12 free parameters to be determined via nonlinear regression, the parameters c and s were fixed at a value of 10

based on previous results [88]. In total 10 parameters ($[ET-1]_0$, $[ET-1]_1$, $[ET-1]_3$, T_M , λ_M , b , d , p , q , r) in the active model were used to fit the culture data.

The final day of culture was found to show the least SMC function and was used as the ‘passive response’. Best-fit values of material parameters for this ‘passive response’ were determined via nonlinear regression (Matlab function lsqnonlin) by minimizing the following objective function,

$$e = \sum_{i=1}^N \left[\left(\frac{P_i^{Theory} - P_i^{Exp}}{P_{Average}^{Exp}} \right)^2 + \left(\frac{f_i^{Theory} - f_i^{Exp}}{f_{Average}^{Exp}} \right)^2 \right], \quad (4.13)$$

where N is the number of data points, ‘Exp’ denotes experimental data, ‘Theory’ denotes calculated variables, and ‘Average’ denotes an average of all specified data. Parameters were constrained to respect a lower bound of 0, but only α_o had an upper bound ($\pi/2$). Using the passive parameters, data for the preceding days of culture were then fit simultaneously to determine the remaining best-fit values. Nonlinear regression (Matlab function lsqnonlin) was again used to minimize the objective function, Eq. 4.13, to determine the active parameters. Like the passive material parameters, all active parameters were constrained to respect a lower bound of 0 with no upper bound. ‘Goodness of fit’ in both the passive and active models was determined via the root mean sum of the square (RMS),

$$RMS = \sqrt{\sum_{i=1}^N \frac{(\sigma_{\theta i}^{exp} - \sigma_{\theta i}^{th})^2}{N}} + \sqrt{\sum_{i=1}^N \frac{(\sigma_{zi}^{exp} - \sigma_{zi}^{th})^2}{N}}, \quad (4.14)$$

where N is again the number of parameters. For both passive and active fits, outlier detection was performed on parameter values in the same manner as Wagner and Humphrey [88].

Outer diameter was recorded during viability testing both before and after exposure to 60 mM KCl. A measure of the contractility of smooth muscle cells at that point in the culture was then calculated as

$$\frac{d^{PostKCl}}{d_{Max}^{PreKCl}} \quad (4.15)$$

where $d^{PostKCl}$ is the outer diameter recorded after KCl exposure on a specific day of culture and d_{Max}^{PreKCl} is the maximum recorded outer diameter before KCl exposure over all days of culture (typically the last day).

MTT staining, used as a viability test, was more qualitative than quantitative. Cultured vessels were visually compared with fresh samples and notes taken on the level of staining (faint vs. bright) and whether it was consistent throughout the tested vessel. While all culture vessels stained more lightly than did the fresh controls. Vessels that stained only faintly or had areas that did not stain at all were excluded from this study.

Table 4.1 Values of constriction to 60 mM KCl on days 0, 1, 3 and 5 and calculated λ_M for culture controls.

	Percent Constriction				λ_M
	Day 0	Day 1	Day 3	Day 5	
Mean	0.34	0.26	0.24	0.08	1.30
Std Dev	0.07	0.09	0.12	0.09	0.15

RESULTS

Pressure-diameter and circumferential stress-stretch curves of control culture data (Fig. 4.1) are shifted left and have flexion points on Day 1 and Day 3. This suggests greater SMC tone/function on these days. Average constriction data from the KCl viability test (Table 4.1) confirms this trend for all control culture data. Day 5, the final day of culture, can be seen to have the least SMC function as it is the farthest curve to the right (Fig. 4.1). Percent constriction data (Table 4.1) supports Day 5 having the least SMC function or being the most passive. Model fits of the Day 5 ‘passive response’, seen in Fig. 4.2, show that while the response may not have been fully passive, the four fiber family model fit the data well. Associated parameter values are listed in Table 4.2. Fits to data from Day 0, 1 and 3 (Fig. 4.3) show the active model can fit multiple sets of data representing differing levels of smooth muscle tone. Associated parameter values are listed in Table 4.3. The equivalent ET-1 values accurately reflected the changing levels of smooth muscle cell activation. This model has been shown [88] to predict reasonable values of λ_M , the stretch at which active stress is highest. This held true here for our fits for the calculated λ_M values (Table 4.1) were similar to those predicted by the model (Table 4.3).

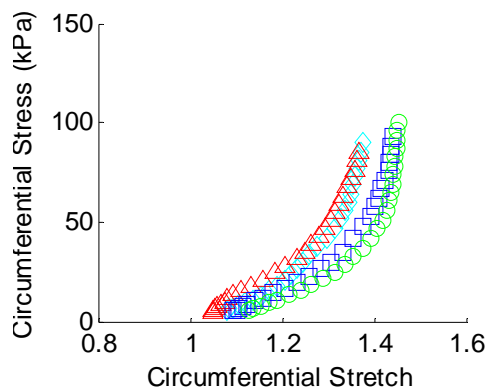
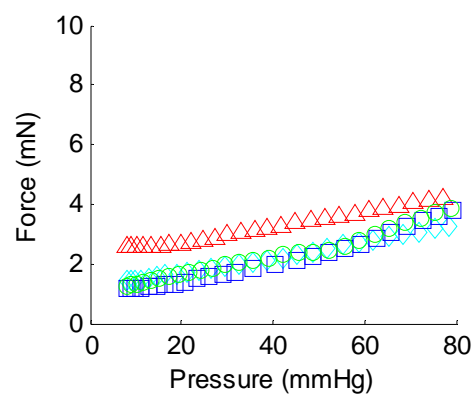
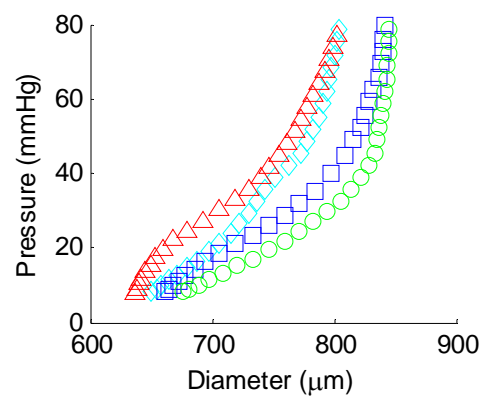


Fig. 4.1 Representative control culture data from days 0 (\diamond), 1 (Δ), 3 (\square), and 5 (\circ).

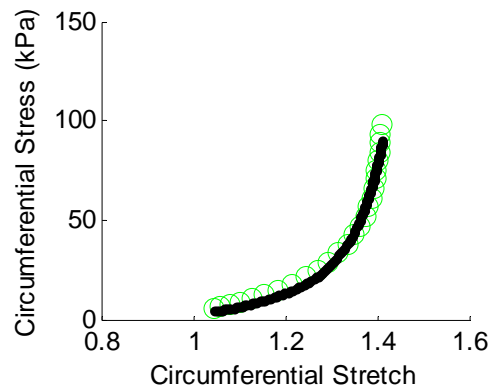
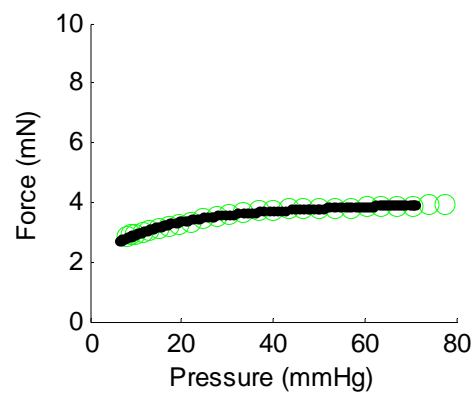
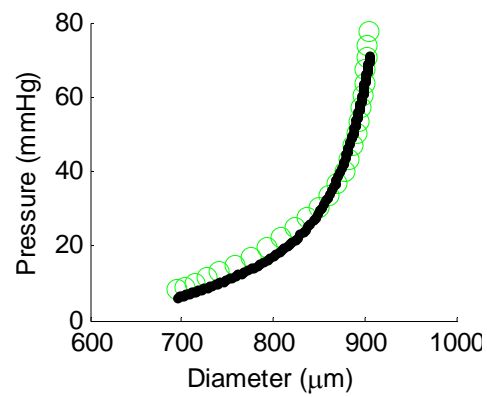


Fig. 4.2 Representative control culture day 5 'passive' data (\circ) and fits ($-$).

Table 4.2 Best-fit parameters for control culture day 5 data ‘passive’ fits.

Specimen	c	c_1^1 (kPa)	c_2^1	c_1^2 (kPa)	c_2^2	$c_1^{3,4}$ (kPa)	$c_2^{3,4}$	α_0	RMS
1	8.16E-10	5.96E-03	85.38	2.76E-03	21.97	14.00	0.66	89.24	2.83
2	4.30E-08	1.82E-09	7.75	3.60E-03	15.36	11.81	0.40	89.99	5.43
3	1.91E-08	39.38	2.74	2.79E-08	30.25	20.23	0.31	78.55	3.94
4	4.22E-08	2.51	21.73	2.45E-08	7.40	6.99	0.55	58.03	3.49
5	6.03E-08	1.35E-01	55.23	1.43E-07	25.15	18.10	0.62	58.60	3.70
6	3.59E-06	13.07	4.11	9.61E-10	18.98	10.77	1.40	54.54	4.37
7	7.11E-08	12.22	9.31	2.14E+00	2.50	22.99	0.03	51.14	3.11
8	1.20E-06	5.82E-03	77.09	7.52E-01	24.68	47.82	1.49	45.31	4.64
9	8.93E-08	33.32	8.09	6.44E-03	7.62	17.06	0.01	57.31	2.00
10	7.23E-06	1.07	35.90	3.63E+00	2.28	17.18	0.01	46.53	4.38
Mean	1.23E-06	10.17	30.73	6.53E-01	15.62	18.70	0.55	62.92	3.79
Std Dev	2.39E-06	14.73	31.33	1.25E+00	10.11	11.27	0.53	16.77	0.99

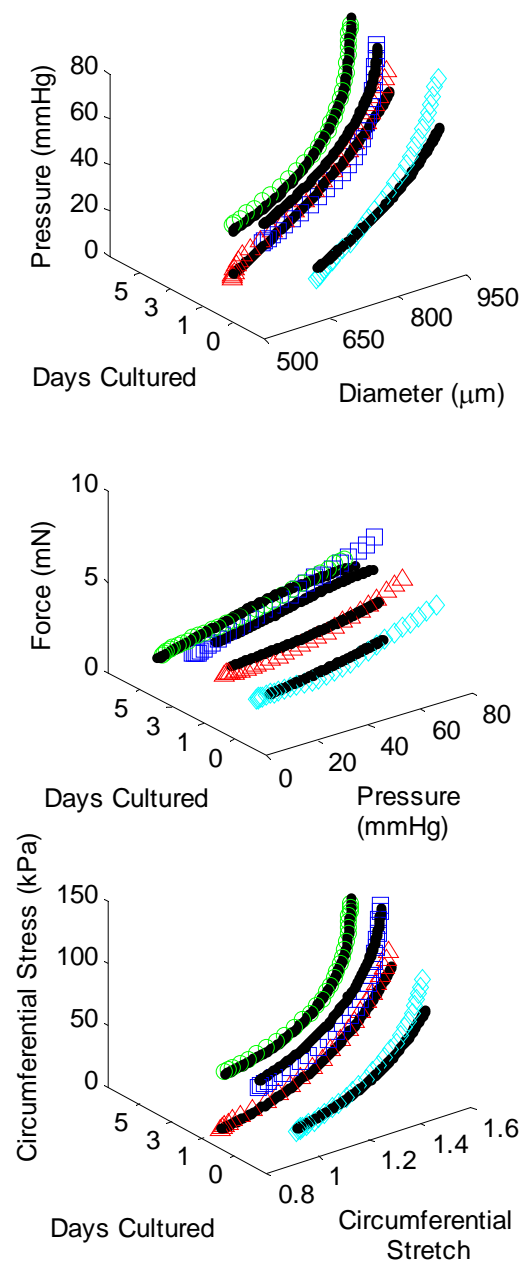


Fig. 4.3 Representative control culture days 0, 1, and 3 ‘active/basal tone’ data and fits.

Table 4.3 Best-fit parameters for control culture day 0, 1, and 3 data ‘active/basal tone’ fits.

Specimen	$[ET-1]_0$	$[ET-1]_1$	$[ET-1]_3$	T_M	λ_M	b	d	q	p	r	RMS
1	3.36E-12		6.56E-11	106.69	1.51	5.90	9.92	49.64	11.00	69.17	34.54
2	2.18E-11		6.93E-11	107.42	1.37	35.51	0.91	32.52	22.64	53.92	26.20
3	7.11E-11	7.43E-11	6.17E-11	92.15	1.68	3.81	11.67	49.92	26.81	59.81	24.49
4	5.14E-11	6.04E-11	2.10E-12	93.23	1.70	9.88	0.88	50.01	17.35	52.17	15.97
5	9.31E-11	9.32E-11	9.79E-11	111.22	1.62	14.24	8.94	63.70	20.52	366.53	17.63
Mean	4.82E-11	7.60E-11	5.93E-11	102.14	1.57	13.87	6.46	49.16	19.66	120.32	23.77
Std dev	3.24E-11	1.35E-11	3.13E-11	7.88	0.12	11.39	4.63	9.90	5.31	123.25	6.65

It was hoped that significant remodeling would occur in the cultures with high levels of vasoactive molecules or growth factors, but this was not the case. Fig. 4.4 shows data from a representative growth factor culture (PDGF-AB 20ng/ml). When compared to Fig. 4.1, we see similar trends of higher SMC tone on Day 1 and 3 and a ‘passive response’ on Day 5. Table 4.4, showing the percent constriction in response to KCl, further supports these trends. Fig. 4.5 shows a fit of the passive model to data from the last day of culture (Day 5 in this case). Associated parameter values can be found in Table 4.5 and have similar trends and values as the culture controls.

Table 4.4 Values of constriction to 60 mM KCl on days 0, 1, 3 and 5 and calculated λ_M for growth factor cultures.

	Percent Constriction				λ_M
	Day 0	Day 1	Day 3	Day 5	
Mean	0.25	0.10	0.10	0.09	1.22
Std Dev	0.10	0.09	0.11	0.12	0.12

A representative fit of the active data for a growth factor culture can be seen in Fig. 4.6. Associated parameters are in Table 4.6; like the passive parameters, they are indistinguishable from the control culture parameters. As with the control cultures, the active model predicted accurate λ_M values for growth factor cultures (Tables 4.4 and 4.6).

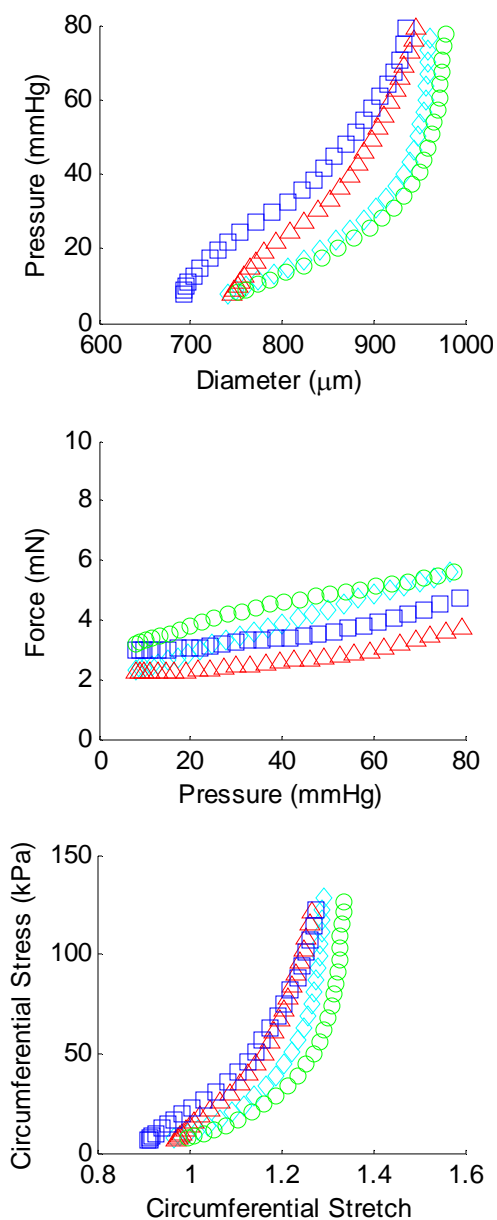


Fig. 4.4 Representative growth factor culture (20 ng/ml PDGF-AB) data from days 0 (' \diamond '), 1 (' Δ '), 3 (' \square '), and 5 (' \circ ').

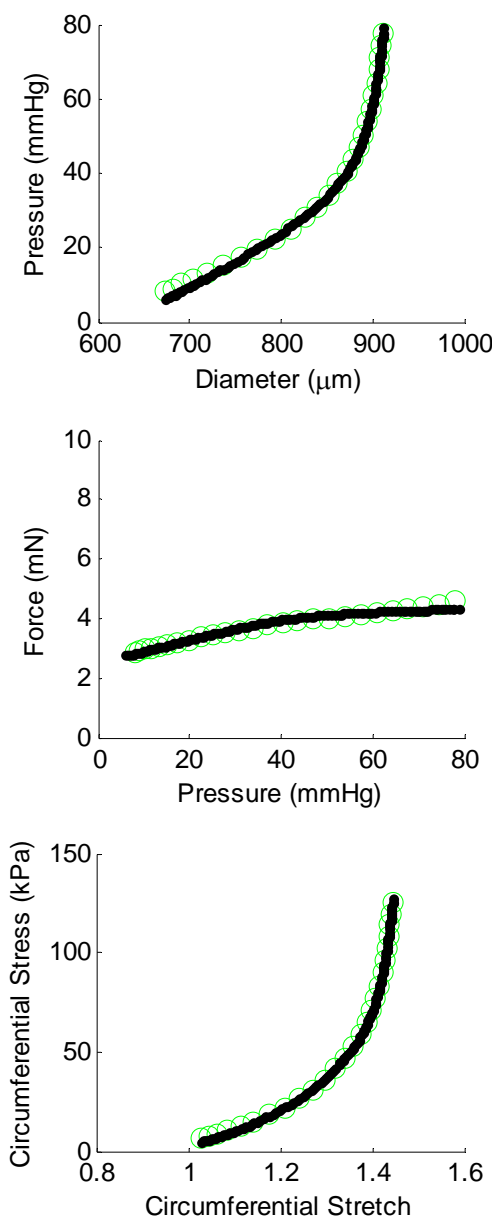


Fig. 4.5 Representative growth factor culture day 5 'passive' data (' \circ ') and fits ('-').

Table 4.5 Best-fit parameters for growth factor culture day 5 data ‘passive’ fits.

Specimen	c	c_1^1 (kPa)	c_2^1	c_1^2 (kPa)	c_2^2	$c_1^{3,4}$ (kPa)	$c_2^{3,4}$	α_0	RMS
1	1.07E-07	6.71	18.76	5.40E-03	14.14	37.82	0.57	54.26	2.54
2	7.35E-08	1.42	35.56	1.67E-02	12.73	36.72	0.48	56.26	2.97
3	2.58E-07	12.00	10.26	2.32E-02	6.18	19.45	0.20	62.80	2.19
4	1.00E-06	7.04	8.12	1.27E-03	36.49	20.44	5.22	56.52	6.61
5	3.63E-07	2.46	33.90	3.13E-03	14.86	34.20	0.77	51.81	2.86
6	1.40E-07	16.24	11.03	3.13E-03	20.71	33.90	3.48	47.13	7.08
7	1.81E-07	0.96	45.64	2.35E-02	14.28	30.69	0.08	63.01	2.63
8	1.53E-07	2.51	34.12	5.24E-04	43.52	45.08	0.63	56.62	3.67
9	4.21E-07	0.74	44.00	5.35E-03	17.44	33.19	0.03	56.89	3.92
10	1.05E-08	7.35	16.52	7.95E-06	21.11	23.92	0.76	55.70	2.05
Mean	2.71E-07	5.74	25.79	8.23E-03	20.15	31.54	1.22	56.10	3.65
Std Dev	2.87E-07	5.19	14.39	9.27E-03	11.40	8.12	1.72	4.67	1.79

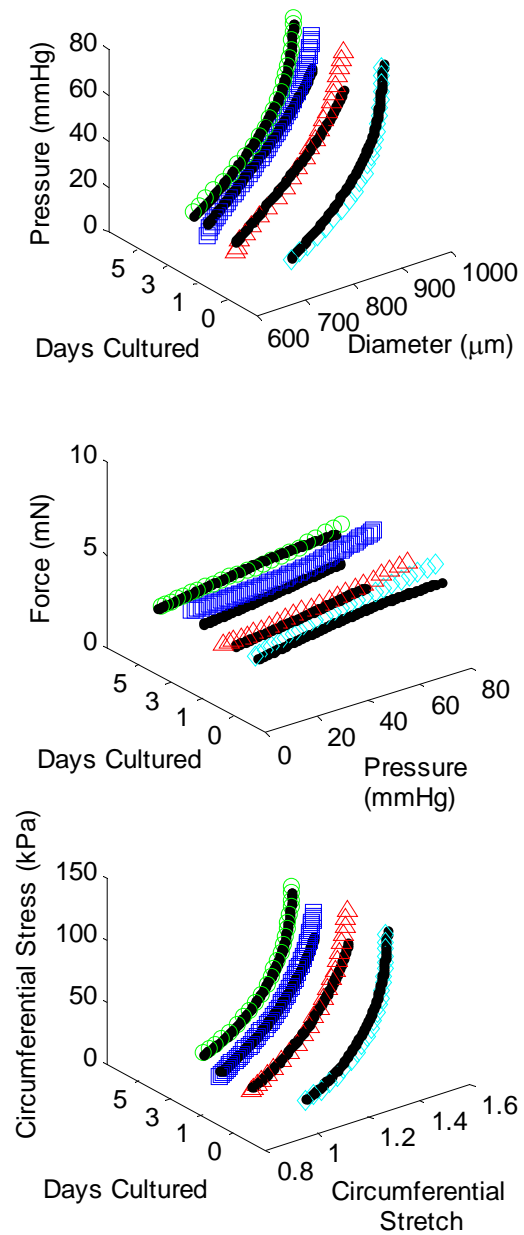


Fig. 4.6 Representative growth factor culture days 0, 1, and 3 ‘active/basal tone’ data and fits.

Table 4.6 Best-fit parameters for growth factor day 0, 1, and 3 data ‘active/basal tone’ fits.

Specimen	$[\text{ET-1}]_0$	$[\text{ET-1}]_1$	$[\text{ET-1}]_3$	T_M	λ_M	b	d	q	p	r	RMS
1	1.82E-11	7.85E-11	7.52E-11	79.99	1.40	12.34	7.35	29.20	15.94	56.73	13.02
2	8.52E-11	8.83E-11	9.31E-11	78.05	1.29	9.80	17.84	29.92	20.13	97.81	27.33
3	5.75E-11	5.55E-11	2.14E-12	71.55	1.36	12.15	1.82	27.34	18.58	36.10	22.05
4	3.31E-11	8.18E-11	7.52E-11	100.07	1.48	1.83	14.01	29.87	8.77	49.98	28.22
5	5.88E-15	9.20E-11	9.57E-11	110.32	1.63	21.74	0.43	45.65	0.02	80.94	20.93
6	8.08E-11	7.63E-11	3.35E-11	99.13	1.29	6.48	13.61	29.70	0.51	50.03	65.67
Mean	4.58E-11	7.87E-11	6.25E-11	89.85	1.41	10.72	9.18	31.95	10.66	61.93	29.54
Std dev	3.45E-11	1.28E-11	3.70E-11	15.37	0.13	6.69	7.10	6.78	8.95	22.92	18.52

DISCUSSION

A number of ex vivo studies have shown that arteries can be maintained in culture for short periods [41, 90]. Yet, all prior studies that have successfully maintained in vivo geometry used extracranial arteries. That is, of the few ex vivo studies of cerebral arteries, none maintained the in vivo geometry [91-93]. For example, Hoel et al. [92] cultured rings of canine basilar artery for 2 days and then measured contraction to various concentrations of 5-carboxamidotryptamine hydrochloride (5-CT) and 5-hydroxytryptamine hydrochloride (5-HT), both of which induce vasoconstriction in cerebral arteries [94]. They found that the cultured arteries had greater sensitivity and degree of contraction compared to fresh controls. This finding is contrary to what was found in the present study where constriction decreased after just one day of culture (Table 4.4); 5-CT and 5-HT work through different pathways than KCl, however, which we used to evaluate contractility herein. Yet, Yoshimoto et al. [93] cultured rings of canine basilar artery for 3 days and found no decrease in contraction to 80 mM KCl. Hansen-Schwartz et al. [91] cultured rings of rat basilar artery for 2 days and then tested contractility to various concentrations of ET-1. Culture increased the sensitivity to ET-1 and maximum contraction was maintained. Unlike these ex vivo ring cultures, we were not able to maintain contraction throughout the culture (Table 4.1).

Ex vivo culture has also been shown to cause significant remodeling of many vessels in response to altered mechanical forces [95-98] and growth factors [99-103]. Although only a few of these studies used segments of arteries similar to our study, all used extracranial arteries. Yamakawa [104] reported the only prior ex vivo culture

wherein cerebral arteries were exposed to growth factors. Culture times were very short, 5 to 30 minutes, and the growth factor used was PDGF-BB. They showed that in vivo geometry was not maintained. While contraction to ET-1 was reported, the results were not recorded in a manner that could determine if any remodeling occurred. A lack of similar cultures makes our results difficult to compare.

Wagner and Humphrey [88] fit acute basilar artery data with the same active and passive models, thus allowing for direct comparison of associated parameter values. Passive parameters for cultures with both control media (Table 4.2) and media supplemented with growth factors (Table 4.5) showed similar values and trends as passive acute data, though the control cultured data had a larger range in parameter values as evidenced by a larger standard deviation (Table 4.2). Comparing RMS values (Tables 4.2 and 4.5) showed that fits for cultured vessels were just as good as those of passive acute vessels ($RMS = 3.93$). For active parameter values, b was found to be twice as large for control and growth factor cultures (Tables 4.3 and 4.6) as those found for acute active data. Values of q were also found to be double for control cultures (Table 4.3) compared to acute active data. All other active parameter values were found to have similar values for acute and cultured vessels. These differences in parameter values may be due in part to the active model not fitting all culture data as well as the acute data. Mean RMS for active acute fits is 7.32. For cultured data, mean RMS was much higher: 29.54 and 23.77 for control and growth factor cultures, respectively.

In this study, we cultured rabbit cerebral arteries for 5 days and contractility was lost over the culture while there was no evidence of vessel remodeling. Thus, inducing

vessel remodeling with growth factors was not successful. While our results are negative, they are also intriguing, and support the idea that if smooth muscle cell tone cannot be maintained throughout culture, then inward remodeling cannot occur (at least in response to the growth factors used). Smooth muscle cells may not be directly involved with the remodeling, but our results suggest that viable SMCs are necessary for inward remodeling. Therefore contractility, a good measure of smooth muscle viability, may be an indirect way of accounting for a vessels ability to remodel.

CHAPTER V

A 3D MICROSTRUCTURAL ARTERY MODEL WITH COLLAGEN FIBER

ORIENTATION AND SMOOTH MUSCLE CELL ACTIVATION

INTRODUCTION

Our primary goal is to characterize the 3-D mechanics of intracranial (muscular) arteries via a microstructurally motivated constitutive relation for the stress response that incorporates residual stresses, transmural collagen fiber orientations, and smooth muscle activation. Finlay et al. [34] and Canham et al. [12] have reported extensive findings on the microstructure of collagen in intracranial arteries. Medial collagen is oriented primarily in the circumferential direction whereas adventitial collagen is distributed widely about an axial orientation. This transmural variation of collagen orientation through the arterial wall suggests the need for a 3D model to characterize the mechanical behavior of these arteries.

Whereas 2D models of wall mechanics are sufficient for computing mean wall stresses as well as modeling changes in the clinically important metrics of caliber and structural stiffness, 3D models can help bridge our understanding between mechanics and mechanobiology. Cells respond to changes in their local mechanical environment, often via changes in migration, proliferation, differentiation, apoptosis, and even production of diverse proteins, glycoproteins, growth factors, cytokines, proteases, and vasoactive molecules [35]. Calculation of distributions of stress across the wall can thus

be correlated to local changes in cell activity, thus providing more insight into the mechanobiology.

Smooth muscle activation is of particular importance in cerebral arteries due to autoregulation, the ability to maintain blood flow at a nearly constant rate despite changes in blood pressure. Autoregulation occurs by two means of smooth muscle activation: myogenic response and chemical mechanism [10]. Myogenic responses occur when a vessel is distended, which stretches the smooth muscle and results in a corresponding contraction [18, 19]. Chemical responses occur when a vessel is exposed to vasoactive molecules, which in turn cause the smooth muscle to relax or contract [10]. A model of cerebral artery activation should take into account both myogenic and metabolic means for smooth muscle activation.

In this paper, we measure opening angles via standard ring tests, collagen fiber orientations using multiphoton nonlinear optical microscopy (NLOM), biaxial biomechanical tests that include varying the levels of smooth muscle activation, and standard light as well as fluorescence microscopy to build a 3D constitutive relation for an intracranial (basilar) artery in the rabbit.

METHODS

Opening angles were measured from sections of basilar arteries studied in Wagner and Humphrey [88]; 1 mm rings were cut, placed in a 37°C normal saline solution (9 g NaCl/L), and allowed to acclimate for 30 minutes. The rings were then mounted so they were suspended in the saline (Fig. 5.1), cut radially, and imaged after 2

hours. The associated opening angle Φ_0 was measured using ImageJ (Fig. 5.1), then converted to Θ_0 using,

$$\Theta_0 = \pi - \Phi_0 \quad . \quad (5.1)$$

Wall thickness was not measured accurately during the opening angle tests, but it did not appear to change from the traction-free (unloaded) to the stress-free configuration.

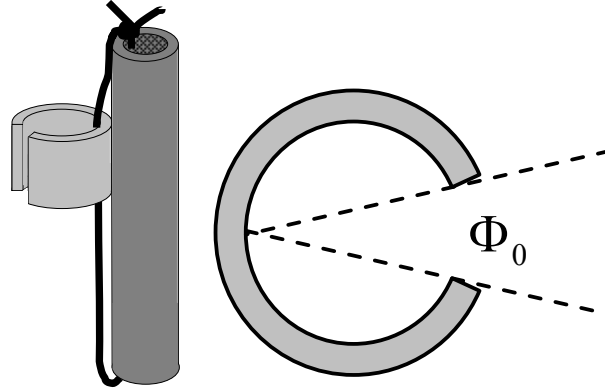


Fig. 5.1 Schematic of opening angle setup and measurement Φ_0 .

NLOM images of basilar arteries under in vivo loaded conditions [88] were taken at 1 micron steps through the wall and processed using ImageJ and Continuity (courtesy Prof. A McCulloch, UCSD). Images were first cropped to remove areas not tangent to the optical plane; Continuity was then used to quantify the number of collagen fibers and their orientations, α^{loaded} (Fig. 5.2) within each field. The number of collagen fibers was then normalized using

$$Norm.Fibers_s^{\alpha^{loaded}} = \frac{Fibers_s^{\alpha^{loaded}}}{M}, \quad (5.2)$$

where $Fibers_s^{\alpha^{loaded}}$ is the number of collagen fibers in slice s at orientation α^{loaded} , and M is the total number of fibers in all slices. For an individual specimen, α_{load} was converted to α_0 in the reference configuration using

$$\alpha_0 = \tan^{-1} \left(\frac{\lambda_z}{\lambda_\theta} \tan \alpha^{loaded} \right). \quad (5.3)$$

Because collagen fibers were averaged from 6 vessels, normalized radii were used to calculate the circumferential stretch λ_θ . Normalized radii were defined as

$$r_n = \frac{r - r_i}{h} \in [0, 1], \quad R_n = \frac{R - R_i}{H} \in [0, 1], \quad (5.4)$$

where r_i and R_i are loaded and unloaded inner radii, h and H are loaded and unloaded wall thickness, and r_n and R_n are loaded and unloaded normalized radius.

Circumferential stretch can then be calculated by

$$\lambda_\theta = \frac{r_n h + r_i}{\rho_n H + \rho_i}. \quad (5.5)$$

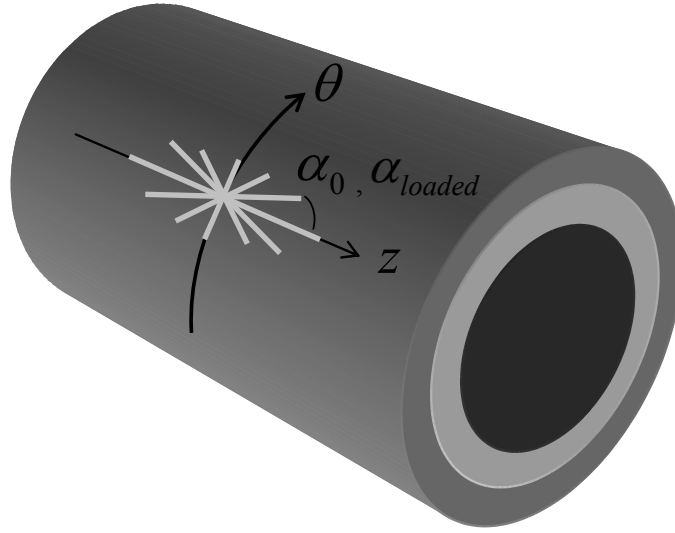


Fig. 5.2 Schematic of collagen fiber angle measurement α .

A modified Von Mises distribution, better known as a circular normal distribution, was used to fit the collagen fibers of each slice through the thickness of the wall from the NLOM images. This distribution is denoted as

$$CF = \frac{c}{2\pi I_0(k)} e^{k \cos(\alpha_{loaded})}, \quad (5.6)$$

where c is a dimensionless scaling factor, k a dimensionless parameter, α^{loaded} the angle of the fiber in a loaded condition measured relative to the axial direction and ranging from $-\pi$ to π (Fig. 5.2), and I_0 is a modified Bessel function of the first kind and order zero. Measured collagen fiber angles were fit using this function via nonlinear regression (Matlab function `fminsearchbnd`) using the following objective function,

$$e = \sum_{i=1}^N \left(\frac{Theory_i - Exp_i}{N} \right)^2, \quad (5.7)$$

where *Theory* is the value computed from the model and *Exp* represents data available from the experiment. Both c and k vary with normalized position through the artery wall, which can be described by the following functions,

$$c(r_n) = Ae^{-B\left(1+\frac{r_n-1}{C}\right)} + D, \quad (5.8a)$$

and

$$k(r_n) = \frac{A}{1 + e^{-B(r_n-C)}} - D, \quad (5.8b)$$

where A , B , C , and D are dimensionless parameters. These functions, c and k , were also fit to data using a nonlinear regression (Matlab function `fminsearchbnd`) and objective function Eq. 5.4.

Biaxial biomechanical data for rabbit basilar and carotid arteries under passive, active, and basal conditions [88] were used along with new opening angle data to calculate local radial, circumferential, and axial stretch via

$$\lambda_\theta = \frac{\Theta_0 R}{r\pi\lambda_z}, \quad \lambda_\theta = \frac{r\pi}{\Theta_0 R}, \quad \text{and} \quad \lambda_z = \frac{l}{L}, \quad (5.9, 5.10, 5.11)$$

where r is the loaded radius, l is the loaded axial length, L is the stress-free axial length, and

$$R = \sqrt{\frac{\pi\lambda_z}{\Theta_0} (r^2 - r_i^2) + R_i^2}, \quad (5.12)$$

where r_i is loaded inner radius and R_i is stress-free inner radius. Using incompressibility and assuming that wall thickness does not change from the stress-free to the unloaded configuration,

$$R_i = \frac{\pi}{\Theta_o} \left(\rho_i + \frac{h}{2} \right) - \frac{h}{2} \quad (5.13)$$

where $h = \rho_o - \rho_i$, and ρ_i and ρ_o are unloaded inner and outer radii, respectively.

A strain energy function developed in Gasser et al. [52], hereafter referred to as the distributed fiber model, was used to model the passive data. It is,

$$W = \frac{c}{2} (I_1 - 3) + \frac{c_1^k}{2c_2^k} \left\{ \exp[c_2^k E^2] - 1 \right\}, \quad (5.14)$$

where I_1 is the first invariant of the right Cauchy-Green tensor (\mathbf{C}), c is a material parameter which models the elastin contribution (assumed to be isotropic), c_1^k (kPa) and c_2^k are material parameters associated with the collagen fibers, and

$$E = \mathbf{H} : \mathbf{C} - 1, \quad (5.15)$$

where

$$\mathbf{H} = \int_{\alpha_0} CF_{Norm}(\alpha_0, r) \mathbf{M}(\alpha_0) \otimes \mathbf{M}(\alpha_0) d\alpha_0, \quad (5.16)$$

$$\mathbf{M}(\alpha_0) = 0\hat{\mathbf{e}}_r + \sin(\alpha_0)\hat{\mathbf{e}}_\theta + \cos(\alpha_0)\hat{\mathbf{e}}_z, \quad (5.17)$$

and

$$CF_{Norm}(\alpha_0, r) = \frac{e^{k \cos(\alpha_0)}}{\int_{\alpha_0} e^{k \cos(\alpha_0)}}. \quad (5.18)$$

CF_{Norm} has been normalized in the manner described by Gasser et al. [52]. Combining Eqs. 5.15 -5.17 gives

$$E = \lambda_\theta^2 \int_{\alpha_0} CF(\alpha_0, r) \sin^2(\alpha_0) d\alpha_0 + \lambda_z^2 \int_{\alpha_0} CF(\alpha_0, r) \cos^2(\alpha_0) d\alpha_0 - 1. \quad (19)$$

Passive radial, circumferential and axial Cauchy stresses are then

$$\sigma_r^{Passive} = -p + \lambda_r^2 c \quad (5.20)$$

$$\sigma_\theta^{Passive} = -p + c \lambda_\theta^2 + 2 \lambda_\theta^2 c_1 E \exp[c_2 E^2] \int_{\alpha_0} CF(\alpha_0, r) \sin^2(\alpha_0) d\alpha_0, \quad (5.21)$$

$$\sigma_z^{Passive} = -p + c \lambda_z^2 + 2 \lambda_z^2 c_1 E \exp[c_2 E^2] \int_{\alpha_0} CF(\alpha_0, r) \cos^2(\alpha_0) d\alpha_0, \quad (5.22)$$

and, from radial equilibrium,

$$p = P_i + \sigma_r^{Passive^e} - \int_r^{\frac{1}{r}} \left(\sigma_\theta^{Passive^e} - \sigma_r^{Passive^e} \right) dr, \quad (5.23)$$

where P_i is the pressure at the intimal (inner) surface. The pressure at the adventitia was nearly zero in our experiments, thus intimal and transmural pressure equal. Intimal pressure and axial force can be calculated by

$$P_i = \int_{r_i}^{r_o} \frac{1}{r} \left(\sigma_\theta^{Passive^e} - \sigma_r^{Passive^e} \right) dr \quad (5.24)$$

and

$$f = \pi \int_{r_i}^{r_o} \left(2 \sigma_z^{Passive^e} - \sigma_r^{Passive^e} - \sigma_\theta^{Passive^e} \right) r dr. \quad (5.25)$$

To account for smooth muscle cell activation, we modified an active model from Wagner and Humphrey [88] to work for a 3D model. The strain energy function then becomes,

$$W_{Total} = W + TM_1 \otimes M_1 + TM_2 \otimes M_2, \quad (5.26)$$

where,

$$T = 0 \hat{e}_r + T_\theta \hat{e}_\theta + T_z \hat{e}_z, \quad (5.27)$$

$$M_1 = 0\hat{e}_r + \lambda_\theta\hat{e}_\theta + 0\hat{e}_z, \quad (5.28)$$

and

$$M_2 = 0\hat{e}_r + 0\hat{e}_\theta + \lambda_\theta\hat{e}_z. \quad (5.29)$$

Radial stress is unaffected by the active model. Total circumferential and axial stresses are

$$\sigma_\theta^{Total} = \sigma_\theta^{Passive} + T_\theta \text{ and } \sigma_z^{Total} = \sigma_z^{Passive} + T_z, \quad (5.30)$$

where

$$T_\theta = T_M e^{-b\left(\frac{\lambda_M - \lambda_\theta}{\lambda_M}\right)} \frac{1}{1 + e^{-d(\log([ET-1]) + c)}}, \quad (5.31)$$

and

$$T_z = (-q\lambda_\theta + p) \frac{1}{1 + e^{-r(\log([ET-1]) + s)}}. \quad (5.32)$$

Parameters are defined as follows: T_M (kPa) is the maximum stress generated by the SMCs, λ_M is the circumferential stretch at which SMCs achieve maximal stress, b , c , d , r and s are dimensionless parameters, p (kPa) and q (kPa) are material parameters, and $[ET-1]$ a concentration of endothelin-1 which gives the same level of chemical activation of SMCs as measured. Intimal pressure and axial force can be calculated by Eqs. 5.24 and 5.25 by substituting total for passive stress.

Best-fit values of material parameters for the passive response were determined via nonlinear regression (Matlab function lsqnonlin) to minimize the objective function

$$e = \sum_{i=1}^N \left[\left(\frac{P_i^{Theory} - P_i^{Exp}}{P_{Average}^{Exp}} \right)^2 + \left(\frac{f_i^{Theory} - f_i^{Exp}}{f_{Average}^{Exp}} \right)^2 \right], \quad (5.33)$$

where N is the number of data points, ‘Exp’ denotes experimental data, and ‘Theory’ denotes calculated variables. This function accounts for differences between theoretically predicted and experimentally measured values. Best fits were found when free parameters were c , c_1, c_2 , C and D . All parameters were constrained to respect a lower bound of 0. Parameters in the active model were determined via nonlinear regression of data (Eq. 5.33) by first fixing those parameter values associated with the passive response. All active curves (4 concentrations of ET-1) were fit simultaneously.

Outlier detection was performed on the parameter values. All parameters were considered non-normally distributed and the log of the values was used to determine means and standard deviations. Any values falling outside the range of the mean plus or minus two standard deviations was considered to be an outlier and the data set was removed.

Tissue samples from a previous study [88] were used to look further at collagen, smooth muscle, elastin, and endothelin B receptors. Sirius red staining was used to assess collagen; this required incubating unstained slides in picro-sirius red solution for 1 hour, washing in two changes of acidified water, dehydrating in 3 (2 minute) washes of 100% ethanol, and clearing for 5 min in xylene. The natural (auto) fluorescence of elastin was used during fluorescent imaging. Smooth muscle and endothelin B receptors (ETB-R) were stained using primary antibodies rabbit polyclonal alpha smooth muscle actin (α SMA) (Abcam, ab 15734) and sheep polyclonal ETB-R (Abcam, ab 50658)

respectively. Unstained slides were first incubated in 1% Bovine Serum Albumin (BSA) in a phosphate buffered saline with 0.5% Tween for 30 minutes. Primary antibody was then added for an overnight incubation. Slides were incubated with secondary antibody (Alexa Flour 594 goat anti-rabbit IgG (Invitrogen, A-11012) and Alexa Flour 594 donkey anti-sheep IgG (Invitrogen, A-11016)) for 1 hour. Cover slip mounting media with DAPI (Fluoroshield with DAPI (Sigma, F6057)) was then applied as a general cell marker.

Images of all stained sections were captured with an Olympus BX-51 Research microscope. Images of sirius red stained slides were captured with bright field and circularly polarized illumination. Fluorescent stained slides were imaged using the appropriate filter with exposure time determined using a control section. PSR and fluorescent images were processed using ImageJ. Images were converted to grayscale, and using threshold the area of interest was selected and then measured. The total area of the vessel was measured in a similar fashion and area fractions were computed using

$$AF = \frac{AI}{TA}, \quad (5.34)$$

where AOI is area of interest and TA is the total area of the vessel. Area fractions of collagen and elastin were then used to calculate collagen to elastin ratio (C:E).

RESULTS

Opening angles values (Table 5.1) varied considerably, which is reflected in the standard deviation. This is common for opening angle measurements. Conversely, in vivo axial stretch has no variation as this was prescribed [88].

Table 5.1 Reference inner and outer radii, wall thickness, in vivo axial stretch, opening angles ($\Theta_0 = \pi - \Phi_0$), collagen to elastin ratio (C:E) and area fraction of smooth muscle.

R_i (μm)	Θ_0 (rads)	ρ_i (μm)	h (μm)	$\lambda_z^{in vivo}$	C:E	smooth muscle
259.5 ± 64.99	1.66 ± 0.42	282.25 ± 28.97	64.16 ± 10.61	1.15 ± 0.00	4.44 ± 1.46	0.30 ± 0.11

NLOM revealed collagen fiber orientations (Fig. 5.3) to be primarily circumferential in the media, diagonally oriented in the transition area between media and adventitia (two thirds of the way through the wall), and axially distributed within the adventitia. Fits of loaded collagen fiber orientations can be seen in Fig. 5.3. Parameters k and c for the altered von Mises function were plotted (Fig. 5.4) with respect to normalized radius and subsequently fit with Eqs. 5.5 and 5.6, respectively. These fits and their associated parameter values can be found in Table 5.2.

Associated parameters for the unloaded collagen fiber orientations can be found in Table 5.2. Unloaded collagen fiber orientations show the similar trends seen in the loaded orientations. For both c and k parameter A controls the amplitude, parameter D allows for the translation of the function along r_n , while parameter C does the same along k or c . Changes in B , associated with k , directly alter the slope between the two tails of the sigmoid function. Changes in B , associated with c , inversely alter the width of the peak. Unloading leads to a smaller amplitude, positive translation along c , and increase in the width of the peak for the function describing c . Looking at k after unloading reveals the amplitude and slope between the tails is increased and there is a positive translation along both r_n and k .

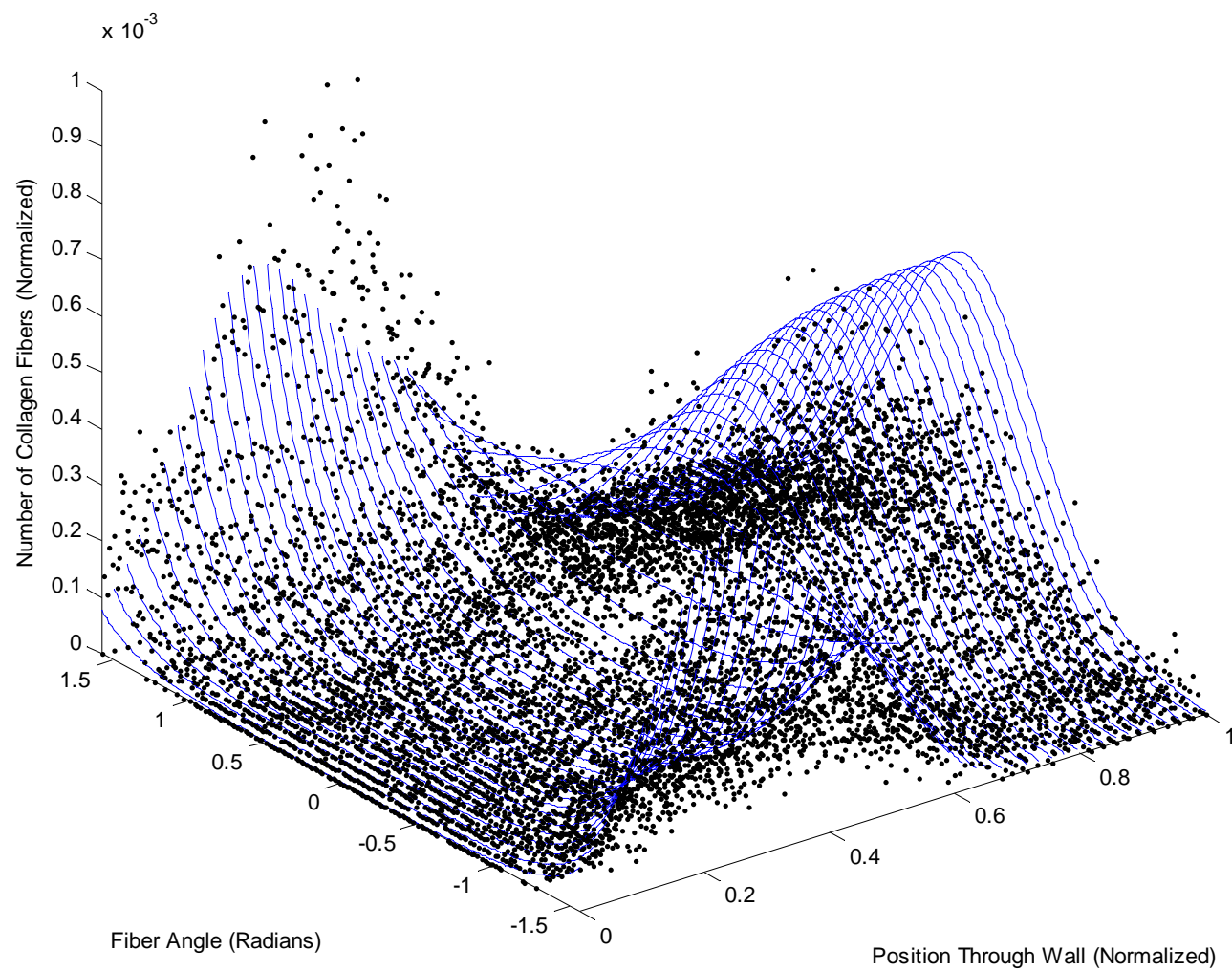


Fig. 5.3 Quantified loaded collagen fiber angles from NLOM images (‘•’) and Von Mises fits (‘-’).

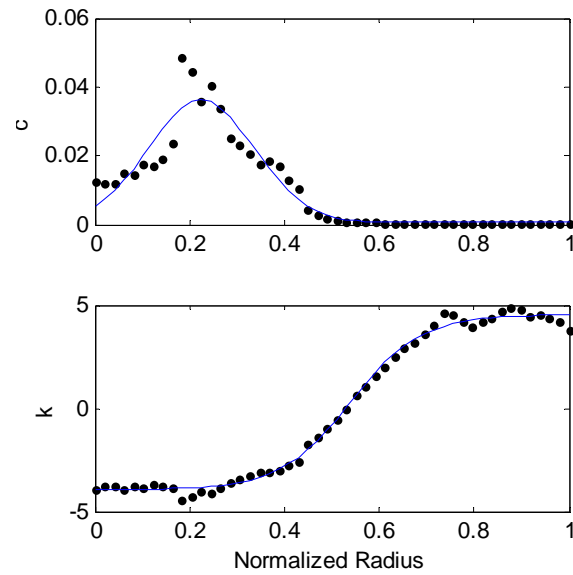


Fig. 5.4 Fits (‘-’) and data (‘•’) of modified von Mises function parameters c and k .

Table 5.2 Mean Best-fit parameters for fits of modified von Mises function parameters c and k for loaded and unloaded collagen fiber orientations. Unloaded values are reported as means.

	c				k			
	A	B	C	D	A	B	C	D
Loaded	3.56E-02	24.39	0.78	7.14E-04	8.49	13.36	0.46	4.54
Unloaded	2.06E-02	18.16	0.76	3.15E-04	8.99	15.41	0.57	3.16

Passive basilar data and fits for the fiber angle distribution model can be seen in Fig. 5.5 with associated parameters in Table 5.3. Elastin parameter c was larger than values previously found in four fiber family model fits [88]. Collagen stiffness parameters c_1 and c_2 values were similar to those found for axial collagen in fiber family model fits [88]. Plots of Cauchy stress (Fig. 5.6) show that radial stress reflects the boundary conditions, starting at negative luminal pressure (-80 mmHg = -10.7 kPa) and reaching zero at the outer radius. Circumferential and axial stress both start out high at the inner radius, with circumferential stress slightly higher, and decrease dramatically when 20% of the way through the wall.

Table 5.3 Mean best-fit parameter values for distribution fiber model fits.

	c	c_1	c_2	C	D	RMS
Mean	1.07E-09	29.71	3.32	0.46	9.91E-09	1.73
Std Dev	6.60E-10	22.08	1.34	0.17	2.28E-09	0.38

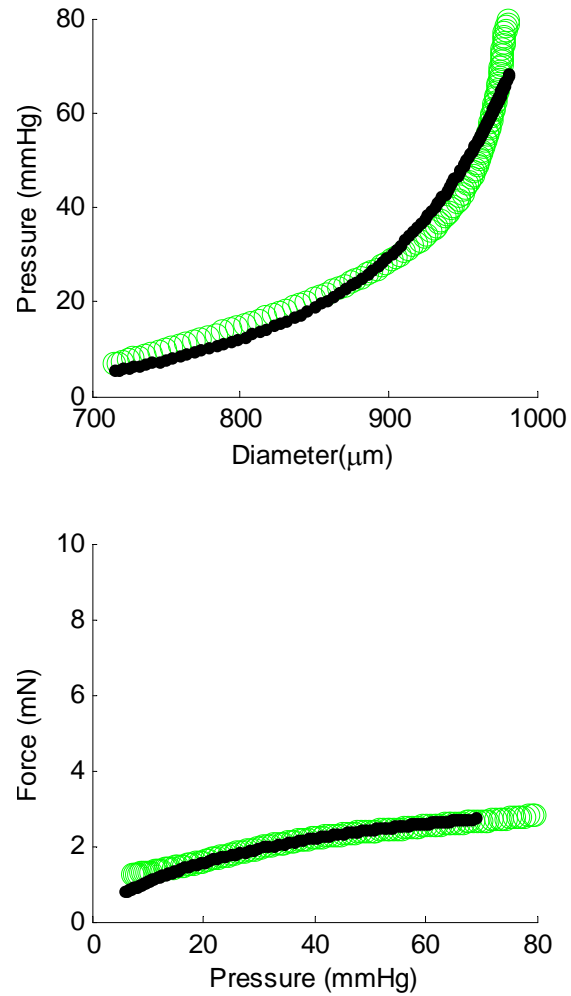


Fig. 5.5 Representative passive data and distribution fiber model fits.

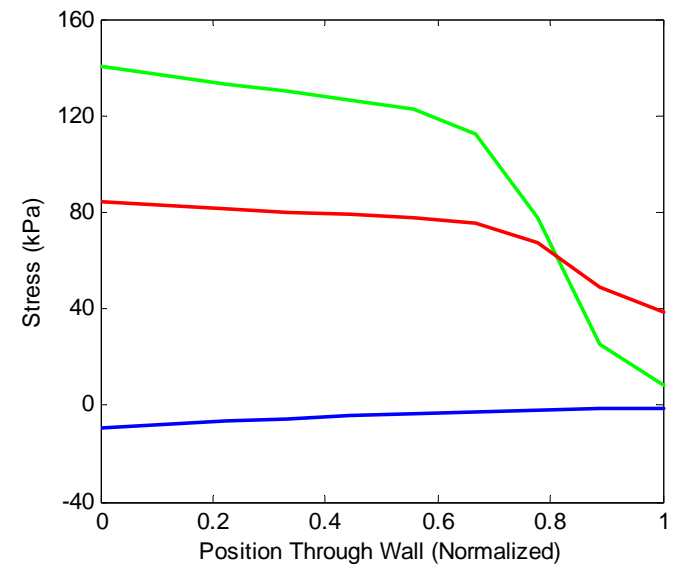


Fig. 5.6 Radial (blue), axial (red) and circumferential (green) stress data from representative distribution fiber model fits at a loaded state of $P=80\text{mmHg}$.

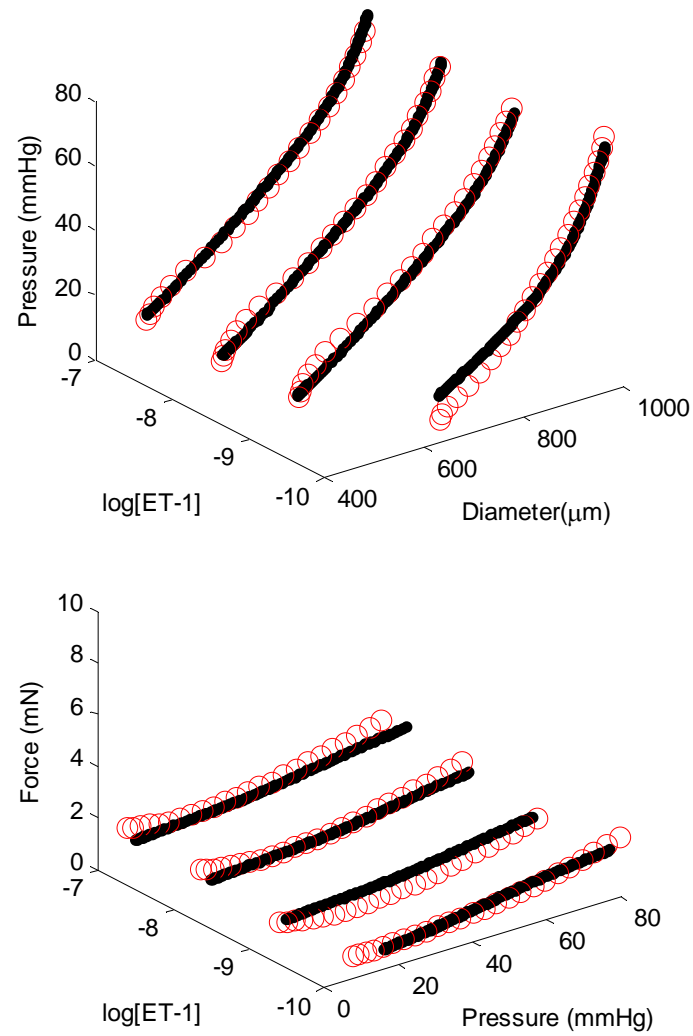


Fig. 5.7 Representative active data and active model fits.

Table 5.4 Mean best-fit parameter values for active model fits.

	T_M	λ_M	b	d	c	q	p	r	s	RMS
Mean	49.76	1.44	8.68	15.70	9.95	17.93	13.55	55.18	10.10	4.85
Std Dev	3.28	0.13	0.66	15.02	0.39	6.00	5.46	94.40	0.27	1.49

Active fits can be seen in Fig. 5.7 with associated parameter values in Table 5.4. Active basilar artery data and parameter fits differ from those in Wagner and Humphrey [88]; they are poorer, with differences evident in parameters T_M , λ_M , b , and p .

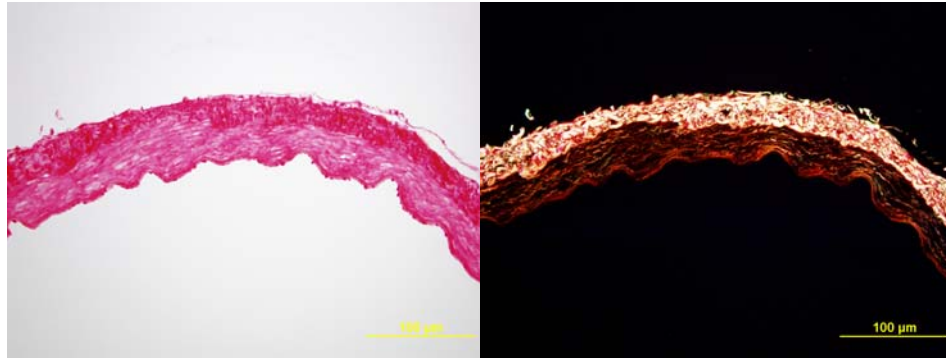


Fig. 5.8 Bright and dark field images of Sirius red stained sections.

Images of PSR stained sections (Fig. 5.8) revealed collagen to be predominantly in the adventitia. Analyzing these images showed basilar have a collagen fraction of 0.24. Staining for α SMA showed densely packed smooth muscle in the media of the basilar artery (Fig. 5.9). Results from analyzing these images can be found in Table 5.1. ET-B receptors were found throughout the wall of the basilar artery (Fig. 5.10).

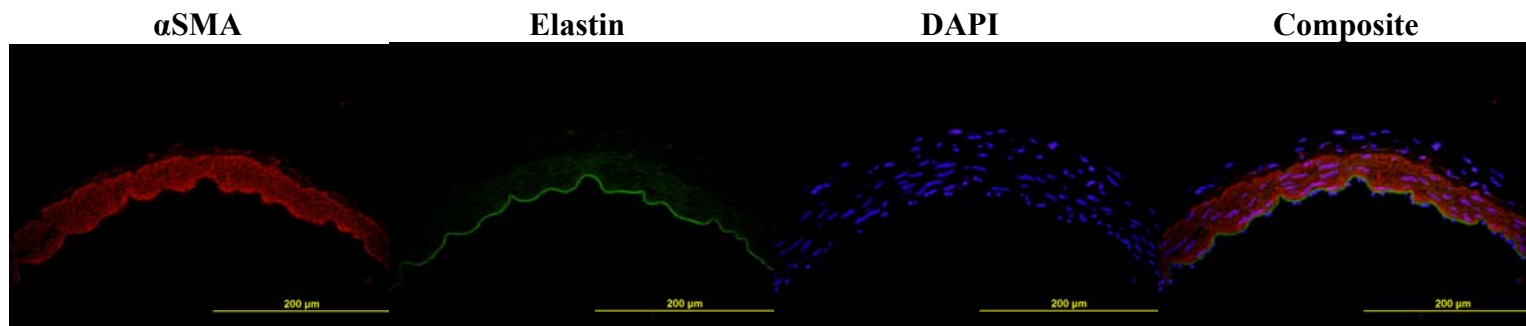


Fig. 5.9 Florescent images of α SMA, elastin, DAPI, and a composite showing all three. Images were taken at 40x magnification.

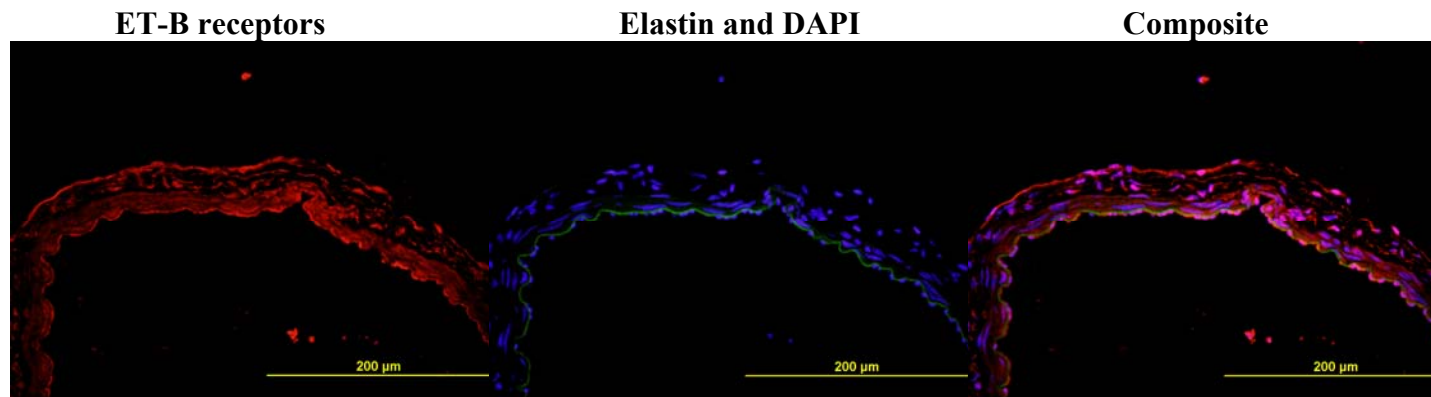


Fig. 5.10 Florescent images of ET-B receptors, elastin and DAPI, and a composite showing all three. Images were taken at 40x magnification.

DISCUSSION

Collagen, elastin, and smooth muscle are considered to be the primary structural constituents of arteries. Therefore, to properly understand the mechanical behavior of arteries we need to understand both the material properties of these constituents and their transmural distributions. Our 3D model takes all of these into account in order to more accurately predict the mechanical behavior of intracranial arteries.

Results from our immunohistochemistry (IHC) and histology for carotid arteries showed numerous layers of elastin with circumferentially oriented SMCs in between as well as an adventitia primarily composed of collagen, which agrees with previous histological results from [56, 88]. Results from IHC and histology for basilar arteries showed a distinct internal elastic lamina, a media dominated by circumferentially oriented SMCs, but also containing faint layers of elastin and circumferential collagen, and an adventitia consisting of oriented collagen fibers. These agree with histological work from Wagner and Humphrey [88], but not Bunce [56], where dog basilar arteries stained for elastin showed interrupted elastin at the medial-adventitial border. Interrupted elastin was not seen in our images, nor was faint elastin found in the media. These differences may be due to the two distinct methods used to view elastin.

More detailed information on collagen was obtained through NLOM. These images revealed adventitial and medial collagen in the basilar artery. Comparing these results to PSR stained sections (Fig. 5.8) suggests that the collagen fraction isn't accurate for basilar arteries. PSR images in Fig. 5.8 only show collagen in the basilar adventitia, which is incongruous with basilar NLOM data. Prior work has established that

adventitial collagen is primarily type I and medial collagen is type I and III [4] and that collagen types I, II, and III stain with PSR [105]. PSR works by binding with collagen and increasing its natural birefringence [105]; more oriented mature collagen has greater natural birefringence. Therefore, larger type I collagen fibers in the adventitia may be so bright under polarization that smaller type III and type I fibers in the media cannot be seen. In order to quantify medial collagen, the adventitia could be blocked out as in Hu et al. [106]. Nonetheless, using a collagen type I to III ratio of 2.98 ± 0.78 from [107] we can estimate basilar medial collagen. C:E for basilar arteries then becomes 5.94 ± 1.96 , which is larger than the original C:E (Table 5.1). Nawagasawa et al. [108] found C:E = 5.1 ± 0.9 for the dog basilar artery, which both of our basilar C:E ratios fall within.

Of the three primary constituents of arteries, smooth muscle is unique for its ability to contract. In order to model this behavior, it is important to understand how smooth muscle cells are activated. ET-1, the only endothelin produced by vascular endothelial cells [109], was used to increase smooth muscle activation. ET-1 acts primarily through ET-B receptors. ET-B receptors were initially described only on vascular endothelium and found to regulate relaxation through nitric oxide (NO) and prostacyclin (PGI₂) [110]. Later ET-B receptors were also found on vascular smooth muscle as well as fibroblasts, where they mediate vasoconstriction and remodeling effects [110-112]. Despite this variation in function by location, only vasoconstriction was induced by applying ET-1 extra-luminally [88]. IHC staining of ET-B receptors was reported previously by Lin-Hong et al. [113] using fresh controls of rat basilar arteries, with similar results of ET-B receptors seen through the arterial wall.

Many models have been used to characterize arterial mechanics, yet the Fung model is one of the most widely used. The Fung model [114] uses an exponential strain energy function in terms of Green strains to model anisotropic behavior. The microstructure of the artery is not taken into account by this model, but it still realistically predicts mechanical behaviors [3, 29, 48, 115, 116]. Because of this, and its relative simplicity, it is still used and new models are often compared to it. Our model is similar in that it uses an exponential function to describe the mechanical contribution of collagen. One of the first models to take into account differences in material properties between the media and adventitia was proposed by von Maltzahn et al. [54], based in large part on the Fung approach. Known as a two layer model, it used separate strain energy functions for the media and adventitia. The adventitia was modeled as an anisotropic material due to the behavior of collagenous tissue; a unique strain energy function was proposed for the media after trying isotropic, transverse isotropic, and anisotropic functions. Similarly, our model includes isotropic and anisotropic contributions, but they are in the same strain energy function rather than separate ones. Von Maltzahn's model was found to fit canine carotid data (Cox 1975b) well, but plots of stresses over the normalized radius clearly showed that material discontinuities can arise by using two strain energy functions.

Another two layered model, proposed by Demiray [55], consisted of two separate cylindrical layers for the media and adventitia. The media was approximated as an orthotropic elastic material. It was reasoned that the adventitia was composed of fibers and fibrils and could therefore be approximated as isotropic. Strain energy functions for

the media and adventitia were described using exponentials. Parameter values for both strain energy functions were determined from biaxial testing of media and adventitia independently. A complete vessel was then simulated; it depicted a nonlinear relationship, but was never compared to experimental data. It is doubtful if experimental data would have been accurately described, as elastin in the media and collagen fibers in the adventitia have later been seen to be represented better by isotropic and anisotropic functions, respectively. Our model avoids material discontinuities by using a single strain energy function and differentiating between media and adventitia with our collagen fiber distribution.

A multi-layer model was proposed by Holzapfel et al. [48] that differed from previous two layer models by having one strain energy function, but different material parameters for each layer. The strain energy function includes anisotropic and isotropic deformations to account for collagen and all other constituents, respectively. Our model uses a similar strain energy function. The anisotropic portion of the Holzapfel model, based on histological data, assumes two helically oriented collagen fiber families. In a later paper [117], cell nuclei were used to obtain better estimation of collagen orientation in the adventitia and media. The isotropic portion is a classic neo-Hookean model. Holzapfel [48] compared this model to Fung's and found it to give reasonable fits, but due to the two sets of material parameter, computed transmural distributions of stress again were discontinuous at the medial-adventitial border. As noted previously, if the Fung model is implemented as a two layer model, the number of parameters double, unlike the Holzapfel [116].

Stergiopolus et al. [29] used the Holzapfel model [48] as basis for a more structurally based model. Like the Holzapfel model, their strain energy function had both isotropic and anisotropic parts. Parameters were created to bear more physical meaning. The isotropic portion included the fraction of elastin and its elastic modulus. The anisotropic portion included collagen fraction, its elastic modulus, waviness, and orientation. Unlike the Holzapfel model, the Stergiopolus model considers only the media rather than the whole vessel. To test the model's capabilities inflation tests on rat carotids with the adventitia removed were fit with a Fung, Holzapfel, and their new model. All three models fit the data well, but the Stergiopolus model fit best. While our model does not incorporate collagen and elastin fractions directly like the Stergiopolus model, it does so implicitly and is able to accurately describe passive properties.

Gasser et al. [52] proposed a 3D mechanical model, which assumed collagen to have a bimodal distribution. It used a strain energy function that simplified to the one originally proposed by Holzapfel and colleagues. This model was applied to two examples. The first was inflation with no axial loading of thin-walled tube, which represented the iliac artery. Using a least squares fit, they obtained the following values: $c=7.64$, $c_1=9996.6$, $c_2=524.6$. Our model is similar with the primary deviation being our collagen distribution (Eq. 5.18), which has no radial components, but contains parameters (Eq. 5.7) that vary with radius. Our value for parameter c is much larger, but we have much smaller values for c_1 and c_2 . Limitations of this model, and ours, are that elastin is modeled as isotropic, which may not be the case based on IHC images (Fig. 5.11) for both the basilar and carotid artery.

Our fiber distribution model could potentially be done for any vessel. All that would be required is opening angle, basic geometric, and collagen fiber orientation information. If needed, Eqs. 5.8a and 5.8b could be easily altered to accommodate better fits collagen fiber orientation. Preliminary data for the application of the fiber distribution model to a carotid artery can be seen in Table 5.5 and Fig. 5.11.

Table 5.5 Reference inner and outer radii, wall thickness, in vivo axial stretch, opening angles ($\Theta_0 = \pi - \Phi_0$), collagen to elastin ratio (C:E) and area fraction of smooth muscle for the carotid artery. Means values followed by standard deviations.

R_i	Θ_0	ρ_i	h	$\lambda_z^{in vivo}$	C:E	smooth muscle
1861.96 ± 183.72	1.12 ± 0.56	575.63 ± 61.07	271.78 ± 34.30	1.68 ± 0.12	2.95 ± 1.13	0.35 ± 0.17

Through our results, we have quantified collagen fiber orientation in loaded basilar artery in a manner never done before. Using this and previous recorded biaxial mechanical data [88], we were able to accurately fit passive data using a model that reflected collagen microstructure. The active model was not as successful and gave less than ideal results for active fits. However, our 3D fiber distribution model gives greater insight in to the distribution of stresses through the passive wall of intracranial arteries.

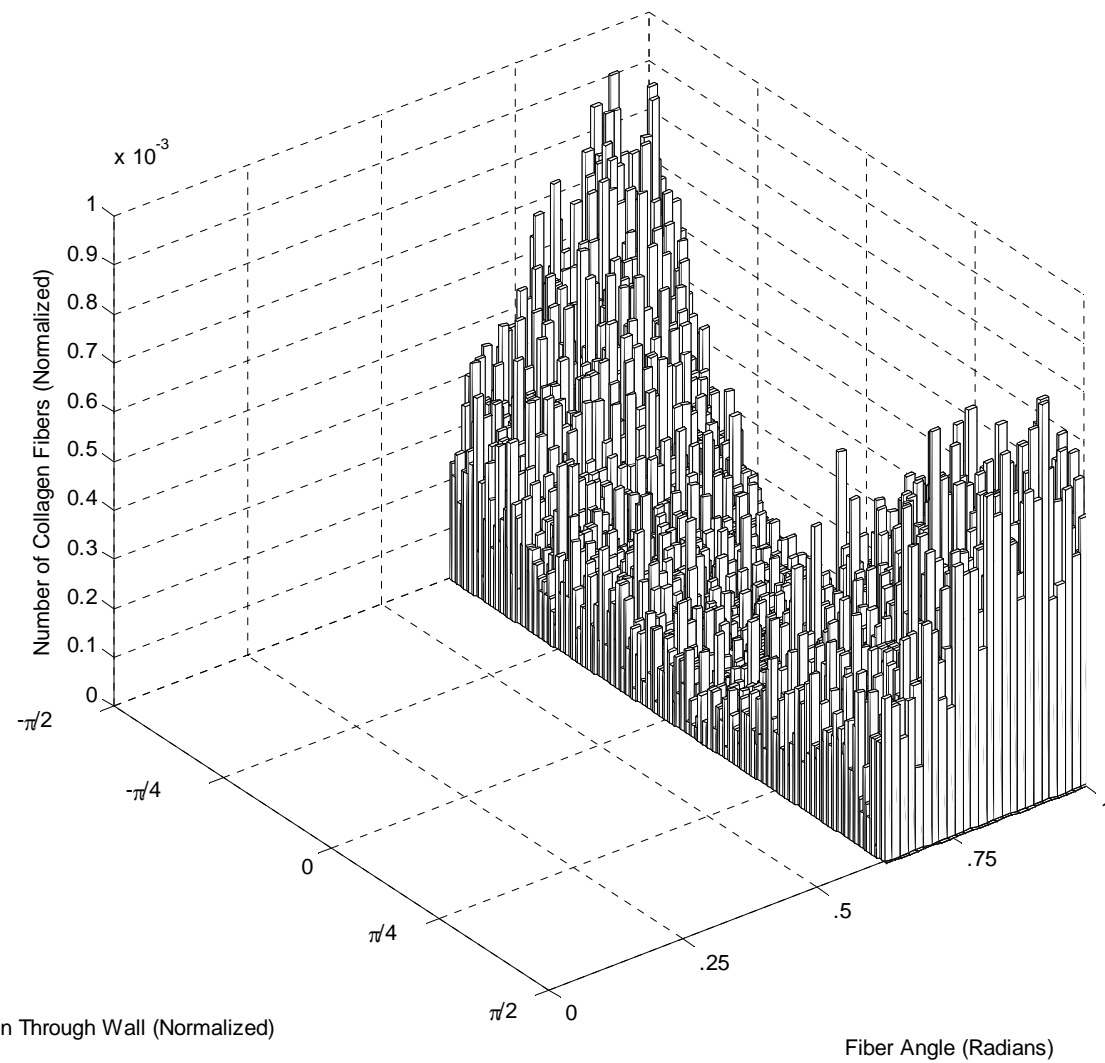


Fig. 5.11: Quantified loaded carotid collagen fiber angles from NLOM images.

CHAPTER VI

CONCLUSION

SUMMARY

Cerebrovascular disease involves adaptations of cerebral vasculature structure and function. The ability to characterize properties of normal cerebral vasculature and how it differs from extracranial arteries furthers our understanding of disease conditions. Findings presented herein lead to a more detailed, better characterization of normal cerebral arteries through experimental methods and modeling.

We determined structure and mechanical behavior of the normal basilar artery using NLOM and the four fiber family model. Through NLOM, the collagen fiber distribution and orientation was measured and the observation was made that collagen becomes less wavy as the vessel is loaded. The first result provides motivation for a more structurally based model, while the second supports the current modeling of collagen fibers in the four fiber family model. The four fiber family model was found to accurately model the mechanical characteristics and collagen microstructure of the basilar artery. Basilar arteries were shown to exhibit typical behavior when smooth muscle was activated, underlining the need for a framework to interpret active wall mechanics.

We created the first model to successfully fit active and passive properties of muscular and elastic artery in the same species. Passive data from basilar and carotid arteries was successfully fit using the four fiber family model, which reflected structural

differences in elastin between the two arteries. Our active model based on myogenic and metabolic mechanism, accurately described smooth muscle cell activation in both vessels and was able to predict levels of smooth muscle cell activation.

We showed that smooth muscle tone is important to vessel viability and its ability to remodel. Control and growth factor ex vivo culture of basilar arteries resulted in a loss contractility over time. Growth factor cultures did not remodel as expected. Therefore, we propose that smooth muscle tone is necessary for remodeling, whether or not it is directly involved in the remodeling process.

Vascular remodeling was not the focus of this work, but we intended to describe native artery mechanics in ways which could be applied to remodeling. Mechanobiology, one aspect of vascular remodeling, requires knowing stresses through the artery wall, which can only be done with a 3D model. We next developed a 3D model taking into account microstructural information, residual stress, and SMC activation to characterize two vessels types.

Our 3D model, incorporated collagen fiber orientation and distribution through the artery wall, and was able to accurately fit passive basilar arteries. Active fits for basilar active fits were less than ideal. Nevertheless, the 3D fiber distribution model allows for the calculation of passive stress distributions through the wall of giving greater insight in to intracranial arteries.

This research has made great strides towards creating a better understanding of intracranial arteries and how they differ from extracranial arteries. In particular our 2D active and 3D passive models are able to better characterize normal cerebral and

extracerebral arteries potential leading to better understanding the etiology of cerebrovascular disease.

RECOMMENDATIONS

While we are quite pleased with our final product of a 3D model capable of characterizing two vessels types, we believe that there are areas where it can be improved. Elastin could be modeled with a new function, as the current isotropic function does not accurately reflect its microstructure. However, it will be difficult due to the discontinuous structure of elastin, which could lead to discontinuities in stress through the wall.

Smooth muscles could also be modeled in more detail. While our model addresses the axial contribution of SMC activation, it is only defined in terms of circumferential stretch and ET-1 concentration. Zahalak [118, 119] has shown the importance of considering axial contribution of smooth and suggested that axial contribution is a function of axial stretch. Additional biaxial tests at multiple concentrations of a vasoconstrictor and multiple axial stretches could clarify this relationship. Responses to other vasoconstrictors should be determined and modeled with attention to the molecular mechanism through which they act.

Additions should be considered in the creation of both a 2D and 3D constitutive model. 2D models aren't as detailed as 3D, but they have been shown to be effective for use in patient specific remodeling [71]. As mentioned previously, 3D models are necessary to bridge mechanics to mechanobiology. Including the aforementioned

additions in a 3D model would help it to more accurately reflect the microstructure resulting in better stress predictions for mechanobiology.

In vivo culture using animal models is the gold standard for disease modeling. More could be learned from disease model by obtain in vivo mechanical data. Masson [80] and Stalhand [120] have shown that this can be done from vessels in vivo. However, to get the most out of any mechanical data it must be used with a well developed model and well developed models requires ex vivo experiments. Therefore it is essential to continue ex vivo mechanical testing.

Ex vivo experiments allow vessels to be put through prescribed motions beyond in vivo ranges during which forces can be measured. Prescribed motions beyond in vivo ranges are necessary to gain a better understanding of material properties. Ex vivo culture still has the potential to be a powerful tool in understanding disease etiology. However, particular care should be taken in choosing the type of vessels culture as much more success has been seen with larger more robust vessels.

This research has made great strides towards creating a better understanding of intracranial arteries and how they differ from extracranial arteries. In particular our 2D active and 3D passive models are able to better characterize normal cerebral and extracerebral arteries potential leading to better understanding the etiology of cerebrovascular disease.

Model development should continue with the help of ex vivo mechanical testing and innovative imaging techniques, such as NLOM, to further incorporate vessel microstructure. In vivo disease models should record and fit mechanical data with an

appropriate, well developed constitutive relation. These techniques can be applied with a broader goal of understanding the contribution of microstructure to vascular mechanics and the role of microstructural components in vascular growth and remodeling.

REFERENCES

- [1] Xu, J., Kochanek, K. D., Murphy, S. L., and Tejada-Vera, B., 2010, "Deaths: Final Data for 2007," Natl. Vital Stat. Rep., **58**(19), p. 2.
- [2] Walker, H. K., Hall, W. D., and Hurst, J. W., 1990, *Clinical Methods : The History, Physical, and Laboratory Examinations*, Butterworths, Boston, MA.
- [3] Hajdu, M. A., and Baumbach, G. L., 1994, "Mechanics of Large and Small Cerebral Arteries in Chronic Hypertension," Am. J. Physiol. Heart Circ. Physiol., **266**(3 Pt 2), pp. H1027-1033.
- [4] Mimata, C., Kitaoka, M., Nagahiro, S., Iyama, K., Hori, H., Yoshioka, H., and Ushio, Y., 1997, "Differential Distribution and Expressions of Collagens in the Cerebral Aneurysmal Wall," Acta Neuropathol. (Berl). **94**(3), pp. 197-206.
- [5] Lee, R. M., 1995, "Morphology of Cerebral Arteries," Pharmacol. Ther., **66**(1), pp. 149-173.
- [6] Walmsley, J. G., 1983, "Vascular Smooth Muscle Orientation in Straight Portions of Human Cerebral Arteries," J. Microsc., **131**(Pt 3), pp. 361-375.
- [7] Finlay, H. M., Whittaker, P., and Canham, P. B., 1998, "Collagen Organization in the Branching Region of Human Brain Arteries," Stroke, **29**(8), pp. 1595-1601.
- [8] Kulik, T., Kusano, Y., Aronhime, S., Sandler, A., and Winn, H., 2008, "Regulation of Cerebral Vasculature in Normal and Ischemic Brain," Neuropharmacology, **55**(3), pp. 281-288.
- [9] Rowe, A. J., Finlay, H. M., and Canham, P. B., 2003, "Collagen Biomechanics in Cerebral Arteries and Bifurcations Assessed by Polarizing Microscopy," J. Vasc. Res., **40**(4), pp. 406-415.
- [10] Gilkes, C., and Whitfield, P., 2007, "Intracranial Pressure and Cerebral Blood Flow," Surgery, **25**(12), pp. 530-535.
- [11] Stehbens, W. E., 1972, *Pathology of the Cerebral Blood Vessels*, C. V. Mosby, Saint Louis, MO.
- [12] Canham, P. B., Talman, E. A., Finlay, H. M., and Dixon, J. G., 1991, "Medial Collagen Organization in Human Arteries of the Heart and Brain by Polarized Light Microscopy," Connect. Tissue Res., **26**(1-2), pp. 121-134.

- [13] Hayashi, K., Handa, H., Nagasawa, S., Okumura, A., and Moritake, K., 1980, "Stiffness and Elastic Behavior of Human Intracranial and Extracranial Arteries," *J. Biomech.*, **13**(2), pp. 175-184.
- [14] Hayashi, K., Nagasawa, S., Naruo, Y., Okumura, A., Moritake, K., and Handa, H., 1980, "Mechanical Properties of Human Cerebral Arteries," *Biorheology*, **17**(3), pp. 211-218.
- [15] Moritake, K., Handa, H., Okumura, A., Nagasawa, S., Naruo, Y., Hayashi, K., Sato, M., and Hazama, F., 1981, "Quantitative Analysis of Microstructural Components of Human Cerebral Arteries," *Neurol. Res.*, **3**(1), pp. 67-82.
- [16] Wagenseil, J. E., and Mecham, R. P., 2009, "Vascular Extracellular Matrix and Arterial Mechanics," *Physiol. Rev.*, **89**(3), pp. 957-989.
- [17] Canham, P. B., 1977, "Orientation of Cerebral Vascular Smooth Muscle, Mathematically Modelled," *J. Biomech.*, **10**(4), pp. 241-251.
- [18] Dobrin, P. B., 1984, "Mechanical Behavior of Vascular Smooth Muscle in Cylindrical Segments of Arteries in Vitro," *Ann. Biomed. Eng.*, **12**(5), pp. 497-510.
- [19] Price, J. M., Davis, D. L., and Knauss, E. B., 1981, "Length-Dependent Sensitivity in Vascular Smooth Muscle," *Am. J. Physiol. Heart Circ. Physiol.*, **241**(4), pp. H557-563.
- [20] Ohta, T., Mori, M., Ogawa, R., and Tsuji, M., 1991, "Development of a New Perfusion System for Pharmacological Study on Rabbit Basilar Arteries," *Stroke*, **22**(3), pp. 384-389.
- [21] Hogestatt, E. D., Andersson, K. E., and Edvinsson, L., 1983, "Mechanical Properties of Rat Cerebral Arteries as Studied by a Sensitive Device for Recording of Mechanical Activity in Isolated Small Blood Vessels," *Acta Physiol. Scand.*, **117**(1), pp. 49-61.
- [22] Saito, A., Shiba, R., Yanagisawa, M., Masaki, T., Kimura, S., Yamada, K., Mima, T., Shigeno, T., and Goto, K., 1991, "Endothelins: Vasoconstrictor Effects and Localization in Canine Cerebral Arteries," *Br. J. Pharmacol.*, **103**(1), pp. 1129-1135.
- [23] Somlyo, A. P., and Somlyo, A. V., 1992, "Smooth Muscle Structure and Function," *The Cardiovascular System*, Fozzard, H. M., ed., Raven Press, New York, pp. 1295-1324.

- [24] Berk, B. C., 2001, "Vascular Smooth Muscle Growth: Autocrine Growth Mechanisms," *Physiol. Rev.*, **81**(3), pp. 999-1030.
- [25] Bobik, A., 2006, "Transforming Growth Factors and Vascular Disorders," *Arterioscler. Thromb. Vasc. Biol.*, **26**(8), pp. 1712-1720.
- [26] Monson, K. L., Goldsmith, W., Barbaro, N. M., and Manley, G. T., 2003, "Axial Mechanical Properties of Fresh Human Cerebral Blood Vessels," *ASME J. Biomech. Eng.*, **125**(2), p. 288.
- [27] Monson, K. L., Barbaro, N. M., and Manley, G. T., 2008, "Biaxial Response of Passive Human Cerebral Arteries," *Ann. Biomed. Eng.*, **36**(12), pp. 2028-2041.
- [28] Humphrey, J. D., 2002, *Cardiovascular Solid Mechanics : Cells, Tissues, and Organs*, Springer, New York, NY.
- [29] Zulliger, M. A., 2004, "A Constitutive Formulation of Arterial Mechanics Including Vascular Smooth Muscle Tone," *Am. J. Physiol. Heart Circ. Physiol.*, **287**(3), pp. H1335-H1343.
- [30] Baek, S., Gleason, R. L., Rajagopal, K. R., and Humphrey, J. D., 2007, "Theory of Small on Large: Potential Utility in Computations of Fluid-Solid Interactions in Arteries," *Comput Methods Appl Mech Eng*, **196**(31-32), pp. 3070-3078.
- [31] Eberth, J. F., Taucer, A. I., Wilson, E., and Humphrey, J. D., 2009, "Mechanics of Carotid Arteries in a Mouse Model of Marfan Syndrome," *Ann. Biomed. Eng.*, **37**(6), pp. 1093-1104.
- [32] Hu, J., Baek, S., and Humphrey, J., 2007, "Stress–Strain Behavior of the Passive Basilar Artery in Normotension and Hypertension," *J. Biomech.*, **40**(11), pp. 2559-2563.
- [33] Hu, J. J., Fossum, T. W., Miller, M. W., Xu, H., Liu, J. C., and Humphrey, J. D., 2007, "Biomechanics of the Porcine Basilar Artery in Hypertension," *Ann. Biomed. Eng.*, **35**(1), pp. 19-29.
- [34] Finlay, H. M., McCullough, L., and Canham, P. B., 1995, "Three-Dimensional Collagen Organization of Human Brain Arteries at Different Transmural Pressures," *J. Vasc. Res.*, **32**(5), pp. 301-312.
- [35] Kim, Y. S., Galis, Z. S., Rachev, A., Han, H.-C., and Vito, R. P., 2009, "Matrix Metalloproteinase-2 and -9 Are Associated with High Stresses Predicted Using a Nonlinear Heterogeneous Model of Arteries," *ASME J. Biomech. Eng.*, **131**(1), p. 011009.

- [36] Borel, C. O., McKee, A., Parra, A., Haglund, M. M., Solan, A., Prabhakar, V., Sheng, H., Warner, D. S., and Niklason, L., 2003, "Possible Role for Vascular Cell Proliferation in Cerebral Vasospasm after Subarachnoid Hemorrhage," *Stroke*, **34**(2), pp. 427-433.
- [37] Liu-Deryke, X., and Rhoney, D. H., 2006, "Cerebral Vasospasm after Aneurysmal Subarachnoid Hemorrhage: An Overview of Pharmacologic Management," *Pharmacotherapy*, **26**(2), pp. 182-203.
- [38] Dumont, A. S., Dumont, R. J., Chow, M. M., Lin, C. L., Calisaneller, T., Ley, K. F., Kassell, N. F., and Lee, K. S., 2003, "Cerebral Vasospasm after Subarachnoid Hemorrhage: Putative Role of Inflammation," *Neurosurgery*, **53**(1), pp. 123-133.
- [39] Rhoton, A. L., Jackson, F. E., Gleave, J., and Rumbaugh, C. T., 1977, "Congenital and Traumatic Intracranial Aneurysms," *Clin. Symp.*, **29**(4), pp. 1-40.
- [40] Humphrey, J. D., Baek, S., and Niklason, L. E., 2007, "Biochemomechanics of Cerebral Vasospasm and Its Resolution: I. A New Hypothesis and Theoretical Framework," *Ann. Biomed. Eng.*, **35**(9), pp. 1485-1497.
- [41] Gleason, R. L., Gray, S. P., Wilson, E., and Humphrey, J. D., 2004, "A Multiaxial Computer-Controlled Organ Culture and Biomechanical Device for Mouse Carotid Arteries," *ASME J. Biomech. Eng.*, **126**(6), p. 787.
- [42] Larson, A. M., and Yeh, A. T., 2006, "Ex Vivo Characterization of Sub-10-Fs Pulses," *Opt Lett*, **31**(11), pp. 1681-1683.
- [43] Van Loon, P., 1977, "Length-Force and Volume-Pressure Relationships of Arteries," *Biorheology*, **14**(4), pp. 181-201.
- [44] Monson, K. L., Goldsmith, W., Barbaro, N. M., and Manley, G. T., 2003, "Axial Mechanical Properties of Fresh Human Cerebral Blood Vessels," *ASME J. Biomech. Eng.*, **125**(2), pp. 288-294.
- [45] Monson, K. L., Goldsmith, W., Barbaro, N. M., and Manley, G. T., 2005, "Significance of Source and Size in the Mechanical Response of Human Cerebral Blood Vessels," *J. Biomech.*, **38**(4), pp. 737-744.
- [46] Vinall, P. E., and Simeone, F. A., 1987, "Whole Mounted Pressurized in Vitro Model for the Study of Cerebral Arterial Mechanics," *J. Vasc. Res.*, **24**(1-2), pp. 51-62.
- [47] Baek, S., Valentin, A., and Humphrey, J. D., 2007, "Biochemomechanics of Cerebral Vasospasm and Its Resolution: II. Constitutive Relations and Model Simulations," *Ann. Biomed. Eng.*, **35**(9), pp. 1498-1509.

- [48] Holzapfel, G. A., Gasser, T. C., and Ogden, R. W., 2000, "A New Constitutive Framework for Arterial Wall Mechanics and a Comparative Study of Material Models," *J Elast*, **61**(1-3), pp. 1-48.
- [49] Weizsacker, H. W., Lambert, H., and Pascale, K., 1983, "Analysis of the Passive Mechanical Properties of Rat Carotid Arteries," *J. Biomech.*, **16**(9), pp. 703-715.
- [50] Canham, P. B., Whittaker, P., Barwick, S. E., and Schwab, M. E., 1992, "Effect of Pressure on Circumferential Order of Adventitial Collagen in Human Brain Arteries," *Can. J. Physiol. Pharmacol.*, **70**(2), pp. 296-305.
- [51] Stalhand, J., Klarbring, A., and Karlsson, M., 2004, "Towards in Vivo Aorta Material Identification and Stress Estimation," *Biomech Model Mechanobiol*, **2**(3), pp. 169-186.
- [52] Gasser, T. C., Ogden, R. W., and Holzapfel, G. A., 2006, "Hyperelastic Modelling of Arterial Layers with Distributed Collagen Fibre Orientations," *J R Soc Interface*, **3**(6), pp. 15-35.
- [53] Humphrey, J. D., and Taylor, C. A., 2008, "Intracranial and Abdominal Aortic Aneurysms: Similarities, Differences, and Need for a New Class of Computational Models," *Annu. Rev. Biomed. Eng.*, **10**, pp. 221-246.
- [54] von Maltzahn, W. W., Besdo, D., and Wiemer, W., 1981, "Elastic Properties of Arteries: A Nonlinear Two-Layer Cylindrical Model," *J. Biomech.*, **14**(6), pp. 389-397.
- [55] Demiray, H., and Vito, R. P., 1991, "A Layered Cylindrical-Shell Model for an Aorta," *Int J Eng Sci*, **29**(1), pp. 47-54.
- [56] Bunce, D. F. M., 1974, *Atlas of Arterial Histology*, W. H. Green, St. Louis, MO.
- [57] Humphrey, J. D., 2008, "Vascular Adaptation and Mechanical Homeostasis at Tissue, Cellular, and Sub-Cellular Levels," *Cell Biochem. Biophys.*, **50**(2), pp. 53-78.
- [58] Wicker, B. K., Hutchens, H. P., Wu, Q., Yeh, A. T., and Humphrey, J. D., 2008, "Normal Basilar Artery Structure and Biaxial Mechanical Behaviour," *Comput. Methods Biomech. Biomed. Eng.*, **11**(5), pp. 539-551.
- [59] Eberth, J. F., Taucer, A. I., Wilson, E., and Humphrey, J. D., 2009, "Mechanics of Carotid Arteries in a Mouse Model of Marfan Syndrome," *Ann. Biomed. Eng.*, **37**(6), pp. 1093-1104.

- [60] Achakri, H., Rachev, A., Stergiopoulos, N., and Meister, J. J., 1994, "A Theoretical Investigation of Low Frequency Diameter Oscillations of Muscular Arteries," *Ann. Biomed. Eng.*, **22**(3), pp. 253-263.
- [61] Carlson, B. E., and Secomb, T. W., 2005, "A Theoretical Model for the Myogenic Response Based on the Length–Tension Characteristics of Vascular Smooth Muscle," *Microcirculation*, **12**(4), pp. 327-338.
- [62] Arribas, S. M., Hinek, A., and Gonzalez, M. C., 2006, "Elastic Fibres and Vascular Structure in Hypertension," *Pharmacol. Ther.*, **111**(3), pp. 771-791.
- [63] Greenwald, S. E., 2007, "Ageing of the Conduit Arteries," *J. Pathol.*, **211**(2), pp. 157-172.
- [64] O'Rourke, M. F., and Hashimoto, J., 2007, "Mechanical Factors in Arterial Aging: A Clinical Perspective," *J. Am. Coll. Cardiol.*, **50**(1), pp. 1-13.
- [65] Blacher, J., and Safar, M. E., 2005, "Large-Artery Stiffness, Hypertension and Cardiovascular Risk in Older Patients," *Nat Clin Pract Cardiovasc Med*, **2**(9), pp. 450-455.
- [66] Lacolley, P., Challande, P., Osborne-Pellegrin, M., and Regnault, V., 2009, "Genetics and Pathophysiology of Arterial Stiffness," *Cardiovasc. Res.*, **81**(4), pp. 637-648.
- [67] Lakatta, E. G., Wang, M., and Najjar, S. S., 2009, "Arterial Aging and Subclinical Arterial Disease Are Fundamentally Intertwined at Macroscopic and Molecular Levels," *Med. Clin. North Am.*, **93**(3), pp. 583-604.
- [68] Benetos, A., Laurent, S., Hoeks, A. P., Boutouyrie, P. H., and Safar, M. E., 1993, "Arterial Alterations with Aging and High Blood Pressure. A Noninvasive Study of Carotid and Femoral Arteries," *Arterioscler. Thromb. Vasc. Biol.*, **13**(1), pp. 90-97.
- [69] Bortolotto, L. A., Hanon, O., Franconi, G., Boutouyrie, P., Legrain, S., and Girerd, X., 1999, "The Aging Process Modifies the Distensibility of Elastic but Not Muscular Arteries," *Hypertension*, **34**(4), pp. 889-892.
- [70] Ferruzzi, J., Vorp, D. A., and Humphrey, J. D., 2011, "On Constitutive Descriptors of the Biaxial Mechanical Behaviour of Human Abdominal Aorta and Aneurysms," *J R Soc Interface*, **8**(56), pp. 435-450.
- [71] Valentin, A., Cardamone, L., Baek, S., and Humphrey, J. D., 2009, "Complementary Vasoactivity and Matrix Remodelling in Arterial Adaptations to Altered Flow and Pressure," *J R Soc Interface*, **6**(32), pp. 293-306.

- [72] Jackson, Z. S., 2002, "Wall Tissue Remodeling Regulates Longitudinal Tension in Arteries," *Circ. Res.*, **90**(8), pp. 918-925.
- [73] Langille, B. L., and Dajnowiec, D., 2007, "Arterial Adaptations to Chronic Changes in Haemodynamic Function: Coupling Vasomotor Tone to Structural Remodelling," *Clin. Sci.*, **113**(1), p. 8.
- [74] Saito, A., Shiba, R., Kimura, S., Yanagisawa, M., Goto, K., and Masaki, T., 1989, "Vasoconstrictor Response of Large Cerebral-Arteries of Cats to Endothelin, an Endothelium-Derived Vasoactive Peptide," *Eur. J. Pharmacol.*, **162**(2), pp. 353-358.
- [75] Mima, T., Yanagisawa, M., Shigeno, T., Saito, A., Goto, K., Takakura, K., and Masaki, T., 1989, "Endothelin Acts in Feline and Canine Cerebral Arteries from the Adventitial Side," *Stroke*, **20**(11), pp. 1553-1556.
- [76] Kobayashi, H., Hayashi, M., Kobayashi, S., Kabuto, M., Handa, Y., and Kawano, H., 1990, "Effect of Endothelin on the Canine Basilar Artery," *Neurosurgery*, **27**(3), pp. 357-361.
- [77] Utkan, T., Kaya, T., and Sarioglu, Y., 1997, "Effects of Sympathectomy on Endothelin-1 and Histamine Responses of Rabbit Carotid Artery," *Gen. Pharmacol.*, **29**(2), pp. 197-199.
- [78] Cox, R. H., 1977, "Effects of Age on the Mechanical Properties of Rat Carotid Artery," *Am. J. Physiol. Heart Circ. Physiol.*, **233**(2), pp. H256-263.
- [79] Dobrin, P. B., and Rovick, A. A., 1969, "Influence of Vascular Smooth Muscle on Contractile Mechanics and Elasticity of Arteries," *Am. J. Physiol.*, **217**(6), pp. 1644-1651.
- [80] Masson, I., Boutouyrie, P., Laurent, S., Humphrey, J., and Zidi, M., 2008, "Characterization of Arterial Wall Mechanical Behavior and Stresses from Human Clinical Data," *J. Biomech.*, **41**(12), pp. 2618-2627.
- [81] Cox, R. H., 1975, "Anisotropic Properties of the Canine Carotid Artery in Vitro," *J. Biomech.*, **8**(5), pp. 293-300.
- [82] Nagasawa, S., Handa, H., Okumura, A., Naruo, Y., Moritake, K., and Hayashi, K., 1979, "Mechanical Properties of Human Cerebral Arteries. Part 1: Effects of Age and Vascular Smooth Muscle Activation," *Surg. Neurol.*, **12**(4), pp. 297-304.

- [83] Toda, N., Hatano, Y., and Hayashi, S., 1978, "Modifications by Stretches of the Mechanical Response of Isolated Cerebral and Extracerebral Arteries to Vasoactive Agents," *Pflugers Arch.*, **374**(1), pp. 73-77.
- [84] Aoki, T., and Nishimura, M., 2011, "The Development and the Use of Experimental Animal Models to Study the Underlying Mechanisms of Ca Formation," *J. Biomed. Biotechnol.*, **2011**, pp. 1-10.
- [85] Hasenfuss, G., 1998, "Animal Models of Human Cardiovascular Disease, Heart Failure and Hypertrophy," *Cardiovasc. Res.*, **39**(1), pp. 60-76.
- [86] Megyesi, J. F., Vollrath, B., Cook, D. A., and Findlay, J. M., 2000, "In Vivo Animal Models of Cerebral Vasospasm: A Review," *Neurosurgery*, **46**(2), pp. 448-461.
- [87] Titova, E., Ostrowski, R. P., Zhang, J. H., and Tang, J., 2009, "Experimental Models of Subarachnoid Hemorrhage for Studies of Cerebral Vasospasm," *Neurol. Res.*, **31**(6), pp. 568-581.
- [88] Wagner, H., and Humphrey, J., (*submitted*), "Distinctive Biaxial Mechanical Behaviors of Elastic and Muscular Arteries: Common Carotid Versus Basilar Arteries."
- [89] Manning, P. J., Ringler, D. H., and Newcomer, C. E., 1994, *The Biology of the Laboratory Rabbit*, Academic Press, San Diego, CA.
- [90] Bakker, E. N., van Der Meulen, E. T., Spaan, J. A., and VanBavel, E., 2000, "Organoid Culture of Cannulated Rat Resistance Arteries: Effect of Serum Factors on Vasoactivity and Remodeling," *Am. J. Physiol. Heart Circ. Physiol.*, **278**(4), pp. H1233-1240.
- [91] Hansen-Schwartz, J., and Edvinsson, L., 2000, "Increased Sensitivity to Et-1 in Rat Cerebral Arteries Following Organ Culture," *Neuroreport*, **11**(3), pp. 649-652.
- [92] Hoel, N. L., Hansen-Schwartz, J., and Edvinsson, L., 2001, "Selective up-Regulation of 5-Ht(1b/1d) Receptors During Organ Culture of Cerebral Arteries," *Neuroreport*, **12**(8), pp. 1605-1608.
- [93] Yoshimoto, Y., Kim, P., Sasaki, T., Kirino, T., and Takakura, K., 1995, "Functional Changes in Cultured Strips of Canine Cerebral Arteries after Prolonged Exposure to Oxyhemoglobin," *J. Neurosurg.*, **83**(5), pp. 867-874.
- [94] Nilsson, T., Longmore, J., Shaw, D., Olesen, I. J., and Edvinsson, L., 1999, "Contractile 5-Ht1b Receptors in Human Cerebral Arteries: Pharmacological Characterization and Localization with Immunocytochemistry," *Br. J. Pharmacol.*, **128**(6), pp. 1133-1140.

- [95] Bardy, N., Karillon, G. J., Merval, R., Samuel, J. L., and Tedgui, A., 1995, "Differential Effects of Pressure and Flow on DNA and Protein Synthesis and on Fibronectin Expression by Arteries in a Novel Organ Culture System," *Circ. Res.*, **77**(4), pp. 684-694.
- [96] Han, H. C., and Ku, D. N., 2001, "Contractile Responses in Arteries Subjected to Hypertensive Pressure in Seven-Day Organ Culture," *Ann. Biomed. Eng.*, **29**(6), pp. 467-475.
- [97] Han, H.-C., Ku, D. N., and Vito, R. P., 2003, "Arterial Wall Adaptation under Elevated Longitudinal Stretch in Organ Culture," *Ann. Biomed. Eng.*, **31**(4), pp. 403-411.
- [98] Vorp, D. A., Peters, D. G., and Webster, M. W., 1999, "Gene Expression Is Altered in Perfused Arterial Segments Exposed to Cyclic Flexure Ex Vivo," *Ann. Biomed. Eng.*, **27**(3), pp. 366-371.
- [99] Bakker, E. N., Buus, C. L., Spaan, J. A., Perree, J., Ganga, A., Rolf, T. M., Sorop, O., Bramsen, L. H., Mulvany, M. J., and Vanbavel, E., 2005, "Small Artery Remodeling Depends on Tissue-Type Transglutaminase," *Circ. Res.*, **96**(1), pp. 119-126.
- [100] Bakker, E. N., Buus, C. L., VanBavel, E., and Mulvany, M. J., 2004, "Activation of Resistance Arteries with Endothelin-1: From Vasoconstriction to Functional Adaptation and Remodeling," *J. Vasc. Res.*, **41**(2), pp. 174-182.
- [101] Bakker, E. N., van der Meulen, E. T., van den Berg, B. M., Everts, V., Spaan, J. A., and VanBavel, E., 2002, "Inward Remodeling Follows Chronic Vasoconstriction in Isolated Resistance Arteries," *J. Vasc. Res.*, **39**(1), pp. 12-20.
- [102] Kida, T., Chuma, H., Murata, T., Yamawaki, H., Matsumoto, S., Hori, M., and Ozaki, H., 2010, "Chronic Treatment with Pdgf-Bb and Endothelin-1 Synergistically Induces Vascular Hyperplasia and Loss of Contractility in Organ-Cultured Rat Tail Artery," *Atherosclerosis*, **214**(2), pp. 288-294.
- [103] Schiotz, L., Buus, C. L., Hessellund, A., and Mulvany, M. J., 2000, "Effect of Mitogens on Growth and Contractile Responses of Rat Small Arteries: In Vitro Studies," *Acta Physiol. Scand.*, **169**(2), pp. 103-113.
- [104] Yamakawa, K., Peterson, J. W., Sibilia, R., and Zervas, N. T., 1995, "Effect of Vasoconstrictor Agents on Diacylglycerol Content of Normal and Vasospastic Canine Basilar Arteries in Vitro," *Neurosurgery*, **36**(4), pp. 789-796.

- [105] Junqueira, L. C., Bignolas, G., and Brentani, R. R., 1979, "Picrosirius Staining Plus Polarization Microscopy, a Specific Method for Collagen Detection in Tissue Sections," *Histochem. J.*, **11**(4), pp. 447-455.
- [106] Hu, J. J., Ambrus, A., Fossum, T. W., Miller, M. W., Humphrey, J. D., and Wilson, E., 2007, "Time Courses of Growth and Remodeling of Porcine Aortic Media During Hypertension: A Quantitative Immunohistochemical Examination," *J. Histochem. Cytochem.*, **56**(4), pp. 359-370.
- [107] Ostergaard, J. R., and Oxlund, H., 1987, "Collagen Type Iii Deficiency in Patients with Rupture of Intracranial Saccular Aneurysms," *J. Neurosurg.*, **67**(5), pp. 690-696.
- [108] Nagasawa, S., Handa, H., Naruo, Y., Moritake, K., and Hayashi, K., 1982, "Experimental Cerebral Vasospasm Arterial Wall Mechanics and Connective Tissue Composition," *Stroke*, **13**(5), pp. 595-600.
- [109] Masaki, T., Ninomiya, H., Sakamoto, A., and Okamoto, Y., 1999, "Structural Basis of the Function of Endothelin Receptor," *Mol. Cell. Biochem.*, **190**(1-2), pp. 153-156.
- [110] Tirapelli, C. R., Casolari, D. A., Yogi, A., Montezano, A. C., Tostes, R. C., Legros, E., D'Orléans-Juste, P., and de Oliveira, A. M., 2005, "Functional Characterization and Expression of Endothelin Receptors in Rat Carotid Artery: Involvement of Nitric Oxide, a Vasodilator Prostanoid and the Opening of K⁺ Channels in Etb-Induced Relaxation," *Br. J. Pharmacol.*, **146**(6), pp. 903-912.
- [111] Frommer, K. W., and Muller-Ladner, U., 2008, "Expression and Function of Eta and Etb Receptors in Ssc," *Rheumatology (Oxford)*, **47**(Suppl 5), pp. v27-v28.
- [112] Price, L. C., and Howard, L. S., 2008, "Endothelin Receptor Antagonists for Pulmonary Arterial Hypertension: Rationale and Place in Therapy," *Am J Cardiovasc Drugs*, **8**(3), pp. 171-185.
- [113] Huang, L.-H., He, J.-Y., Yuan, B.-X., and Cao, Y.-X., 2010, "Lipid Soluble Smoke Particles Upregulate Endothelin Receptors in Rat Basilar Artery," *Toxicol. Lett.*, **197**(3), pp. 243-255.
- [114] Chuong, C. J., and Fung, Y. C., 1983, "Three-Dimensional Stress Distribution in Arteries," *ASME J. Biomech. Eng.*, **105**(3), pp. 268-274.
- [115] Humphrey, J. D., 1999, "An Evaluation of Pseudoelastic Descriptors Used in Arterial Mechanics," *ASME J. Biomech. Eng.*, **121**(2), pp. 259-262.

- [116] Holzapfel, G. A., Gasser, T. C., and Ogden, R. W., 2004, "Comparison of a Multi-Layer Structural Model for Arterial Walls with a Fung-Type Model, and Issues of Material Stability," *ASME J. Biomech. Eng.*, **126**(2), pp. 264-275.
- [117] Holzapfel, G. A., Gasser, T. C., and Stadler, M., 2002, "A Structural Model for the Viscoelastic Behavior of Arterial Walls: Continuum Formulation and Finite Element Analysis," *Eur. J. Mech. A Solids*, **21**(3), pp. 441-463.
- [118] Zahalak, G. I., 1996, "Non-Axial Muscle Stress and Stiffness," *J. Theor. Biol.*, **182**(1), pp. 59-84.
- [119] Zahalak, G. I., and Ma, S. P., 1990, "Muscle Activation and Contraction: Constitutive Relations Based Directly on Cross-Bridge Kinetics," *ASME J. Biomech. Eng.*, **112**(1), pp. 52-62.
- [120] Stalhand, J., and Klarbring, A., 2005, "Aorta in Vivo Parameter Identification Using an Axial Force Constraint," *Biomech Model Mechanobiol*, **3**(4), pp. 191-199.

VITA

Name: Hallie Paige Wagner

Address: 337 Zachry Engineering Center
3120 TAMU
College Station, TX 77843-3120

Email Address: hallie_h@tamu.edu

Education: B.S., Biomedical Engineering, Washington University in St. Louis,
2005
Ph.D., Biomedical Engineering, Texas A&M University, 2011